DECIPHERING THE DOLOMITIZATION HISTORY OF THE LOWER MEMBER WINNIPEGOSIS CARBONATES: BASIN-SCALE GRADIENTS IN MAGNESIUM AND STRONTIUM ISOTOPES IDENTIFY THE DEEP STRUCTURAL CENTER OF THE WILLISTON BASIN AS A SOURCE OF REACTIVE MAGNESIUM

A Thesis Submitted to the
College of Graduate and Postdoctoral Studies
In Partial Fulfillment of the Requirements
For the Degree of Master of Science
In the Department of Geological Sciences
University of Saskatchewan
Saskatoon

By

MATTHEW D. NADEAU

PERMISSION TO USE

In presenting this thesis/dissertation in partial fulfillment of the requirements for a Postgraduate degree from the University of Saskatchewan, I agree that the Libraries of this University may make it freely available for inspection. I further agree that permission for copying of this thesis in any manner, in whole or in part, for scholarly purposes may be granted by the professor or professors who supervised my thesis work (Dr. C. Holmden) or, in their absence, by the Head of the Department or the Dean of the College of Graduate and Postdoctoral Studies. It is understood that any copying or publication or use of this thesis/dissertation or parts thereof for financial gain shall not be allowed without my written permission. It is also understood that due recognition shall be given to me and to the University of Saskatchewan in any scholarly use which may be made of any material in my thesis titles *"Deciphering the Dolomitization History of the Lower Member Winnipegosis Carbonates: Basin-Scale Gradients in Magnesium and Strontium Isotopes Identify the Deep Structural Center of the Williston Basin as a Source of Reactive Magnesium"*

DISCLAIMER

Reference in this thesis to any specific commercial products, process, or service by trade name, trademark, manufacturer, or otherwise, does not constitute or imply its endorsement, recommendation, or favoring by the University of Saskatchewan. The views and opinions of the author expressed herein do not state or reflect those of the University of Saskatchewan and shall not be used for advertising or product endorsement purposes. Requests for permission to copy or to make other uses of materials in this thesis/dissertation in whole or part should be addressed to:

Department of Geological Sciences
University of Saskatchewan
114 Science Place
Saskatoon, Saskatchewan, S7H 5E2, Canada

--OR—

Dean
College of Graduate and Postdoctoral Studies
University of Saskatchewan
116 Thorvaldson Building, 110 Science Place
Saskatoon, Saskatchewan, S7N 5C9
Canada

UNIVERSITY OF SASKATCHEWAN

College of Graduate and Postdoctoral Studies

Deciphering the Dolomitization History of the Lower Member Winnipegosis Carbonates: Basin-Scale Gradients in Magnesium and Strontium Isotopes Identify the Deep Structural Center of the Williston Basin as a Source of Reactive Magnesium

Submitted in partial fulfillment
of the requirements of the
Degree of Master of Science

By

Matthew D. Nadeau
Department of Geological Sciences
University of Saskatchewan
September 2019

Examining Committee:

Dr. J. Merriam	Chair of Graduate Committee
Dr. C. Holmden	Supervisor, Department of Geological Sciences
Dr. W. Patterson	Department of Geological Sciences
Dr. B. Eglington	Department of Geological Sciences
Dr. A. Immenhauser	External Examiner

ABSTRACT

Dolomitized carbonates in the Williston Basin are common below the Middle Devonian Prairie Evaporite Formation, highlighting the conceivable role of brine reflux as the source of magnesium (Mg) for dolomitization. However, strontium isotope ratios ($^{87}Sr/^{86}Sr$), and iron (Fe) and manganese (Mn) concentrations in a dolomite body directly below the evaporite (in the Lower Member Winnipegosis Formation near Saskatoon, SK) are inconsistent with its formation using seawater as the source of reactive Mg. It has been proposed instead that the dolomitizing fluids ascended from deep in the basin where sedimentary formation waters may develop very radiogenic $^{87}Sr/^{86}Sr$ ratios through water-rock interaction with Rb-bearing siliciclastic sediments and old crystalline rocks of the Precambrian basement (Fu et al., 2006). In this thesis, I expand the geographic range of the studied dolomite samples covering most of the northern half of the Williston Basin, and I employed novel stable Mg isotopes ($\delta^{26}Mg$) as a tracer of the dolomitizing fluids. The main finding is that the Lower Member Winnipegosis records a basin scale gradient in dolomite $\delta^{26}Mg$ values, with low values (~ –2.0‰) in the deep center of the basin in North Dakota, and higher values (~ –1.3‰) near the outcrop edge of the basin in Manitoba. The $\delta^{26}Mg$ and $^{87}Sr/^{86}Sr$ data, when plotted on a geographic map of the Williston Basin and contoured using Surfer® software, reveal a radial pattern of increasing $\delta^{26}Mg$ values and decreasing $^{87}Sr/^{86}Sr$ ratios. Using water-rock interaction modeling, I show that the gradients in $\delta^{26}Mg$ and $^{87}Sr/^{86}Sr$ formed when hot Mg-bearing and ^{87}Sr-bearing fluids flowed upwards through the Winnipegosis from a source in the center of the basin. The gradient in ^{87}Sr occurs from dilution of the higher $^{87}Sr/^{86}Sr$ ratio of the dolomitizing fluid by the release of seawater-derived Sr to pore fluids with a lower $^{87}Sr/^{86}Sr$ ratio along the flow path. The gradient in $\delta^{26}Mg$ reflects Mg isotope exchange between: (1) an early formed replacive proto-dolomite with a uniform $\delta^{26}Mg$ value (~ –1.55‰) reflecting its formation at ambient temperature in an open diagenetic system using seawater as a source of reactive Mg ($\delta^{26}Mg \approx 0.15$‰), and (2) a hot (~90ºC) upwardly ascending Mg-bearing fluid with a lower $\delta^{26}Mg$ value (~ –0.80‰). The gradient arises from greater exchange occurring between proto-dolomite and fluid at higher cumulative water-rock ratios in the deep basin (closer to the source of reactive Mg) and less exchange occurring near the edges at lower cumulative water-rock ratios. The resulting ~1.0‰ gradient in dolomite $\delta^{26}Mg$ signifies cryptic mixing between primary and secondary dolomite formed at two different temperatures from Mg bearing fluids with

different δ^{26}Mg values at two different stages in the basin history. The burial history of the basin is punctuated by heat flow anomalies, with fluid movement indicated by the resetting of thermal remnant magnetizations in dolomite and evaporite minerals within the basin. I speculate that ultramafic rocks supplied Mg to the bottom of the Williston Basin when they were hydrothermally altered or carbonated during an anomalous heat flow event that affected the Williston Basin in the Late Devonian/Early Carboniferous. Seismic pumping drove these fluids upwards through fracture networks in the crust, and eventually into the deep center of the Williston Basin along vertically-oriented down-to-the-basement faults, pressuring deep confined aquifers like the Winnipegosis that induced up dip migrations of fluid towards the edges of the basin. This study demonstrates that Mg isotopic mapping of large dolomite bodies is a useful tool for deciphering paleofluid-flow histories in sedimentary basins, which may help exploration geologists to find petroleum that may have migrated and become trapped along the same pathways, or Mississippi Valley Type ore deposits. Lastly, contouring mapping of Fe, Mn and δ^{13}C values in the Lower Member Winnipegosis dolomite shows that these are not tracers of dolomitizing fluid flow or signals of the dolomitization process in the studied dolomites. They see through the dolomitization and record information on carbonate depositional environments.

ACKNOWLEDGMENTS

First and foremost, I would like to express my gratitude to my supervisor, Dr. C. Holmden, for providing me the opportunity to study under his direction and providing me support, guidance, and patience throughout my studies. I would also like to thank the members of my advisory committee for their support and contributions: Dr. B. Eglington and Dr. B. Patterson. I am grateful to my fellow students: Brayden McDonald, Christopher K. West, Brittany Laing, Jyostnamani Mohanta, Isabelle Baconnais, and Iliajah Pidskalney for the many stimulating discussions. I would like to extend many thanks to M. Nasreen and S. Timsic, for their assistance and mentorship in the Lab, and to J. Rosen for his technical expertise. I would like to thank the staff at the Saskatchewan Ministry of the Economy's Subsurface Geological Laboratory, the Manitoba Geological Survey's Resource Development Division Drillcore Library and the North Dakota Geological Survey Wilson M. Laird Core & Sample Library for granting me sampling privileges and the use of their facilities. The University of Saskatchewan Devolved and Graduate Teaching Fellowship funded this thesis, as well as NSERC Discovery Grants and Saskatchewan Ministry of the Economy Grants.

TABLE OF CONTENTS

LIST OF FIGURES

LIST OF FIGURES

presence of a reaction front, highlighted by the green box, that moves through the rock in the direction of fluid flow. By panel D, the reaction front has migrated past the modeled flow path length shown. Behind the reaction front, Type 1 proto-dolomite is progressively transformed to Type 2 dolomite, producing a gradient of increasing δ^{26}Mg values in the direction of fluid flow, reflecting the fact that proto-dolomite located closer to the source of the dolomitizing fluid in the deep center of the Williston basin is exposed to higher cumulative water-rock volumes during ascending flow than proto-dolomite located near the edges of the basin (A-D). This gradient will eventually be removed if the fluid flow event continues long enough to equilibrate the entire dolomite body with the new higher temperature Mg-bearing fluid. Gray dotted line represents the echo of the previous bulk rock δ^{26}Mg value.

Conceptual model of ascending Mg-bearing fluid flow originating from the center of the Williston Basin and below, with up dip directed fluid flow through permeable carbonate aquifers. Three confined carbonate-bearing aquifers would have channelized the bulk of the fluid flow: (1) the Middle Devonian Winnipegosis aquifer of this study, (2) the Silurian Interlake aquifer, and (3) the Late Ordovician Red River aquifer (Kimmig, 2017). Only the Interlake dolomites remain to be studied using Mg isotopes. Note that the thickness of the Prairie Evaporite Formation decreases towards the basin margins. Vertical black lines illustrate the down-to-the-basement faults abundantly located near the structural center of the Williston Basin (Anna, 2013). Black arrows denote hypothetical subsurface fluid migration trajectories. TDS = Total Dissolved Solids. The blue color estimates the portion of the deep Williston Basin with TDS concentrations in formation waters of the order of ten times the salinity of seawater (Bachu and Hitchon, 1996; Grasby et al., 2000).

Shaded contour map of carbonate δ^{18}O values of the Lower Member Winnipegosis Formation. The erosional extent of the Middle Devonian Elk Point Basin demarcates the countering limits. Thick black line represents the divide between the central basin / mud mound facies and the surrounding platform facies (Modified after Fischer and Burke, 1987 and Jin and Bergman, 1999). See locations of sampled sites indicated by red circles. Depth to the top of the Winnipegosis is represented as an isopach overlay shown in solid and dashed lines (300 m spacing, max depth dashed contour line at 2900 m below sea level).

Photomicrographs showing textures of type 1 dolomite (A–E) and type 2 (F–J) dolomite. **(A)** Dolomite in the upper view field of picture (fc) is finely crystalline and nonplanar-a, which is interpreted as resulting from recrystallization. Intercrystalline porosities are filled with acicular anhydrite. Dolomite in the lower view field of picture (mc) is microcrystalline. 6-36-38-28W2, 1041 m, the Upper Winnipegosis Member (UW), plane polarized light (PPL). **(B)** Crystals of type 1 dolomite in precursor grains (ac) are coarser than those in matrix (mt). 16-20-37-8W3, 1104Æ6m, UW, PPL. **(C)** Crystals of type 1 dolomite in precursor grains (ac) are finer than those in matrix (mt). A single, inclusion-enriched dolomite crystal mimics the morphology of a crinoidal fragment (cf). 13-1-38-8W3, 1152Æ8m, UW, PPL. **(D)** Very fine to finely crystalline, planar-s type 1 dolomite. Note crystal size varies from very finely crystalline (fc) in one side of the stylolite to finely crystalline (cc) in the other side. 10-29-36-9W3, 1179Æ4 m, UW, PPL. **(E)** Type 1 dolomite mimetically replaces the radiaxial fibrous cements inferred to have precipitated as calcite from sea water in submarine environments. 6-36-38-28W2, 1047Æ0 m, UW, cross polarized light. **(F)** Type 2 dolomite is medium crystalline and mainly planar-e. Note intercrystalline porosity. 7-2-38-1W3, 1186Æ0 m, the Lower Winnipegosis Member (LW), PPL. **(G)** Dolomitization (do) front in limestone (ls) is constrained by a stylolite (st). 6-16-38-1W3, 1175Æ9 m, LW, PPL. **(H)** Replacement of limestone by type 2 dolomite occurs along dissolution seams (ds). 6-16-38-1W3, 1175Æ9 m, LW, PPL. (I) Wackestone (red stained with Alizarin Red-S) is partially replaced by type 2 dolomite (in grey color). In the left half view field of picture, rhomboid type 2 dolomite crystals ‘floating’ in limestone; in the right half view field of picture, limestone relicts (mainly grain relicts, denoted by gr) ‘floating’ in dolomite. 13-3-42-26W2, 1002Æ1 m, LW, PPL. **(J)** Type 2 dolomite showing medium crystalline, planar-s fabric. Note dolomite crystals are truncated by stylolites (sl). 16-11-33-1W3, 1278Æ2 m, LW, PPL. Modified after Fu et al., 2006.

LIST OF TABLES

LIST OF ABBREVIATIONS

AFT – Apatite Fission Track
AGL – Aqueous Geochemical Lab
B.S.L. – Below Sea Level
CAM-1 – Cambridge 1 Magnesium
DIC – Dissolved Inorganic Carbon
DSM3 – Dead Sea Magnesium 3
HMC – High Magnesium Calcite
IC – Ion Chromatography
ICP-MS – Inductively Coupled Plasma Mass Spectrometry
LW – Lower Winnipegosis Member
MC-ICP-MS – Multi-Collector Inductively Coupled Plasma Mass Spectrometry
NBS – National Bureau of Standards
SIL – Saskatchewan Isotope Lab
SIL-1 – Saskatchewan Isotope Lab Magnesium
SIMS – Secondary Ionization Mass Spectrometry
TDS – Total Dissolved Solids
TIMS – Thermal Ionization Mass Spectrometry
UW – Upper Winnipegosis Member
VHMC – Vary High Magnesium Calcite
VPDB – Vienna PEE DEE Belemnite
WA – Whitkow Anhydrites

CHAPTER 1 – Introduction

Carbonates are prominent minerals in the hydrosphere, biosphere, and geosphere, and are integral to the global cycles of magnesium (Mg), calcium (Ca), and carbon (C). Sedimentary successions of marine carbonates are essential archives for geochemical proxy reconstructions of Earth's changing climate, ocean chemistry, and tectonics over geological time (e.g., Clark and Fontes, 1990; Degens and Epstein, 1964; Hayes and Waldbauer, 2006; Knoll et al., 1986; Sharma and Clayton, 1965; Stuiver, 1970). However, in order to develop accurate records of Earths past environments, it is necessary to recognize that the original geochemistry and mineralogy of marine carbonates are susceptible to alteration during diagenesis (Bathurst, 1972; Swart and Eberli, 2005). Without accurate reconstruction, diagenetic effects may lead to false inferences about seawater chemistry. One of the most apparent diagenetic processes, and the subject of this study, is dolomitization. While dolomite ($CaMg(CO_3)_2$) (de Dolomieu, 1791) is thermodynamically favored to directly precipitate abiotically from modern-day seawater (Warren, 2000), it is kinetically inhibited (Hardie, 1987, Land 1998) by aqueous magnesium's stable double hydration shell and the strong complex that it forms with dissolved sulfate ions (Lippman, 1973; Morrow and Rocketts, 1988). Accordingly, dolomite is not abundantly present in modern-day marine carbonate environments (Warren, 2000), sharply contrasting its prevalence as a common constituent of marine carbonate successions in the deep geological past. This observation is the basis of the "dolomite problem".

$$2CaCO_{3\,(s)} + Mg^{2+}_{(aq)} = CaMg(CO_3)_{2\,(s)} + Ca^{2+}_{(aq)} \qquad K_{eq} = \frac{a_{Ca^{2+}}}{a_{Mg^{2+}}} = 1.49 \tag{1.1}$$

Consequently, most dolomite in the rock record is believed to have formed by replacement of metastable calcite and aragonite ($CaCO_3$) in subsurface diagenetic environments where fluid-flow through the pore spaces of the sediment is required to deliver reactive Mg to the sites of dolomitization, and to remove the product Ca, according to Equation 1.1 (Land, 1980; Machel, 2004). Massive replacive dolomite is therefore a hydrogeological phenomenon (Land, 1998; Machel, 2004). Dolomite may form early in the diagenetic history of a carbonate deposit using seawater as the dolomitizing fluid, and geothermal heating (Kahout) or brine reflux as drivers of fluid flow. It may also form after deep burial has occurred from Mg-bearing formation waters migrating in response to sediment compaction, tectonic loading, topographically driven meteoric water recharge, or buoyancy effects related to the emplacement of magmatic intrusions (Land, 1985; Machel, 2004; Morrow, 1982; Warren, 2000).

Whether it is proto-dolomite forming by replacement of primary carbonate, or dolomite forming by replacement of proto-dolomite, there is a tendency for the composition of dolomite to evolve along the fluid flow path. If this evolution is interrupted before proto-dolomite or dolomite fully equilibrates with the migrating fluid, or the migrating fluid composition or temperature changes, a compositional gradient will be recorded by the dolomite in the direction of fluid flow. (Ahm et al., 2018; Banner and Hanson, 1990; Husson et al., 2015). For example, $\delta^{18}O$ values in carbonates can be altered at very low water-rock ratios (~$10e^0$ - $10e^1$) without affecting $\delta^{13}C$ values, which require higher water-rock ratios (~$10e^3$ - $10e^4$) to become altered, owing to drastic differences in concentrations of O and C between carbonate minerals (high O, high C) and diagenetic fluids (high O, low C) (Figure 1.1) (Ahm et al., 2018; Banner and Hanson, 1990; Husson et al., 2015). It is for this reason that dolomites often preserve $\delta^{13}C$ values belonging to the original carbonate deposits. Differences in water-rock ratios required to alter different elements and their isotopes can be computed from mass balance considerations (Figure 1.1). In this thesis, I apply principles of water-rock interaction modeling to understand the origin and significance of basin scale-gradients in dolomite $\delta^{26}Mg$ values and $^{87}Sr/^{86}Sr$ ratios in the Lower Member Winnipegosis Formation (Middle Devonian) in the Williston Basin.

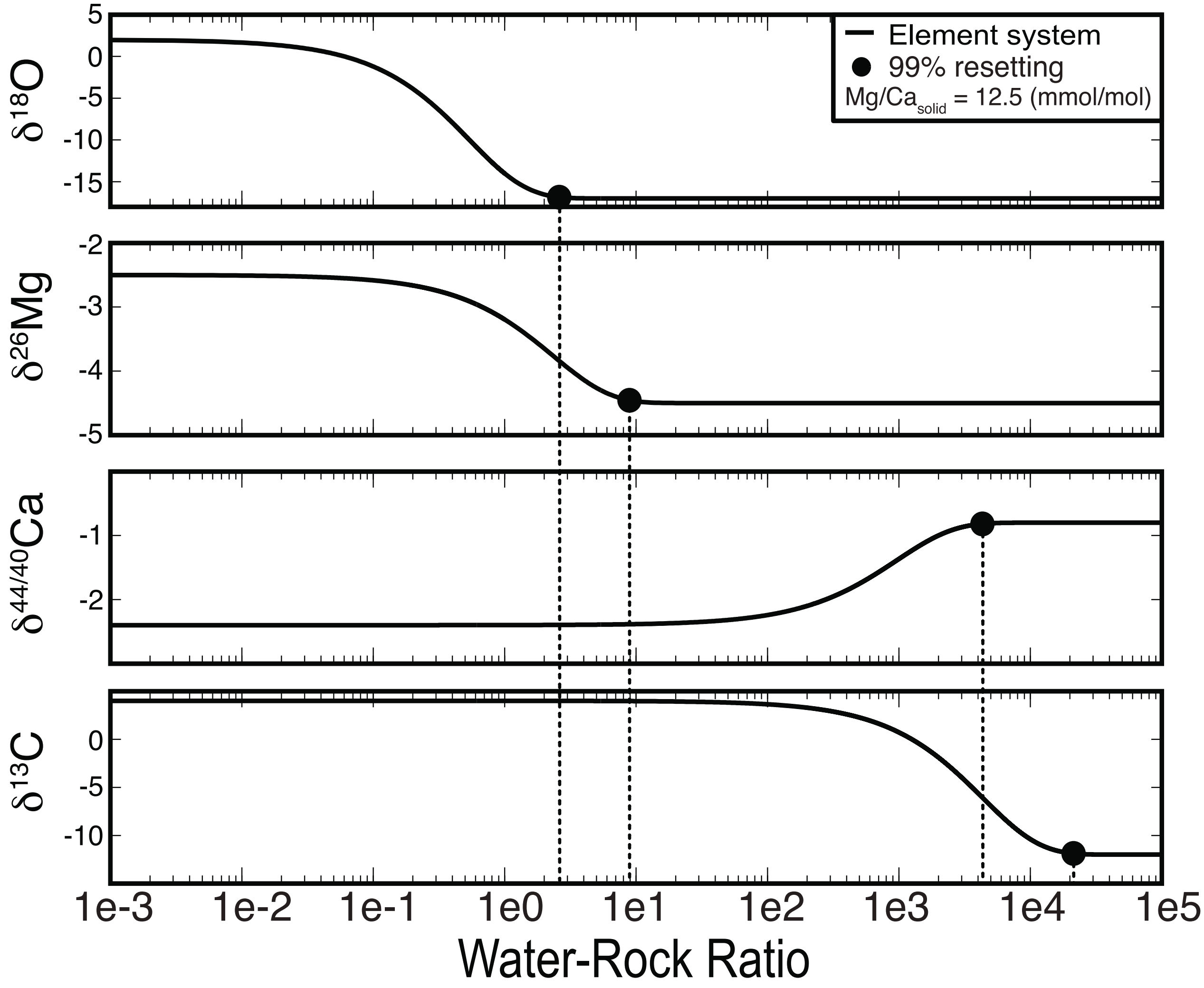

Figure 1.1 Example simulations of $CaCO_3$ diagenesis, after Ahm et al. (2018), Banner and Hanson (1990) and Husson et al. (2015), where limestone reacts with modern-day seawater: Ca (10.3 mmol/kg), Mg (52.8 mmol/kg) and C (2.3 mmol/kg). Precursor limestone has a Mg/Ca ratio of 12.5 mmol/mol. Isotopic resetting progresses left to right, as water-rock ratios increase. 'Fully reset' is defined by black circles which represent 99% resetting. The relative ease of resetting is $\delta^{18}O > \delta^{26}Mg > \delta^{44/40}Ca > \delta^{13}C$. However, if proto-dolomite ($(Ca,Mg,CO_3)_2$) is the carbonate phase being altered, then $\delta^{26}Mg$ values will equilibrate at higher water-rock ratios due to the higher concentration of Mg, similar to the water-rock ratios required to alter $\delta^{44/40}Ca$ values in $CaCO_3$.

1.1 The magnesium isotope proxy – an interpretive framework for tracing paleofluid flow

Magnesium has three naturally occurring isotopes, ^{24}Mg, ^{25}Mg and ^{26}Mg with relative abundances of 78.99%, 10.00%, and 11.01%, respectively (Catanzaro et al., 1966; Rosman and Taylor, 1998). It is the 8th most abundant element in the continental crust (Taylor and McLennan, 1985) and 4th most abundant element in seawater (Millero, 1974) due to its high solubility and mobility in the aqueous environment. Mg isotope studies in the 1970s aimed to resolve small isotopic anomalies of ^{26}Mg in meteorites produced by radioactive decay of primordial ^{26}Al (e.g., Lee and Papanastassiou, 1974; Wasserburg et al., 1977). These measurements were performed by Thermal Ionization Mass Spectrometry (TIMS) or Secondary Ion Mass Spectrometry (SIMS), which works well for determining abundances of isotopic anomalies, but not for measurements of mass-dependent stable isotope fractionations. Owing to the lack of four or more naturally occurring isotopes of Mg, a double-spiking technique cannot be used to correct for mass fractionation effects that occur during sample preparation and analysis. As such, most early isotopic measurements aimed at determining mass-dependent fractionation of Mg isotopes in nature were hampered by significant analytical uncertainties (±1 to 2‰), leading to the general misconception of limited fractionation of stable Mg isotopes on Earth.

It was not until the development of Multiple Collector Inductively Coupled Plasma Mass Spectrometry (MC-ICP-MS) in the middle to late 1990s that accurate Mg isotope measurements were made possible using a standard-bracketing technique (Galy et al., 2001, 2003). Since then, stable isotope measurements of Mg isotope abundances in terrestrial materials has become routine (e.g., Galy et al., 2001; Galy et al., 2003; Dessert et al., 2005; Tipper et al., 2006; Tipper et al., 2008; Hippler et al., 2009; Higgins and Schrag, 2010; Fantle and Higgins, 2014; Geske et al., 2015a; Geske et al., 2015b; Blättler et al., 2015; Higgins and Schrag, 2015; Husson et al., 2015; Mavromatis et al., 2017; Gothmann et al., 2017; Kimmig, 2017; Kimmig and Holmden, 2017; Kimmig et al, 2018; Higgins et al., 2018). Due to the relative mass difference between ^{24}Mg and ^{25}Mg (4%) and ^{24}Mg and ^{26}Mg (8%), the range of ^{26}Mg/^{24}Mg is about twice as large as the range of ^{25}Mg/^{24}Mg (e.g., Galy et al., 2001) due to mass dependent fractionation processes. These measured ratios are converted to delta notation (δ) and reported as permil (‰) deviations from the DSM3 standard, as δ^{26}Mg and δ^{25}Mg values, respectively (Equation 3.1). Review papers by Hoefs

(2015) and Teng (2017) show a 6‰ range of δ^{26}Mg values in terrestrial materials. Carbonate minerals record a large range of the known fractionation of Mg isotopes in nature (~5‰) (Figure 1.2).

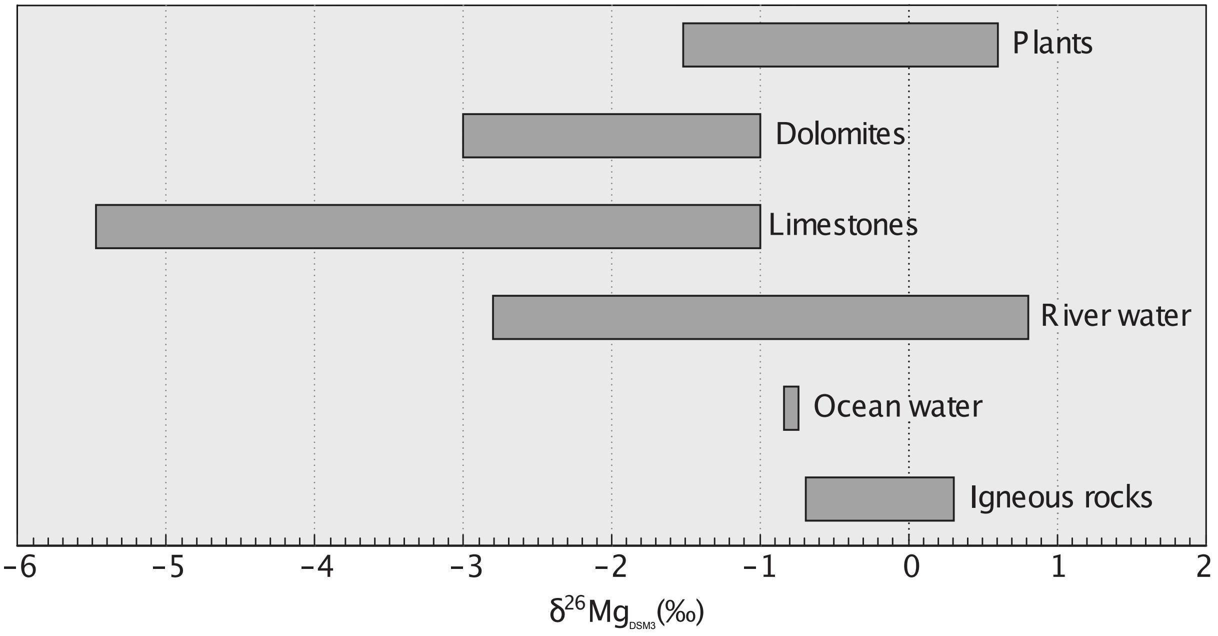

Figure 1.2 δ^{26}Mg values of important geological reservoirs. Figure reproduced from Hoefs (2015) and Teng (2017) and references therein.

Mg isotopes are ideally suited to studies of dolomite. Firstly, dolomite contains abundant Mg for analysis. Secondly, the bulk of the Mg isotope fractionation on earth occurs in surface and near-surface environments where dolomite typically forms (Figure 1.2). Thirdly, Mg isotopes are fractionated during dolomite precipitation, favoring the uptake of light Mg isotopes in dolomite. As a result, migrating fluid δ^{26}Mg values evolve in the direction of fluid flow by Rayleigh fractionation, becoming progressively enriched in ^{26}Mg as a result of preferential uptake of ^{24}Mg into precipitated dolomite (Figure 1.3) (Higgins and Schrag, 2010; Fantle and Higgins, 2014; Blättler et al., 2015; Li et al., 2015; Peng et al., 2016; Ahm et al., 2018; Bialik et al., 2018; Higgins et al., 2018; Kimmig, 2017; Li et al., 2019). Consequently, dolomite bodies are hypothesized to record spatial gradients in their δ^{26}Mg values that can be used to pinpoint the source of Mg and the direction of fluid flow during dolomitization. This has been attempted before using the stable isotopes of O (δ^{18}O values) and C (δ^{13}C values), and the radiogenic isotopes of Sr (^{87}Sr/^{86}Sr ratios) as proxies for Mg-bearing fluid flow, but the interpretations are often ambiguous (e.g., Wilson, 1990; Qing and Mountjoy, 1992). In this study, I use Mg isotopes for the same purpose, which is a direct tracer of the dolomitizing fluids.

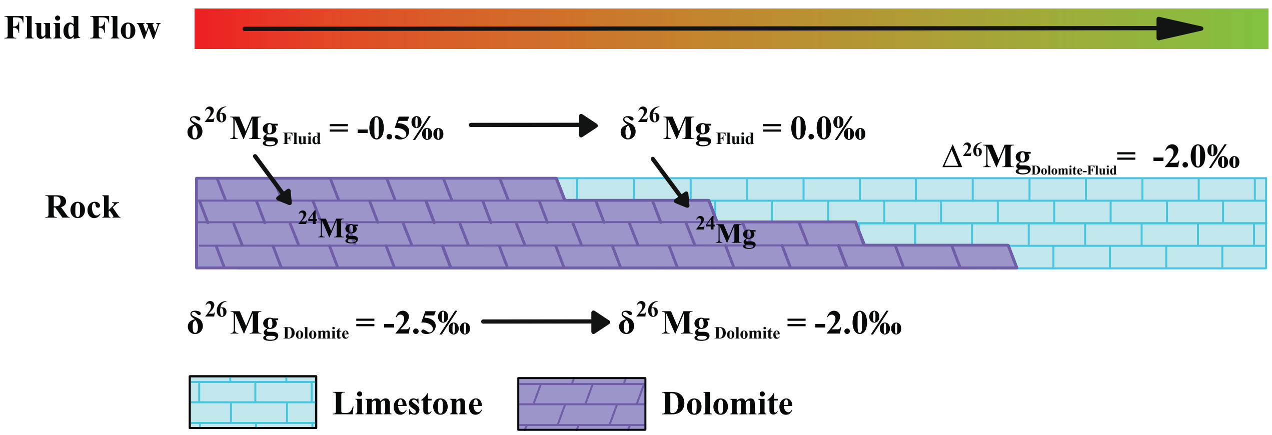

Figure 1.3 A conceptual model showing progressive enrichments of ^{26}Mg in fluids and dolomite formed along the flow path during replacive dolomitization. The fractionation factor (Δ^{26}Mg) ($\equiv 1000\ln(\alpha)$) between dolomite and aqueous Mg ions is temperature dependent. The –2.0‰ fractionation factor used in this example is appropriate for dolomitization in near-surface diagenetic environments at ambient temperatures (e.g., Higgins and Schrag, 2010; Fantle and Higgins, 2014 Blättler et al., 2015; Li et al., 2015). Smaller fractionation factors would accompany dolomitization at higher temperatures in deep-burial diagenetic systems.

Many factors likely influence the scale and magnitude of the hypothesized gradients in dolomite δ^{26}Mg values: including, the crystal-chemical mechanism of dolomite formation, the rate of dolomitization relative to the rate of fluid flow and supply of Mg ions, how open or closed the diagenetic system is during dolomite formation, the extent to which the rocks themselves are sources of isotopically contrasting Mg (e.g., high Mg-calcite (HMC)), and the degree to which earlier formed proto-dolomite is overprinted by younger dolomitization events.

$$\Delta^{26}\mathrm{Mg}_{\text{Dolomite-Fluid}} = (-0.1554 \pm 0.0096) \times {}^{10^6}\!/_{\mathrm{T}^2} \tag{1.2}$$

In addition, there are other mechanisms besides Rayleigh distillation effects, such as temperature changes and mixing, that can produce gradients in δ^{26}Mg values in dolomite bodies. As noted above, the dolomite Mg isotope fractionation factor (Δ^{26}Mg) is temperature-dependent (Equation 1.2), decreasing with increasing temperature (Li et al., 2015). The magnitude of the fractionation factor at ~12.5ºC was initially deduced from pore fluid studies of deep-sea sediment where dolomite is forming in the present day, yielding a $\Delta^{26}\mathrm{Mg} \approx -2.0‰$ ($\equiv 1000\ln(\alpha)$) (Blättler et al., 2015; Fantle and Higgins, 2014; Higgins and Schrag, 2010). The fractionation factor has also been experimentally determined over a range of hydrothermal temperatures, resulting in the isotope paleotemperature equation shown in Equation 1.2, where T is temperature in Kelvin (Li et al., 2015). Substituting 12.5ºC into Equation 1.2 yields a fractionation factor of –1.90‰, which is in good agreement with the results from pore fluid studies. If the temperature of the dolomitizing fluid were to increase along the flow path, as would happen with sinking fluids in sedimentary basins, then dolomite δ^{26}Mg values would be expected to increase in the direction of fluid flow if the fluid composition remained constant (indicative of high cumulative water-rock ratios). Mixing of two or more generations of dolomite with contrasting isotopic compositions and spatially controlled differences in abundances can also create gradients in bulk dolomite δ^{26}Mg values. Mixing effects may be cryptic in cases where an earlier formed proto-dolomite partially exchanges Mg with a younger migrating fluid.

1.2 Tracing paleofluid flow using $^{87}Sr/^{86}Sr$

Strontium has four stable isotopes ^{84}Sr, ^{86}Sr, ^{87}Sr and ^{88}Sr with approximate relative abundances of 0.56%, 9.86%, 7.00%, and 82.58% respectively. Although there is a small amount of isotopic fractionation of stable Sr isotopes in nature, it is the radiogenic production of ^{87}Sr that is used as a tracer in this study. Production of ^{87}Sr by the radioactive decay of ^{87}Rb ($T_{1/2}$ =46.8 Ga) produces large variations in ^{87}Sr/^{86}Sr in nature (Faure and Powell, 1972). Seawater, however, has a uniform ^{87}Sr/^{86}Sr ratio at any one time in the geological past due to the long oceanic residence time of Sr (~2.5 Ma), which effectively mixes the heterogenous inputs of ^{87}Sr from: (1) continental weathering (^{87}Sr/^{86}Sr = 0.711), (2) hydrothermal venting at mid-ocean ridges (^{87}Sr/^{86}Sr = 0.7035), and (3) the release of Sr from marine-sediment pore waters (^{87}Sr/^{86}Sr = 0.7067 - 0.7091) (Elderfield et al., 1986; Goldstein and Jacobsen, 1987; Palmer and Edmond, 1989). However, because the input Sr fluxes to the oceans have change over geological time, and in some cases their ^{87}Sr/^{86}Sr ratios as well, seawater ^{87}Sr/^{86}Sr varies on million-year timescales (Veizer et al., 1999).

The geochemical behavior of Sr^{2+} is similar to that of Ca^{2+} due to their similar ionic radii (1.21Å and 1.08Å respectively), electronegativity and valence. However, with the exception of aragonite, most carbonate minerals discriminate against the uptake of Sr into their crystal lattice structures. Thus, the Sr/Ca ratio of diagenetically stable carbonate minerals such as calcite and dolomite are lower than the solutions from which they precipitated. This behavior is quantified using the distribution coefficient (D_{Sr}) (=Sr/Ca_{Carb})/(Sr/Ca_{Fluid}), which is ~0.10 for calcite and ~0.011 for dolomite (Katz et al., 1972; Lorens et al., 1981; Vahrenkamp and Swart, 1990). The difference in the distribution coefficients implies that when dolomite forms by replacement of calcite (or aragonite) according to Equation 1.1, Sr will accumulate in pore fluids. Therefore, the Sr/Ca ratio of the dolomitizing fluid and the dolomite precipitated from this fluid will both increase in the direction of fluid flow. There are no stable isotope fractionation effects to consider when using ^{87}Sr/^{86}Sr as a tracer, as these are removed by the correction for mass-dependent fractionation that occurs in the mass spectrometer, which is monitored and corrected using measurements of ^{86}Sr/^{88}Sr with a true ratio of 0.1194. Accordingly, ^{87}Sr/^{86}Sr only changes by mixing of Sr sources with contrasting ^{87}Sr/^{86}Sr ratios.

If dolomitization occurs during early diagenesis using seawater as the source of reactive Mg, then the ^{87}Sr/^{86}Sr ratio of dolomite will record the ^{87}Sr/^{86}Sr ratio of seawater at that time. On the other hand, if the dolomitizing fluid was not seawater, or the seawater $^{87}Sr/^{86}Sr$ ratio was altered by water-rock interactions with siliciclastic Rb-containing rocks during fluid migration in the subsurface, then dolomite will record elevated $^{87}Sr/^{86}Sr$ ratios. Gradients in dolomite $^{87}Sr/^{86}Sr$ ratios may form by mixing along the fluid flow path where the limestone has a different $^{87}Sr/^{86}Sr$ ratio than that of the dolomitizing fluid. As Sr of seawater origin is released into pore fluids during dolomitization, the $^{87}Sr/^{86}Sr$ ratio of dolomite becomes progressively seawater-like in the direction of fluid flow.

1.3 Thesis overview

Chapter 2 explains the geological background of the thesis and research hypothesis, covering the geological setting and dolomitization models proposed for the study setting. Chapter 3 discusses the chemical and analytical procedures used, and Chapter 4 presents the results. Chapter 5 presents a model for dolomitization of the studied carbonates and discusses the broader implications of those results. Finally, Chapter 6 concludes the thesis and presents a discussion of considerations for future work.

CHAPTER 2 – Geological Background and Research Hypotheses

The Williston Basin formed along the southeastern margin of the Western Canada Sedimentary Basin. It is the textbook example of a subsiding intracratonic sedimentary basin, containing marine carbonate and siliciclastic sediment. The Williston Basin extends across Saskatchewan, Manitoba, North Dakota, and Montana, while the structural center of the basin is located in northeastern North Dakota (Figure 2.1a). Six major stratigraphic sequences belong to the Williston Basin, reflecting marine sedimentation during periods of high relative sea level, separated by periods of erosion or non-deposition manifested as unconformities. The three lower sequences of the Williston Basin are the Sauk Sequence (Cambrian-Lower Ordovician), Tippecanoe Sequence (Middle Ordovician-Lower Devonian) and Kaskaskia Sequence (Devonian-Lower Carboniferous) which are relevant to this thesis and are described below (Figure 2.2).

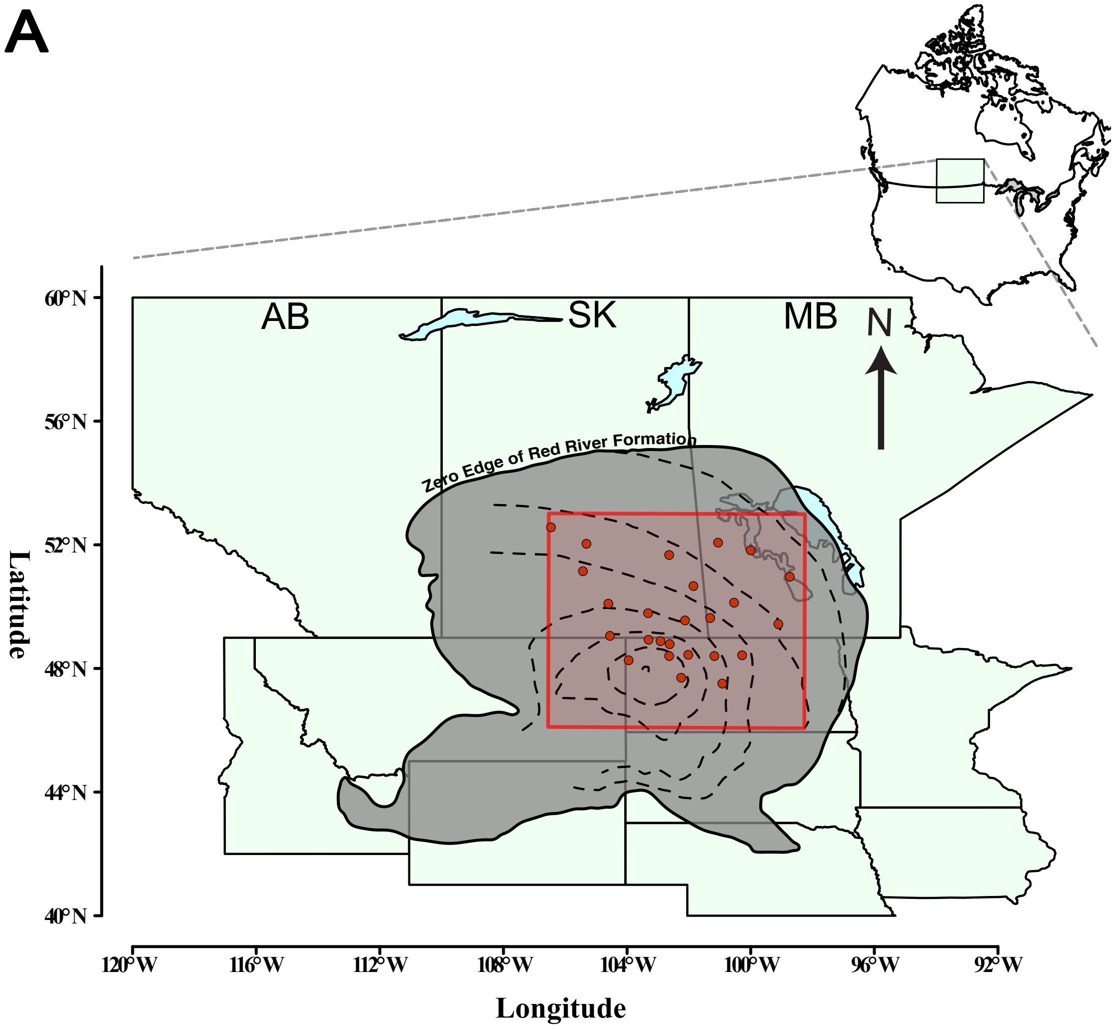

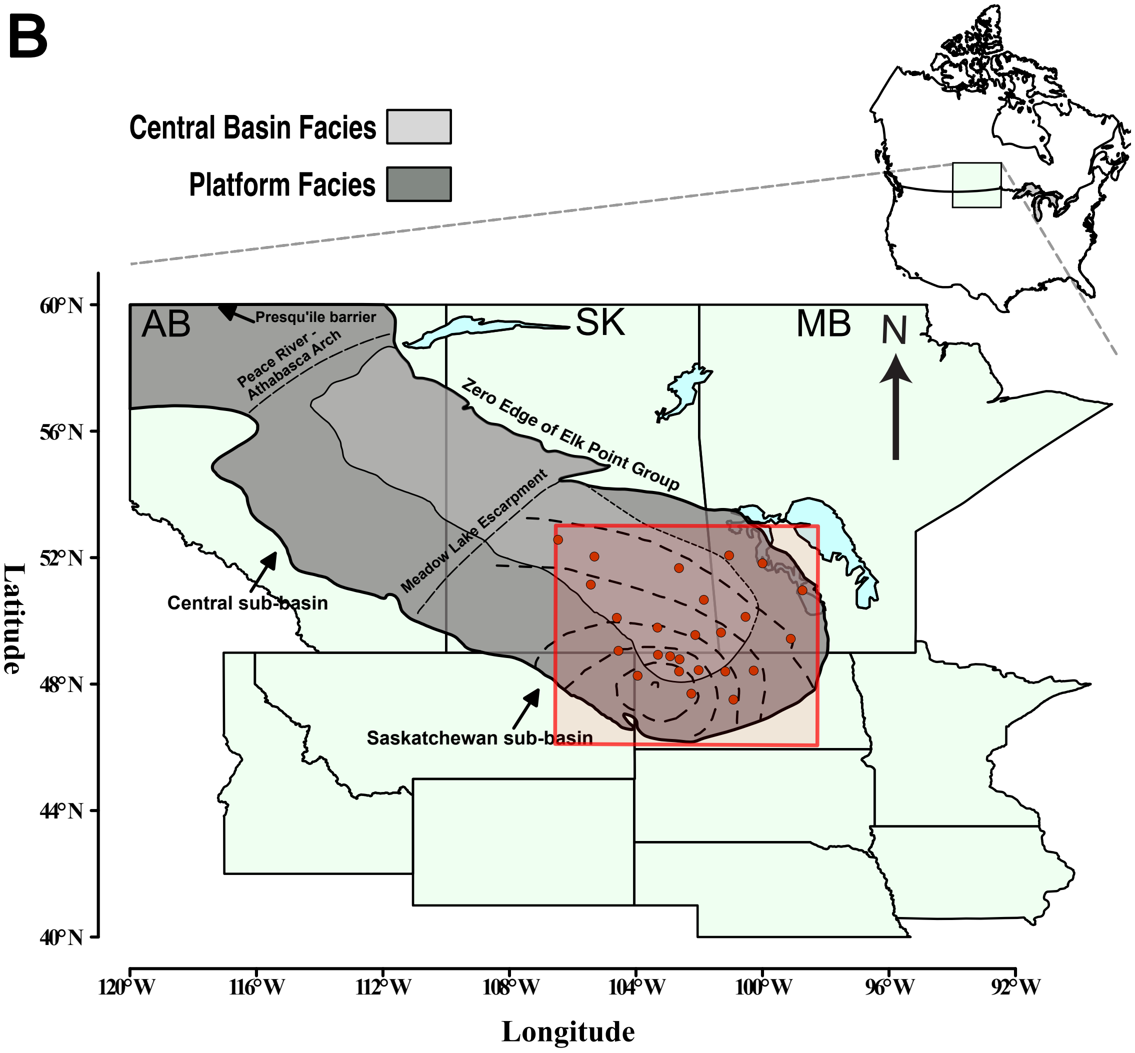

Figure 2.1 (A) Map of central North America showing the erosional extent of the Williston Basin (after Pratt and Haidl, 2008) and **(B)** the Elk Point Basin (after Fischer and Burke, 1987 and Jin and Bergman, 1999). Study area is highlighted by the red square, with studied core locations denoted by red circles. Black dashed lines represent depth isopach contours of the Winnipegosis Formation, showing the structural center of the Williston Basin (600 m spacing, max depth contour at 3200 m b.s.l.). MB, Manitoba; SK, Saskatchewan; ND, North Dakota.

The Sauk Sequence consists of the Upper Cambrian Deadwood Formation (Figure 2.2) and represents the initial stages of marine transgression over the Archean crystalline basement rocks after the Great Unconformity (Karlestrom and Timmones, 2012). The sediment source for the siliciclastic sediments of the Deadwood Formation eroded from highlands to the southeast along the Transcontinental Arch (Carlson and Thompson, 1987). Post-Sauk erosion erased much of the regressive part of this sequence and marks the first significant unconformity (Carlson and Thompson, 1987; Rédly, 1998).

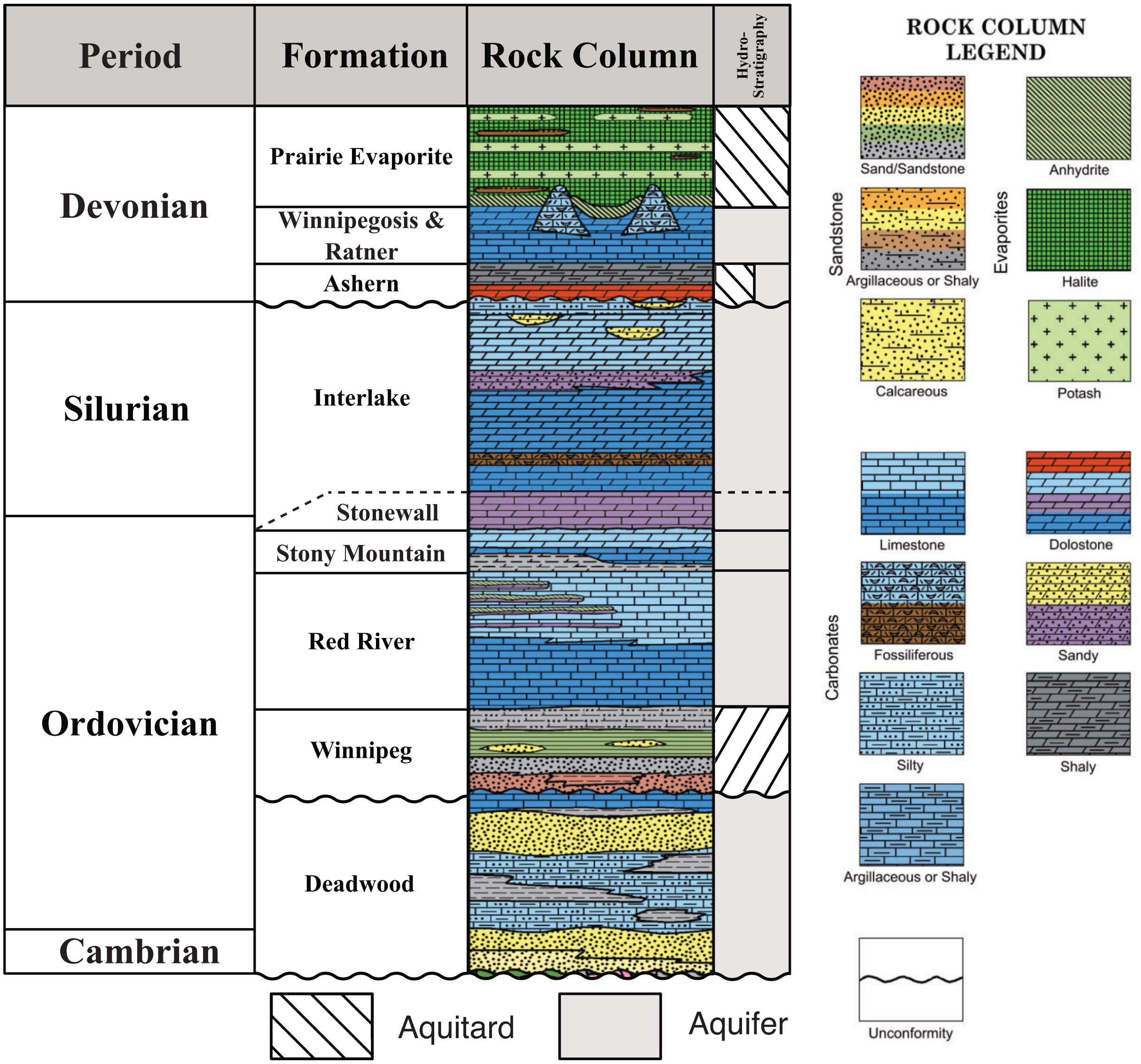

Figure 2.2 Generalized stratigraphic chart of the Cambrian to Devonian aged strata of the Williston Basin as seen in the study area. Nomenclature after Anna, (2013). Rock column after Murphy et al. (2009).

The Tippecanoe Sequence signifies the start of the second transgressive-regressive cycle during the Middle Ordovician through Silurian / earliest Devonian. Depositional patterns of the Winnipeg Formation shale and the overlying Red River Formation carbonates and evaporites (Figure 2.2) indicate that basin subsidence was occurring at this time (Gerhard and Anderson, 1988; Gerhard et al., 1990). The Red River contains three brining upward sequences, consisting of partially dolomitized burrowed limestone, overlain by laminated dolomite, and capped by anhydrite. Conformably overlying the Red River are carbonates and anhydrites of the Stony Mountain Formation, Stonewall Formation, and Interlake Formation (Figure 2.2) (Rédly, 1998). A major regression terminated Tippecanoe sedimentation near the end of the Silurian, and subsequent erosion removed parts of the Interlake, especially around the basin margins (Anna, 2013).

The Kaskaskia, beginning in the Middle Devonian (Eifelian), is discernible by a marine transgression which ultimately expanded the epicontinental sea northwards, resulting in the inundation of southern Northwest Territories, including parts of Alberta, Saskatchewan, Manitoba, North Dakota, and Montana (Figure 2.1b). The transition from Tippecanoe to Kaskaskia is marked by an unconformity between the Silurian Interlake and the Devonian Ashern formations (Figure 2.2). Carbonates belonging to the Elk Point Group were deposited in the Elk Point Basin, consisting of three sub-basins: The North and Central sub-basins divided by the Peace River–Athabasca Arch, and the Saskatchewan sub-basin divided by the Meadow Lake Escarpment (Figure 2.1b). The Saskatchewan sub-basin was a depositional basin whose subsidence was later controlled by the Williston Basin (Figure 2.1a). The four formations of the Elk Point group are from older to younger: Ashern, Winnipegosis, Ratner, and Prairie Evaporite (Figure 2.3a). The focus of this study is the Winnipegosis (Lower and Upper members), which directly underlie thin anhydrite-abundant carbonates of the Ratner, and much thicker deposits of anhydrite, halite and potash salts of the Prairie Evaporite. The Elk Point group was deposited during a transgressive-regressive cycle of relative sea-level change (Figure 2.3b).

Lower Member Winnipegosis carbonates are composed of moderately fossiliferous wackestones representing net sediment accumulation of 7-16 m. They were deposited during a transgression that followed deposition of the argillaceous Ashern carbonate and shale (Reinson and Wardlaw, 1972; Perrin, 1982). The Upper Member Winnipegosis consists of carbonate buildups once termed 'pinnacle reefs' or 'banks' that contain more mud than skeletal fragments and are, thus, now considered mud mounds by most authors (e.g., Gendzwill and Wilson, 1987; Reinson and Wardlaw, 1972; Fu et al., 2006). The mud mounds formed in ~100 m depth waters in the centre of the Saskatchewan sub-basin (central basin/mud mound facies) (Kendall, 1975). Shallow water carbonates accumulated in shallower waters surrounding the central basin (platform facies) (Jin and Bergman 1999; Martindale et al., 1991). Using seismic imaging techniques, Gendzwill (1978) found that the steep-sided Winnipegosis mounds ranged between 0.5 and 6.0 km in width, and Kendall (1975) reported thicknesses of 30–90 m. In the deep waters between the mud mounds, laminated organic-rich carbonates of the Brightholme and Ratner were deposited with interbeds of mound-derived detritus (Figure 2.3a). The Brightholme is considered a source rock for Winnipegosis oil and gas (Stoakes et al., 1987; Osadetz et al. 1990).

A sill developed along the Presqu'ile Barrier Reef complex (Figure 2.1b) that restricted the exchange of seawater between the ocean and the Saskatchewan Sub-basin along the Elk Point Seaway (Maiklem, 1971). Seawater began to evaporite in the Saskatchewan sub-basin. Lower water levels terminated growth of the mud mounds, as revealed by subaerial exposure features and vadose diagenetic cements at the top of the mud mounds (Fu et al., 2004). The Ratner laminate (1-20 m) (Fu et al., 2002; Fu et al., 2011) represents the initial stages of evaporite deposition, consisting of a brining upward succession of interbedded carbonate and anhydrite (Jin and Bergman, 1999). Continued basin desiccation resulted in the deposition of halite and potash salts of the Prairie Evaporate Formation (~150 m), which eventually buried the Upper Winnipegosis mounds (Perrin, 1982) (Figure 2.3a). At this time, the Elk Point Basin was located 0°–15° south of the equator (Heckel and Witzke, 1979; Van der Voo, 1988; Witzke, 1990).

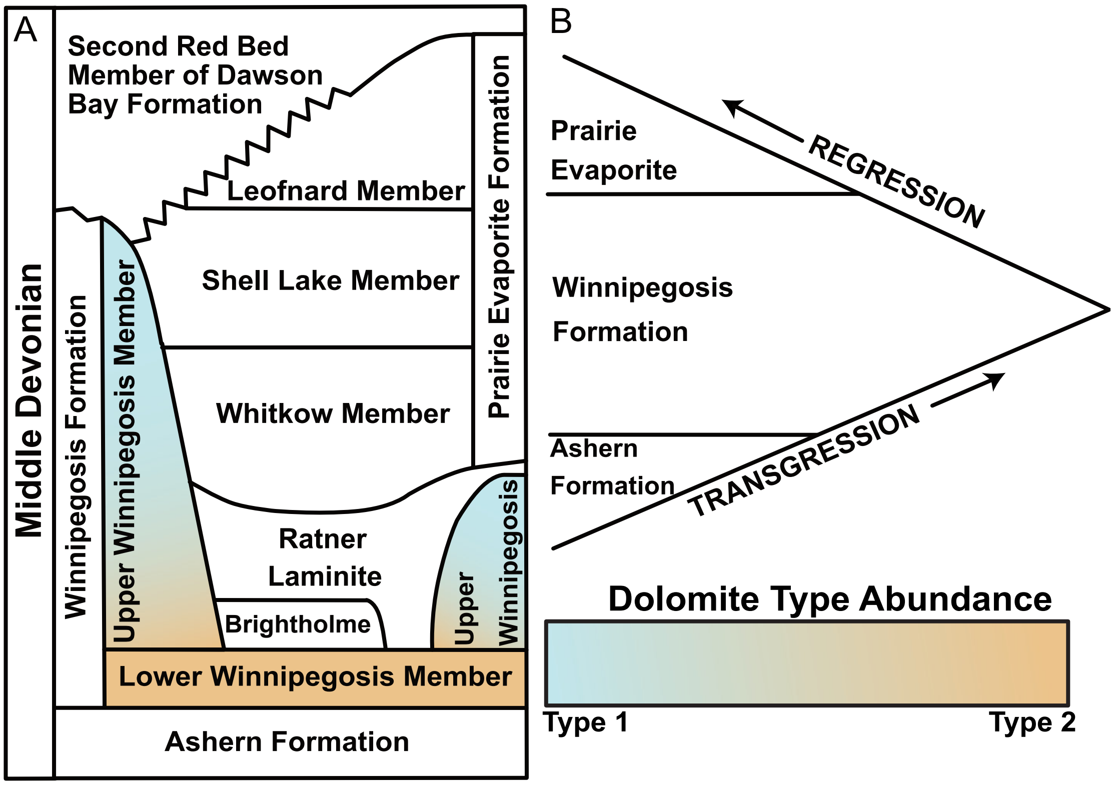

Figure 2.3 (A) Detailed stratigraphic chart and nomenclature of the Winnipegosis carbonates, Ratner laminate, and Prairie Evaporate Deposits (modified from Fu et al., 2006; Jin et al., 2001). Dolomite type abundance based on interpretations from Fu et al., 2006. **(B)** Sense of relative sea level change during deposition of Elk Point Basin sediments.

2.1 Dolomitization models for the Winnipegosis Formation

Previous studies of the Winnipegosis have detailed its stratigraphy, depositional environments (Baillie, 1951, 1953; Jin and Bergman, 1999), diagenesis (Fu et al., 2006; Jin & Bergman, 1999, 2001; Jones, 1965), and source rock maturation (Osadetz and Snowdon, 1995). The most important digenetic process is dolomitization (Fu et al., 2006). Dolomite in the Winnipegosis carbonates is ubiquitous and has been interpreted as being: (1) an artesian flow of seawater through the Lower Member Winnipegosis and upwards through the mud mounds (Kendall 1989), (2) the early diagenetic product of evaporatively concentrated seawater fluxing downward into the carbonate sediment through the mud mounds (Rosenthal 1987; Stanford 1989; Fu et al., 2006), and (3) the late diagenetic product of ascending fluid flow during deep burial (Fu et al., 2006).

Kendall (1989) suggested that Winnipegosis dolomites formed in a regional subsurface flow system driven by differences in sea level across the Presqu'ile Barrier (Figure 2.4a). The hydraulic head difference (cf., Tóth, 1963, 1980) of ~100 m pressurized the Lower Member Winnipegosis aquifer, creating an artesian system hypothesized to have carried seawater down the length of the Elk Point Basin, which then dolomitized the Lower Member carbonates. Some of the seawater discharged upwards through the mud mounds, and these were dolomitized as well (Kendall, 1989) (Figure 2.4a). If this interpretation is correct, ^{87}Sr/^{86}Sr ratios in the Winnipegosis dolomite (not measured by Kendall, 1989) should record Middle Devonian seawater signatures of ~0.7079, yet they do not, according to the subsequent study of Fu et al. (2006).

Given the large evaporite basin directly overlying the Winnipegosis carbonates in the Middle Devonian, seawater or evaporatively concentrated seawater is an attractive source of dolomitizing fluids (Ehrets & Kissling, 1987; Fu et al., 2006; Perrin, 1982; Kendall 1989; Rosenthal 1987; Stanford 1989). Fu et al. (2006) found two types of dolomite in the Winnipegosis that they called "Type 1" and "Type 2" in studied cores near Saskatoon (Figure 1a in Fu et al., 2006). Photomicrographs of "Type 1" and "Type 2" dolomites from Fu et al. (2006) are given in Appendix A – Supplementary Figure 2. Type 1 dolomite, which characterizes the Upper Member Winnipegosis mud mounds, is cryptocrystalline (<5 μm) to finely crystalline (20-60 μm) in grain size, and records a uniform ^{87}Sr/^{86}Sr ratio consistent with middle Devonian seawater (0.7079) (Fu et al., 2006) (Table 4.1). Type 2 dolomite is medium crystalline (> 60 μm) and characterizes the Lower Member Winnipegosis (Fu et al., 2006), but it is also found decreasing upwards in abundance in some of the mud mounds (Fu et al., 2006) (Figure 2.3). Type 2 dolomite records higher ^{87}Sr/^{86}Sr ratios than Type 1 dolomite, ranging between 0.70809 and 0.70928 (average 0.70853, n=14; Fu et al., 2006), implying that Type 2 dolomite did not form from Middle Devonian seawater. Taken at face value, this finding is inconsistent with the artesian flow model of dolomitization of the Winnipegosis suggested by Kendall (1989). Instead, Fu et al. (2006)

proposed that evaporatively concentrated seawater from the Saskatchewan sub-basin filtered downwards through the mud mounds and dolomitized them, consistent with the decrease in abundance of Type 1 dolomite with depth in the mounds, and in agreement with their Middle Devonian seawater $^{87}Sr/^{86}Sr$ ratios. By contrast, they proposed that Type 2 dolomite formed at a much younger age by Mg bearing fluids ascending from deeper in the Williston Basin, consistent with the more radiogenic $^{87}Sr/^{86}Sr$ ratios. It is possible that the Type 2 dolomite formed by replacement of Type 1 dolomite, but the authors did not favor this hypothesis. According to Fu et al. (2006), the decreasing abundance of Type 1 dolomite with depth in the mud mounds reflects the lower limit of descending dolomitizing fluid flow that formed Type 1 dolomite, rather than the upper limit ascending Type 2 fluids that altered Type 1 dolomite. If Type 2 dolomite formed from Type 1 dolomite, then the Kendall (1989) model for the formation of Type 1 dolomite cannot be ruled out as proposed by Fu et al. (2006). In fact, the two models for the formation of Type 1 dolomite are not mutually exclusive.

In addition to higher $^{87}Sr/^{86}Sr$ ratios, Type 2 dolomite also exhibits elevated concentrations of Fe and Mn compared to Type 1 dolomite. Accordingly, Fu et al. (2006) considered Type 2 dolomite to have formed from deep burial fluids that lacked dissolved oxygen, as Fe and Mn are both more soluble in their lower oxidation states. Type 2 dolomite also formed syn-genetically with the formation of stylolites (Fu et al., 2006), which are rock deformation features believed to require 500 to 900 m of burial before they will form in carbonate rocks (Dunnington, 1967; Fabricius, 2000; Mountjoy et al., 1999). This is consistent with Type 2 dolomite having formed in post Devonian time (Figure 2.5a) from Mg-bearing formation waters that ascended from deeper depths in the Williston Basin, where they acquired radiogenic ^{87}Sr through water-rock interactions with siliciclastic lithologies that are more abundant near the base of the sedimentary succession (Figure 2.2), or crystalline basement rocks underlying the Williston Basin. It is also possible that some of the ^{87}Sr in Type 2 dolomite was locally sourced from thin argillaceous units in the underlying Ashern (Lobdell, 1984) (Figure 2.2).

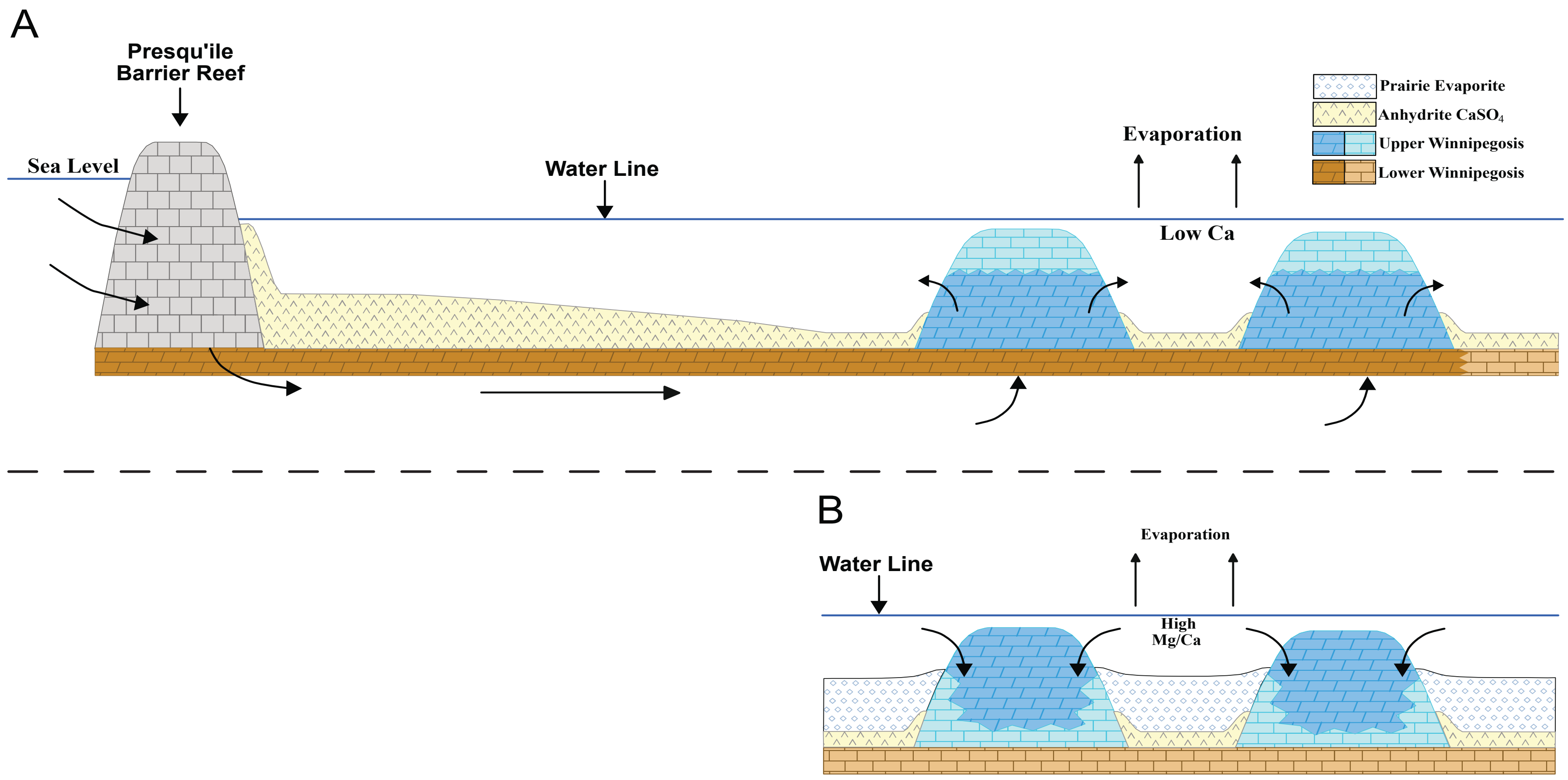

Figure 2.4 (A) Simplified cross-section of the Elk Point Basin during the Middle Devonian (early Givetian), illustrating seawater dolomitization of the Winnipegosis mud mound by Kendall (1989). Note that fluid flow through the mud mounds is upwardly directed. **(B)** Simplified cross-section of the Elk Point Basin during the Middle Devonian (early Givetian), illustrating brine reflux dolomitization where the proposed fluid flow is downward though the mud mounds (Fu et al., 2006). Dark blue (for Upper Winnipegosis) and dark brown (for Lower Winnipegosis) colors indicate dolomitized carbonates. See the legend for details.

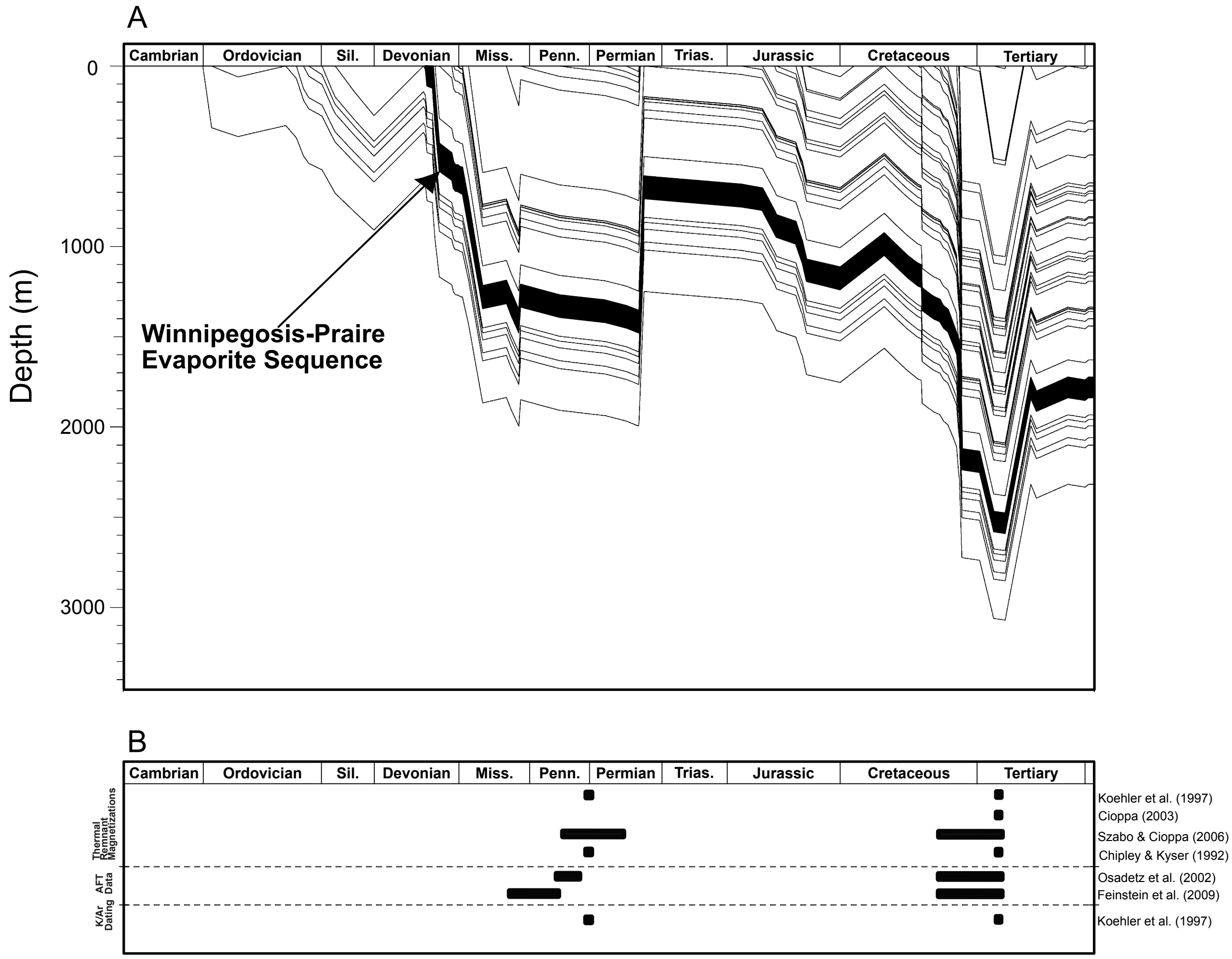

Figure 2.5 (A) Burial history of the Williston Basin based on the Baildon well (02-011-15-26W2). Modified from Osadetz et al. (2002). **(B)** Geological timescale depicting the timing of the anomalous thermal events in the Williston Basin. Black bars show timing of anomalous heating recorded by thermal remnant magnetizations, apatite fission tracks (AFT), and K/Ar dating of evaporite minerals. Modified from Kimmig (2017).

The cores with Type 1 and Type 2 dolomites studied by Fu et al. (2006) are located in the northern part of the Williston Basin near Saskatoon, SK (Figure 1a in Fu et al., 2006), where the Winnipegosis occurs approximately one kilometer below the surface. The same unit near the center of the Williston Basin in North Dakota is found over three and a half kilometers deep (Figure 2.1). If the Mg-bearing formation waters responsible for Type 2 dolomite ascended from greater depths in the Williston Basin, then the most likely path of ascent was along the gently dipping slope of the Winnipegosis aquifer, which is confined by the overlying Prairie Evaporite aquiclude and the underlying Ashern aquitard (Figure. 2.2).

2.2 A novel model of late-stage burial dolomitization – evidence from the Late Ordovician Red River Formation

The Late Ordovician Red River Formation is ~1 km deeper in the Williston Basin than the Middle Devonian Winnipegosis (Figure 2.2). Early interpretations for dolomitization of the Red River are from Kendall, described in papers written in 1976, 1977, and 1984 where he proposed a brine reflux model of dolomitization, supported by the occurrence of dolomite bodies sandwiched between three evaporitic units of bedded anhydrite. In the studied 'C' Member carbonate of the Red River, dolomite is mostly restricted to an anastomosing network of *Thalassinoides* burrows (though there are some areas where both the burrows and matrix are dolomitized). Kendall proposed that Mg bearing brines filtered downward from the overlying Herald evaporite basin and selectively dolomitized the burrows due to the higher permeability of the infilling burrow sediment compared to the matrix sediment. Kimmig (2017) found basin-scale gradients in δ^{26}Mg values and ^{87}Sr/^{86}Sr ratios in the burrow-dolomite that she interpreted as evidence for ascending flows of radiogenic ^{87}Sr and Mg-bearing fluids through the burrows, suggesting that the burrows were dolomitized very late in the diagenetic history of the deposits by burial fluids ascending from the deep center of the Williston Basin, reminiscent of the ascending fluids proposed by Fu et al. (2006) for the formation of Type 2 dolomite in the Lower Member Winnipegosis. Both authors linked ascending fluid flow to the Late Devonian/Early Carboniferous heat flow anomaly (Figure 2.5b). Kimmig (2017) found the lowest δ^{26}Mg and highest ^{87}Sr/^{86}Sr in burrow-dolomite in the deep center of the Williston Basin (Figure 2.1a). Closer to the edges of the basin, burrow-dolomite records higher δ^{26}Mg and lower ^{87}Sr/^{86}Sr (Figure 3.4a and 3.4b in Kimmig, 2017). Kimmig (2017) proposed that during the heat flow anomaly, seismic pumping drove hot Mg-bearing fluids into the bottom of the Williston Basin from the underlying crystalline basement. This induced pressurization of deep confined aquifers like the Red River, driving Mg and ^{87}Sr bearing fluids upwards through the network of burrows to the edges of the basin. Because the fluids contained Mg, the burrows were dolomitized. Alternatively, the burrows were dolomitized earlier by brine reflux as suggested by Kendall (1976, 1977, and 1984), and/or through microbial mediation as suggested by Gingras et al. (2004), and then later altered by ascending Mg-bearing fluid flow.

2.2 Research aim, hypotheses, and predictions

The objective of this research is to determine the source(s) and paleofluid flow directions for the Mg-bearing fluid that dolomitized the Lower Member Winnipegosis. Specifically, I will look for basin-scale gradients in dolomite δ^{26}Mg values and ^{87}Sr/^{86}Sr ratios between the deeply buried center of the Williston Basin in North Dakota and the outcrop edge in Manitoba, analogous to the gradients reported by Kimmig (2017) in the burrow-dolomite of the ‘C’ Member carbonate of the Red River. If gradients of similar orientation and magnitude are found, it will strengthen the case for an ascending fluid flow event in the Williston Basin that dolomitized carbonate sediment below the Prairie Evaporite aquiclude, and/or altered pre-existing proto-dolomite. If the same gradients are not found in the Winnipegosis dolomite, then the ascending fluid flow event is restricted to deeper formations. This study will, thus, provide new data for gauging the magnitude of the ascending fluid flow event that affected the Williston Basin in the late Paleozoic, with broader implications regarding the role of the crust as a source of fluid and Mg for dolomitization. This study will also bring new data to bear on the artesian flow model for dolomitization of the Winnipegosis proposed by Kendall (1989). If this interpretation is correct, I expect to find a northwest-to-southeast gradient of dolomite δ^{26}Mg values that will follow the depositional outline of the Elk Point Basin. If this interpretation is incorrect, I expect to find a gradient that conforms to the structural outline of the subsiding Williston Basin (Figure 2.1b), similar to the gradient found in burrow dolomite in the Red River (Kimmig, 2017).

CHAPTER 3 – Sampling and Analytical Methods

Carbonate samples from the Lower Member Winnipegosis were sampled *in situ* using a power drill equipped with a tungsten carbide bone crusher drill bit (Kimmig, 2017) from cores housed in storage facilities in Saskatchewan, Manitoba and North Dakota. Up to four closely spaced samples were taken from a single core box (~1 m) in the Lower Winnipegosis. Approximately 150 mg of homogenized powdered sample was dissolved in a 50 ml centrifuge tube using two-times the stoichiometric amount of ultrapure 1.0 N HCl. Samples were centrifuged when the effervescence ceased, the supernatant decanted into an acid leached Savillex^{TM} container and then dried. Any residue remaining after the dissolution was tested with a drop of 6 N HCl to ensure that the acid attack fully digested all carbonate phases. The supernatant was re-solubilized into a stock solution using 0.3 N HCl. The residue was dried, weighed, and subtracted from the original sample weights to calculate the wt.% carbonate in each sample. Aliquots of stock solutions were measured by ICP-MS for elemental concentrations (Mg, Ca, Sr, Fe, and Mn) in the Department of Geological Sciences Aqueous Geochemistry Laboratory (AGL) at the University of Saskatchewan with uncertainties typically better then ±10% (2σ).

3.1 Automated ion chromatography

In most cases, the variation in δ^{26}Mg values in terrestrial materials amounts to just 1–2‰. Therefore, highly precise measurements are required, as well chemical separations that purify Mg without fractionating its isotopes. Gravity-flow columns filled with various cation exchange resins have been traditionally used to separate and purify Mg from matrix elements in weak acid solutions (e.g., Chang et al., 2003; Kimmig, 2017). For other elements (e.g., calcium) a double-spike is added to the sample before column separations to ensure that fractionation occurring during the mass spectrometry is corrected (e.g., Russell and Papanastassiou, 1978). As four or more naturally occurring isotopes are needed to use the double-spike technique, and Mg has only three isotopes, fractionation of Mg isotopes is a major concern for the analysis of Mg isotopes. Yields of Mg from the cation exchange columns must be close to 100% to avoid isotopically fractionating the sample. This is done by checking collection yields before and after the Mg elution peak to ensure that 95% or more of the Mg was collected from the column (e.g., Chang et al., 2003; Kimmig, 2017). This results in lengthy analytical procedures and additional mass spectrometry. Advances in high-pressure ion chromatography offer an automated alternative that can increase sample throughput and decrease the number of measurements by ensuring 100% yields for Mg isotopes. Schmitt et al. (2009) showed that Ca could be separated using an automated Ion Chromatography (IC) system, and I have adopted this technique for Mg isotopes measured in this study using a Thermo Scientific Dionex ICS-5000 instrument equipped with an IonPac CS16 5×50 mm guard column and IonPac CS16 5×250 mm analytical column with methanesulfonic acid as the eluant (cf. Blättler et al., 2015). The shape of the Mg peak and timing of its release from the column can be monitored in real-time using the instrument's conductivity detector, which triggers the collection of eluted Mg using an automated fraction collector (Figure 3.1). This ensures that ~100% of the Mg is collected from the column for each purified sample, which is crucial for accurate Mg isotope analysis due to isotopic fractionation that occurs on the cation exchange columns, where the heavy isotopes of Mg travel through the column faster than the light isotopes (Chang et al., 2003; Teng et al., 2007). The overall sample elution takes approximately 32 minutes. After each elution, the IC system is cleaned for 32 min using ultrapure water (18.2 mΩ-cm). Magnesium blanks were measured by injection of ultrapure water after 30 and 60 minutes of cleaning. Blanks were measured using a Thermo-Fisher Scientific NEPTUNE multi-collector inductively-coupled plasma mass spectrometer (MC-ICP-MS), by comparing peak-voltages of the Mg isotopes in the blank to a Mg standard of known concentration. Results show that Mg blanks ranged from 8–13 ng, yielding an acceptable sample-to-blank ratio of ~1100 to 1900.

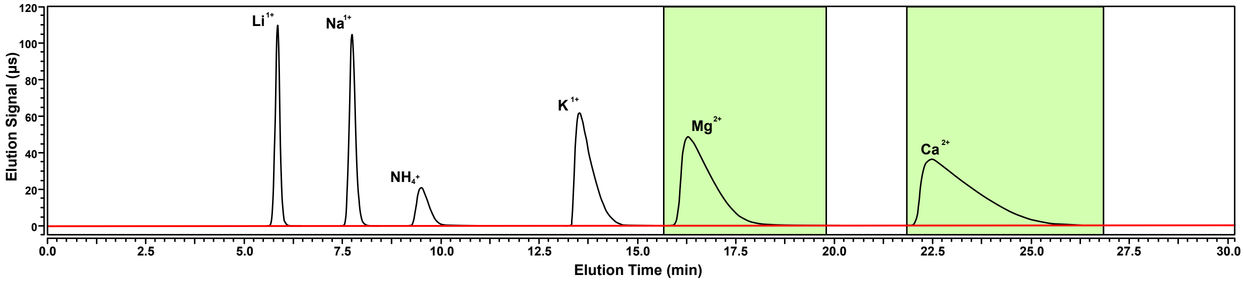

Figure 3.1 The elution of a 6-cation standard showing clean separation between Lithium, Li; Sodium; Na; Ammonia, NH_4; Potassium, K; Magnesium, Mg; Calcium, Ca. Green boxes enveloping Mg and Ca elution peaks show range of fraction collected eluant. The red horizontal bar represents the base-line signal, typically below 0.5 µS, microsiemens.

3.2 Mass spectrometry – magnesium isotopes

After chemical clean up, the Mg eluates were dried down and treated with ~ 1 ml of ultrapure 15 N HNO_3 and one drop of high purity 30% H_2O_2 to convert the eluted Mg from a hydroxide to a nitrate complex, and to destroy small amounts of co-eluted dissolved organic matter released from the columns. Purified sample solutions with ~1 ppm Mg in 0.3 N HNO_3 were measured using a Thermo-Fisher Scientific NEPTUNE multi-collector inductively-coupled plasma mass spectrometer (MC-ICP-MS) located in the Saskatchewan Isotope Laboratory (SIL). Sample measurements were conducted using a standard-bracketing technique to correct for instrumental mass fractionation of Mg isotopes and instrumental drift in the isotopic compositions of standards (Galy et al., 2003). Sample intensities (8-12 V on mass 24) were matched to within 5% of the intensity of an ultrapure Mg bracketing standard: Dead Sea Magnesium - DSM3 (Galy et al., 2003), or Saskatchewan Isotope Lab Magnesium - SIL-1. Data quality was monitored using the external CAM-1 standard (Galy et al., 2003) and an internal SpecPure ICP-MS standard. Reported δ^{26}Mg values of samples are averages of four repeated measurements of the same purified Mg solution performed during a single mass spectrometry session. A session represents a single, uninterrupted, individually tuned mass spectrometer run consisting of a finite number of samples bracketed by the DSM3 or SIL-1 standards.

$$\delta^{26}\text{Mg} = \frac{(^{26}\text{Mg}/^{24}\text{Mg})_{\text{Sample}} - (^{26}\text{Mg}/^{24}\text{Mg})_{\text{DSM3}}}{(^{26}\text{Mg}/^{24}\text{Mg})_{\text{DSM3}}} * 10^3 \qquad (3.1)$$

Mg isotope data (^{26}Mg/^{24}Mg) are reported as permil (‰) deviations of the sample ^{26}Mg/^{24}Mg relative to the ^{26}Mg/^{24}Mg of the DSM3 standard (Galy et al., 2003) as shown in Equation 3.1. The measurement uncertainty for each sample (Table 4.1) is calculated as two standard errors (SE) of the mean of up to four measurements, representing an estimate of the internal precision of that measurement. The external precision is based on the long-term reproducibility of the CAM-1 ($\delta^{26}Mg_{DSM3}$= −2.60‰ ± 0.10‰, n=70) and SpecPure standard ($\delta^{26}Mg_{DSM3}$= −3.78‰ ± 0.09‰, n=53) measured over many sessions (Figure 3.2). The values for these standards fall within the analytical uncertainties of the values reported from other laboratories (e.g., CAM-1: δ^{26}Mg = –

2.58‰ ± 0.14‰ in Galy et al., 2003; –2.62‰ ± 0.25‰ in Higgins and Schrag, 2010; –2.58‰ ± 0.14‰ in Kimmig 2017; –2.61‰ ± 0.08‰ Mavromatis et al., 2014; –2.60‰ ± 0.14‰ in Tipper et al., 2006; and –2.66‰ ± 0.14‰ in Tipper et al., 2008). Kimmig et al. (2017) reported –3.79‰ ± 0.10‰ for repeated analyses of SpecPure Mg, which compares favorably with −3.78‰ ± 0.09‰ obtained in this study.

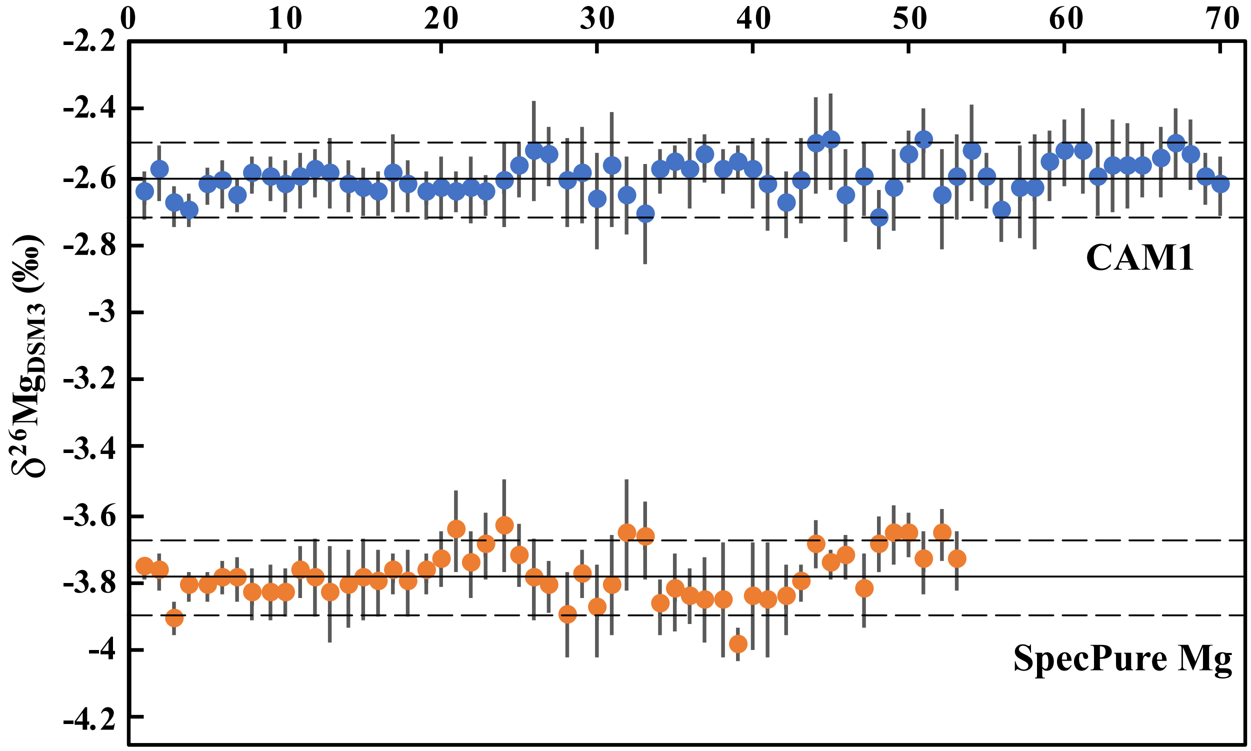

Figure 3.2 Long-term monitoring of CAM-1 (blue circles) and SpecPure (orange circles) Mg standards in the Saskatchewan Isotope Laboratory over the course of this study. Error bars (light gray vertical lines) are ± 2σ for each individual analysis, with a long-term mean value of CAM-1 = $\delta^{26}Mg_{DSM3}$ = –2.60‰ ± 0.10‰, n=70 and SpecPure Mg = $\delta^{26}Mg_{DSM3}$ = –3.78‰ ± 0.09‰, n=53. The solid horizontal black line shows the mean value and dashed lines indicate the 2σ error from the mean.

3.3 Strontium chemical separation and mass spectrometry

Strontium was purified from matrix ions using conventional gravity flow Savillex™ columns packed with AG® MP50 resin and HCl as the eluant. The $^{87}Sr/^{86}Sr$ ratio measurements were performed using a Thermo Scientific TRITON thermal ionization mass spectrometer (TIMS) housed in the Saskatchewan Isotope Laboratory. The reproducibility of the $^{87}Sr/^{86}Sr$ measurements is estimated from repeated analyses of SRM 987 performed over the course of this work, yielding 0.710272 ± 0.000006 (2 σ, n=9).

3.4 Stable C and O isotope measurements

Carbonate and oxygen isotope measurements were obtained using a Finnigan Kiel-IV carbonate preparation device directly coupled to a dual inlet Finnigan MAT 253 gas isotope ratio mass spectrometer housed in the Saskatchewan Isotope Laboratory. Carbonate powders (20-50 μg) were dissolved using five drops of anhydrous phosphoric acid for 500 seconds at 70°C. The evolved CO_2 was cryogenically purified before being passed to the mass spectrometer for analysis. Isotopic ratios were corrected for acid fractionation and ^{17}O contribution and reported in permil (‰) notation relative to Vienna Pee Dee Belemnite (VPDB). Data quality was monitored using SRM NBS-19 (average = $\delta^{13}C$ = 2.06‰ VPDB, n = 25; average = $\delta^{18}O$ = –2.22‰ VPDB, n = 25). The external precisions for $\delta^{13}C$ and $\delta^{18}O$ are ±0.05‰ and ±0.11‰, respectively (1σ), based on long term reproducibility of internal standards. $\delta^{18}O$ values are calculated using the following acid fractionation factors at 70°C: calcite = 1.008698 (Swart et al., 1991), and dolomite = 1.009926 (Rosenbaum and Sheppard, 1986).

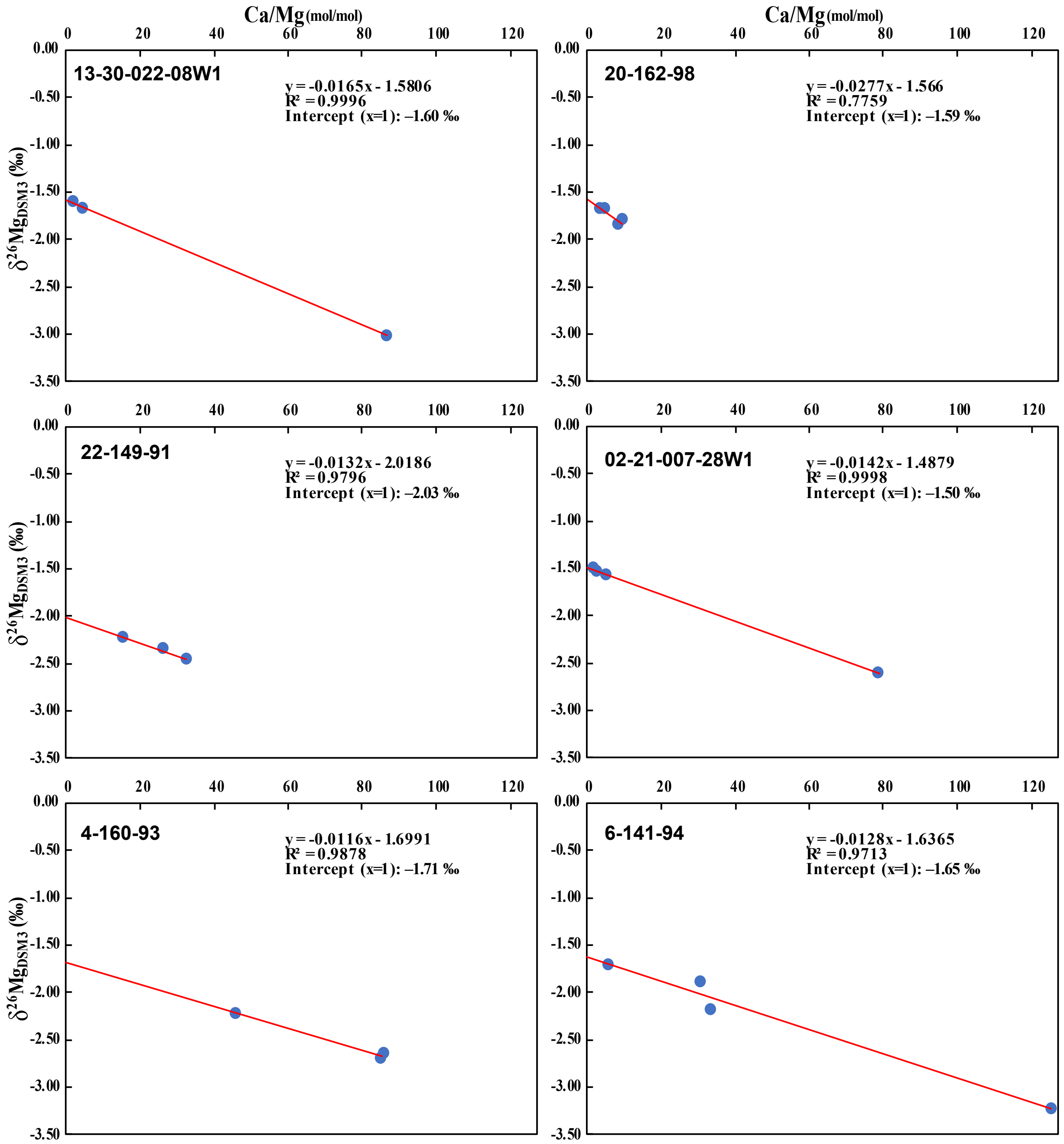

Figure 3.3 The δ^{26}Mg (‰) *vs.* Ca/Mg (mol/mol) cross-plots for sampled well cores where dolomitization is incomplete (molar Ca/Mg ≳ 1.0). Equations for the best fit lines are shown in addition to the R^2 values. Two component mixtures of dolomite and calcite plot as straight lines on this diagram. The δ^{26}Mg value for the dolomite end-member is calculated using the equation of the line when Ca/Mg = 1.

3.5 Mixing analysis to determine dolomite end-member for contour mapping

Dolomite δ^{26}Mg values from extensively dolomitized (Ca/Mg molar ratios $\cong$ 1.00) core intervals of the Winnipegosis are the average of the samples measured in the core. In studied cores where dolomitization is incomplete (molar Ca/Mg > 1.0), plots of δ^{26}Mg *vs.* Ca/Mg reveal linear relationships consistent with two-component mixing between limestone and dolomite (Figure 3.3) (e.g., Kimmig, 2017). In these cores, the δ^{26}Mg value of the dolomite end-member is calculated from the best-fit equation of the line for a Ca/Mg ratio of 1.0. Wherever possible, I selected the purest dolomite samples to conduct the ^{87}Sr/^{86}Sr analyses. Dolomite δ^{26}Mg values and ^{87}Sr/^{86}Sr ratios are plotted against their geographical coordinates on a map of the Elk Point Basin. The data were gridded and contoured using Surfer® 15 and interpolation was performed by a Kriging gridding method. Maps were also constructed for whole-rock δ^{13}C and δ^{18}O values, and Fe and Mn concentrations.

CHAPTER 4 – Results

Stable isotope (δ^{26}Mg, δ^{18}O, δ^{13}C) and ^{87}Sr/^{86}Sr data for all sampled carbonates are listed in Table 4.1. The end-member dolomite δ^{26}Mg values and ^{87}Sr/^{86}Sr ratios for each core interval can be found in Table 4.2. End-member dolomite δ^{26}Mg values for Lower Member Winnipegosis cores sampled from across the Williston Basin are plotted and contoured on an isopach map showing depths to the top of the Winnipegosis (Figure 4.1a). The map also shows the locations of the sampled cores and the outline of the depositional Elk Point Basin. The lowest values are found in the deep center of the Williston Basin in northwestern North Dakota (–2.03‰). Higher values are found towards the edges of the basin, reaching –1.34‰ in the outcrop belt in Manitoba.

Three samples of Type 1 dolomite from an Upper Member Winnipegosis mud mound in the Saskatoon area yielded an average δ^{26}Mg value of –1.55 ±0.01‰ (2se). Type 2 dolomite measured in the same core yielded –0.96‰, supporting different fluid origins for the two dolomite types. Type 1 dolomite yielded an average ^{87}Sr/^{86}Sr ratio of 0.70804 ±0.000008 (2se) (Table 4.1), which is consistent with Middle Devonian seawater as measured in the overlying Whitkow Anhydrite at the base of the Prairie Evaporite (Figure 2.3a) yielding 0.70789 (Table 4.1). Lower Member Winnipegosis (Type 2) dolomite ranges between 0.7079 and 0.7089 (average = 0.70825, n=26), with all but one sample recording ^{87}Sr/^{86}Sr above the ratio of Middle Devonian seawater (Figure 4.2a).

A map was prepared using ^{87}Sr/^{86}Sr ratios from the most dolomitized samples from each core (Figure 4.3a). It does not conform to the contour map of dolomite δ^{26}Mg in the Lower Member Winnipegosis, nor does it conform to the depositional outline of the Elk Point Basin. A closer look at the data reveals that six cores (Table 4.2) have low dolomite abundances and must be corrected to for Sr contributions from limestone. The corrected map (Figure 4.3b) shows higher ^{87}Sr/^{86}Sr ratios in dolomite in the deep center of the Williston basin.

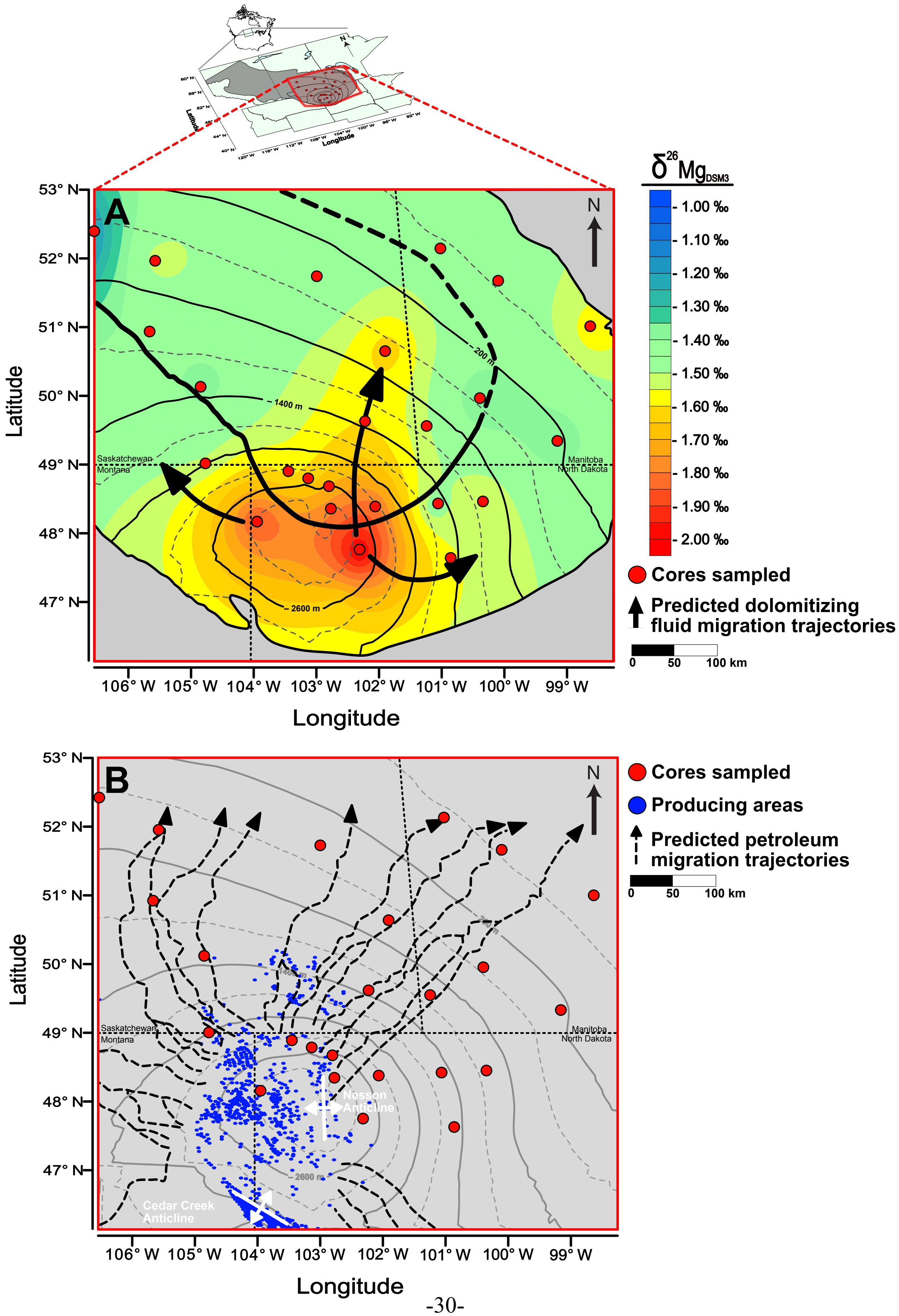
A
B
Latitude
Longitude
53° N
52° N
51° N
50° N
49° N
48° N
47° N
106° W
105° W
104° W
103° W
102° W
101° W
100° W
99° W
N
200 m
1400 m
2600 m
Saskatchewan
Montana
Manitoba
North Dakota
δ26MgDSM3
1.00 ‰
1.10 ‰
1.20 ‰
1.30 ‰
1.40 ‰
1.50 ‰
1.60 ‰
1.70 ‰
1.80 ‰
1.90 ‰
2.00 ‰
Cores sampled
Predicted dolomitizing fluid migration trajectories
0
50
100 km
Producing areas
Predicted petroleum migration trajectories
Nesson Anticline
Cedar Creek Anticline
Latitude
Longitude

Figure 4.1 (A) Shaded contour map of dolomite end-member δ^{26}Mg values within the Lower Member Winnipegosis in the Williston Basin. The erosional extent of the Middle Devonian Elk Point Basin demarcates the countering limits. Large black arrows interpreted flow direction of the dolomitizing fluids which are drawn at right angles to the contours. Thick black lines represent the divide between the central basin / mud mound facies and the surrounding platform facies (Modified after Fischer and Burke, 1987 and Jin and Bergman, 1999). See locations of sampled sites indicated by red circles. **(B)** Hydrostatic simulation of petroleum migration trajectories (black dotted lines) depicting migration of oil and gas up-dip from the deep center of the Williston Basin towards the outcrop belt in Manitoba (Khan et al., 2006). Blue dots represent Red River oil and gas production wells modified after Khan et al. (2006). Depth to the top of the Winnipegosis is represented by the isopach contours in solid and dashed lines (300 m spacing, max depth dashed contour line at 2900 m below sea level).

Sampled Fe and Mn concentrations in the Lower Member Winnipegosis dolomite ranged from 75 to 3226 ppm (average 640 ppm) and 32 to 296 ppm (average 106 ppm), respectively (Table 4.1) (Figure 4.2b). These are consistent with concentrations in Type 2 dolomite in the Saskatoon cores reported by Fu et al. (2006). Fe and Mn concentrations (Figure 4.2b) in the Upper Member Winnipegosis dolomite measured in this study are comparable to Type 1 dolomites reported by Fu et al. (2006) (Figure 4.2b). Lower Member dolomite Fe and Mn concentrations are plotted and contoured on a geological map of the study area, with the shape of the contours appearing to match the outline of the depositional Elk Point Basin (Figure 4.4c and 4.4b, respectively). This is in marked contrast to the contour map of dolomite δ^{26}Mg values, which aligns better with the isopach map of the Winnipegosis depths, which reflects subsidence of the Williston Basin. Lower Fe ($\lessapprox$ 250 ppm) and Mn ($\lessapprox$ 75 ppm) concentrations characterize the deeper waters of the central basin / mud mound facies. Higher concentrations of Fe ($\gtrapprox$ 500 ppm) and Mn ($\gtrapprox$ 95 ppm) characterize the surrounding shallow water platform facies. The finding that geographic patterns in the Fe and Mn concentrations correspond better to both the outline and depositional facies of the Elk Point Basin than the structure map of the Williston Basin, indicates that the Fe and Mn distributions in these dolomites are likely inherited from the originally deposited carbonates.

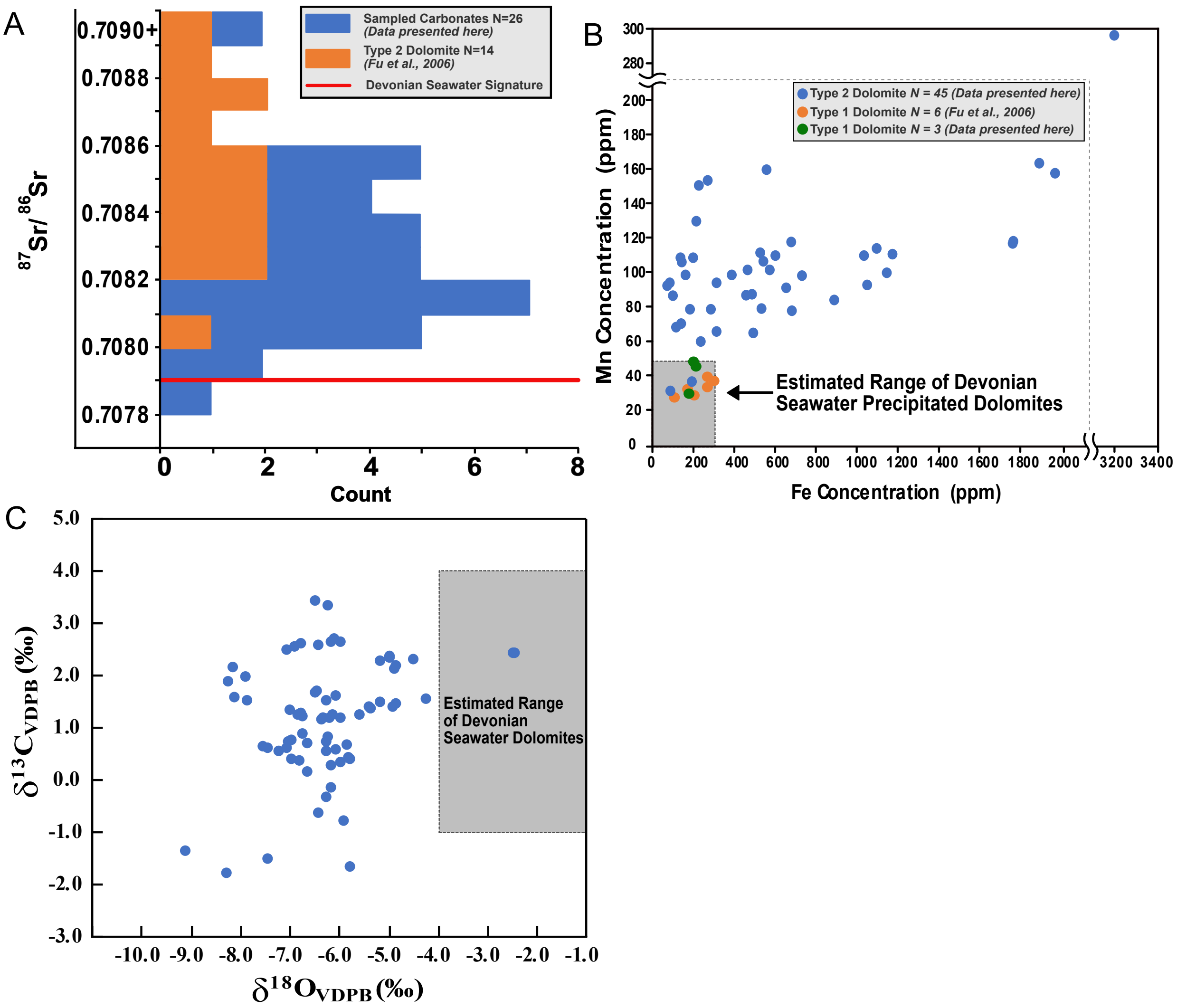

Figure 4.2 (A) Histogram of measured ^{87}Sr/^{86}Sr ratios from samples of Type 2 dolomite from the Lower Winnipegosis in blue (n=26). The histogram also includes Type 2 dolomite from Fu et al. (2006) in orange (n=14). The ^{87}Sr/^{86}Sr ratios in Type 2 dolomite are higher than middle Devonian seawater (solid red line). **(B)** Cross-plot of Mn *vs*. Fe concentrations (ppm) of Lower Member Winnipegosis dolomite in blue. Results show concentrations (Mn an Fe) that are higher than expected for dolomites precipitating from middle Devonian seawater. The cross-plot also has Type 1 dolomite from the Upper Winnipegosis in green (data from this study) and orange (data from Fu et al., 2006). Note the break in both the X and Y-axis. **(C)** Plot of δ^{18}O *vs*. δ^{13}C for the Lower Member Winnipegosis dolomites. Estimated range of Middle Devonian dolomite formed in seawater-derived pore fluids is constructed using literature values (cf. Fritz, 1971; Qing 1998).

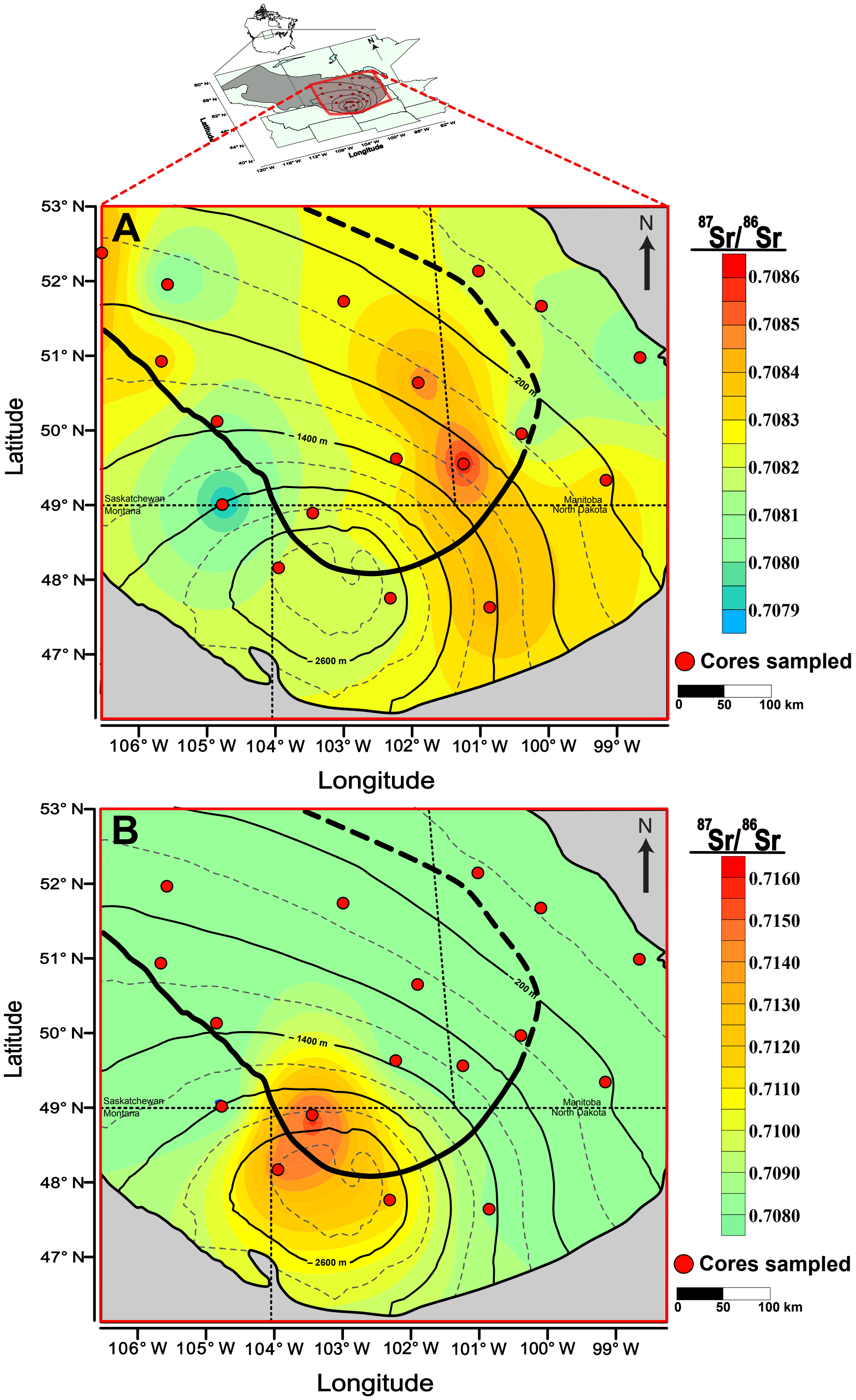
Latitude
Longitude
A
B
N
53° N
52° N
51° N
50° N
49° N
48° N
47° N
106° W
105° W
104° W
103° W
102° W
101° W
100° W
99° W
200 m
1400 m
2600 m
Saskatchewan
Montana
Manitoba
North Dakota
$^{87}Sr/^{86}Sr$
0.7086
0.7085
0.7084
0.7083
0.7082
0.7081
0.7080
0.7079
0.7160
0.7150
0.7140
0.7130
0.7120
0.7110
0.7100
0.7090
0.7080
Cores sampled
0
50
100 km

Figure 4.3 Shaded contour map of **(A)** $^{87}Sr/^{86}Sr$ ratios from the most dolomitized samples from each core, and **(B)** of corrected dolomite endmember $^{87}Sr/^{86}Sr$ ratios of the Lower Member Winnipegosis Formation. The erosional extent of the Middle Devonian Elk Point Basin demarcates the countering limits. Thick black line represents the divide between the central basin / mud mound facies and the surrounding platform facies (Modified after Fischer and Burke, 1987 and Jin and Bergman, 1999). See locations of sampled sites indicated by red circles. Depth to the top of the Winnipegosis is represented as an isopach overlay shown in solid and dashed lines (300 m spacing, max depth dashed contour line at 2900 m below sea level).

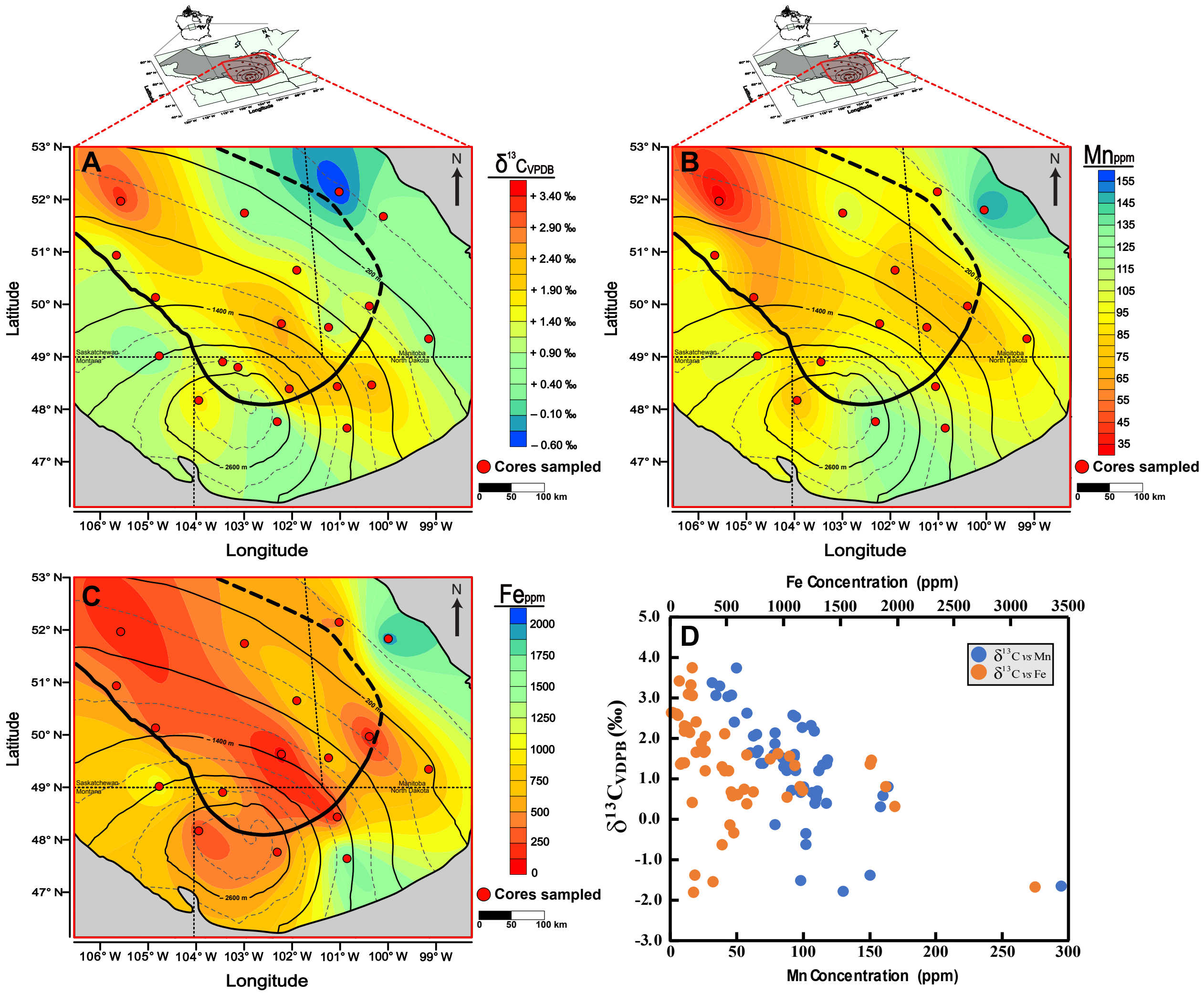

Figure 4.4 Shaded contour map of **(A)** $\delta^{13}C$ values, **(B)** Mn concentrations and **(C)** Fe concentrations of the Lower Member Winnipegosis. The erosional extent of the Middle Devonian Elk Point Basin demarcates the countering limits. Thick black line represents the divide between the central basin / mud mound facies and the surrounding platform facies (Modified after Fischer and Burke, 1987 and Jin and Bergman, 1999). See locations of sampled sites indicated by red circles. Depth to the top of the Winnipegosis is represented by the isopach contours in solid and dashed lines (300 m spacing, max depth dashed contour line at 2900 m below sea level). **(D)** Plot of $\delta^{13}C$ *vs*. Fe concentrations (ppm) (orange circles) and $\delta^{13}C$ *vs*. Mn concentrations (ppm) (blue circles) for the Winnipegosis dolomites.

The Lower Winnipegosis dolomites have $\delta^{18}O$ values ranging from –9.10 to –2.43‰ (average = –6.23‰, n = 68) (Appendix A – Supplementary Figure 1) and $\delta^{13}C$ values ranging from –1.83 to 3.38‰ (average = 1.07‰, n = 68) (Figure 4.2a) (Table 4.1). Dolomite $\delta^{13}C$ values of the Lower Member Winnipegosis are plotted and contoured on a map of the study area and like the Fe and Mn maps the contours align better with the outline and depositional facies of the Elk Point Basin, with higher $\delta^{13}C$ (Figure 4.4a) values in the central basin / mud mound facies (~ 3.00‰) and lower values in the surrounding platform facies (~ 0.50‰). The contour map of dolomite $\delta^{18}O$ values (Appendix A – Supplementary Figure 1) does not align with the outline of the Elk Point Basin (Figure 2.1b) or Williston Basin.

Table 4.1 Isotope and Elemental concentrations for the Winnipegosis carbonates and Whitkow anhydrites.

Sample Name	State/Province	Strata	Depth (m)	Latitude	Longitude	$\delta^{26}Mg_{DSM3}$ (‰)(± 2SE)	$^{87}Sr/^{86}Sr$ (± 2SE)	Ca/Mg (mol/mol)	Fe (ppm)	Mn (ppm)	$\delta^{18}O$ (‰)$_{VPDB}$	$\delta^{13}C_{Carb}$ (‰)$_{VPDB}$
13-27-008-2W2-1	SK	LW	1907	49.680947	-102.206765	-1.60 ± 0.02	0.708207 ± 0.000009	0.94	87	95	-6.88	2.52
13-27-008-2W2-2	SK	LW	1907	49.680947	-102.206765	-1.63 ± 0.03		0.96	75	94	-6.41	2.55
13-27-008-2W2-3	SK	LW	1907	49.680947	-102.206765	-1.62 ± 0.03		0.94			-7.03	2.44
13-27-008-2W2-4	SK	LW	1907	49.680947	-102.206765	-1.57 ± 0.01		0.95			-6.75	2.57
2-10-1-21W2-1	SK	LW	2733	49.015495	-104.730191	-1.54 ± 0.03	0.707880 ± 0.000007	0.98	1186	112	-7.01	0.68
2-10-1-21W2-2	SK	LW	2733	49.015495	-104.730191	-1.50 ± 0.01		0.99	1047	111	-7.20	0.52
2-10-1-21W2-3	SK	LW	2733	49.015495	-104.730191	-1.50 ± 0.02		1.02			-6.93	0.72
4-27-31-7W2-1	SK	LW	931	51.679600	-102.924981	-1.43 ± 0.03		1.20			-7.43	0.56
4-27-31-7W2-2	SK	LW	931	51.679600	-102.924981	-1.37 ± 0.01		1.00	687	119	-6.94	0.35
4-27-31-7W2-3	SK	LW	931	51.679600	-102.924981	-1.38 ± 0.03	0.708237 ± 0.000014	1.03	549	107	-6.63	0.65
4-27-31-7W2-4	SK	LW	931	51.679600	-102.924981	-1.47 ± 0.01		0.99	608	111	-7.05	0.58
10-34-23-27-W2-1	SK	LW	1568	51.002835	-105.691232	-1.40 ± 0.04		0.98			-6.18	1.16
10-34-23-27-W2-2	SK	LW	1568	51.002835	-105.691232	-1.45 ± 0.07		0.98	533	112	-5.93	1.16
10-34-23-27-W2-3	SK	LW	1568	51.002835	-105.691232	-1.44 ± 0.06	0.708311 ± 0.000007	1.00	319	95	-6.31	1.16
10-34-23-27-W2-4	SK	LW	1568	51.002835	-105.691232	-1.43 ± 0.04		0.97			-6.10	1.21
3-29-036-25W1-1	MB	LW	244	52.115389	-101.002788	-1.47 ± 0.03		0.97			-5.88	-0.82
3-29-036-25W1-2	MB	LW	244	52.115389	-101.002788	-1.45 ± 0.03	0.708152 ± 0.000010	1.45	392	99	-7.42	-1.57
3-29-036-25W1-3	MB	LW	244	52.115389	-101.002788	-1.48 ± 0.03		1.01	473	103	-6.40	-0.68
3-29-036-25W1-4	MB	LW	244	52.115389	-101.002788	-1.40 ± 0.02		1.00	579	103	-6.24	-0.38
4-27-011-22W1-1	MB	LW	863	49.947579	-100.413362	-1.42 ± 0.02		0.99	102	87	-5.34	1.32
4-27-011-22W1-2	MB	LW	863	49.947579	-100.413362	-1.30 ± 0.01		0.96	144	71	-4.90	1.36
4-27-011-22W1-3	MB	LW	863	49.947579	-100.413362	-1.31 ± 0.02	0.708097 ± 0.000007	1.00	118	69	-5.38	1.37
4-27-011-22W1-4	MB	LW	863	49.947579	-100.413362	-1.32 ± 0.02		0.93			-4.81	1.43
13-30-022-08W1-1	MB	LW	24	50.931009	-98.572228	-1.60 ± 0.03		2.04	3226	296	-5.75	-1.71
13-30-022-08W1-2	MB	LW	24	50.931009	-98.572228			39.89	219	131	-8.26	-1.83
13-30-022-08W1-3	MB	LW	24	50.931009	-98.572228	-3.01 ± 0.10		86.85	230	152		
13-30-022-08W1-4	MB	LW	24	50.931009	-98.572228	-1.67 ± 0.04	0.707986 ± 0.000006	4.38	274	155	-9.10	-1.40
2-156-82-1	ND	LW	2115	48.361558	-101.167782	-1.48 ± 0.03		0.95	145	107	-4.46	2.28
2-156-82-2	ND	LW	2115	48.361558	-101.167782	-1.49 ± 0.02		0.95	139	110	-4.82	2.14
2-156-82-3	ND	LW	2115	48.361558	-101.167782	-1.43 ± 0.02		0.94	164	100	-5.14	2.23
5-154-103-1	ND	LW	3637	48.192435	-103.957185	-1.91 ± 0.04	0.708157 ± 0.000018	3.49	290	79	-8.21	1.85
5-154-103-2	ND	LW	3637	48.192435	-103.957185			8.03	188	80	-8.14	2.12
5-154-103-3	ND	LW	3637	48.192435	-103.957185	-1.86 ± 0.06		4.58			-7.88	1.93
5-154-103-4	ND	LW	3637	48.192435	-103.957185	-1.89 ± 0.01		4.87			-8.08	1.54
20-162-98-1	ND	LW	3100	48.847664	-103.439244	-1.86 ± 0.04	0.708194 ± 0.000009	8.53	492	88	-6.31	1.15
20-162-98-2	ND	LW	3100	48.847664	-103.439244	-1.80 ± 0.02		9.80	469	87	-6.76	1.25
20-162-98-3	ND	LW	3100	48.847664	-103.439244	-1.68 ± 0.05		3.85	1109	115	-6.98	1.29
20-162-98-4	ND	LW	3100	48.847664	-103.439244	-1.69 ± 0.03		5.26			-6.81	1.20

Table 4.1 Cont.

Sample Name	State/Province	Strata	Depth (m)	Latitude	Longitude	δ^{26}Mg (‰)$_{DSM3}$	^{87}Sr/^{86}Sr (± 2se)	Ca/Mg (mol/mol)	Fe (ppm)	Mn (ppm)	δ^{18}O (‰)$_{VPDB}$	δ^{13}C$_{Carb}$ (‰)$_{VPDB}$
22-149-91-1	ND	LW	3520	47.712110	-102.313085	-2.23 ± 0.01	0.708145± 0.000011	15.53	564	161	-6.03	0.53
22-149-91-2	ND	LW	3520	47.712110	-102.313085	-2.46 ± 0.04		32.71	203	110	-5.77	0.38
22-149-91-4	ND	LW	3520	47.712110	-102.313085	-2.35 ± 0.03		26.48			-6.14	0.24
1-04-020-32W1-1	SK	LW	1085	50.682960	-101.860891	-1.63 ± 0.04	0.708352 ± 0.000003	0.98	691	79	-6.03	1.57
1-04-020-32W1-2	SK	LW	1085	50.682960	-101.860891	-1.65 ± 0.09	0.708541 ± 0.000007	0.97	901	85	-6.23	1.47
1-05-033-19W1-1	MB	LW	132	51.798959	-100.108691	-1.48 ± 0.05	0.708139 ± 0.000007	0.97	1911	165	-6.21	0.77
1-05-033-19W1-2	MB	LW	132	51.798959	-100.108691	-1.38 ± 0.02	0.708148 ± 0.000005	1.08	1991	159	-5.94	0.30
1-12-035-26W2-1	SK	LW	1119	51.985652	-105.577769	-1.56 ± 0.07	0.707990 ± 0.000006	0.98	196	38	-6.20	3.29
1-12-035-26W2-2	SK	LW	1119	51.985652	-105.577769	-1.51 ± 0.04	0.708007 ± 0.000006	0.91	91	32	-6.46	3.38
02-21-007-28W1-1	MB	LW	1447	49.578987	-101.221962	-1.53 ± 0.02		3.07			-5.57	1.21
02-21-007-28W1-2	MB	LW	1447	49.578987	-101.221962	-2.61 ± 0.04		78.76			-7.51	0.60
02-21-007-28W1-3	MB	LW	1447	49.578987	-101.221962	-1.50 ± 0.02	0.708568 ± 0.000007	1.83	1063	94	-4.20	1.51
02-21-007-28W1-4	MB	LW	1447	49.578987	-101.221962	-1.57 ± 0.01	0.708195 ± 0.000006	5.53	541	80	-6.13	-0.19
04-02-014-21W2-1	SK	LW	1883	50.136327	-104.778990	-1.37 ± 0.03	0.708074 ± 0.000006	0.99	318	67	-6.44	1.66
04-02-014-21W2-2	SK	LW	1883	50.136327	-104.778990	-1.36 ± 0.08	0.708093 ± 0.000007	1.03	241	61	-6.45	1.63
16-33-004-13W1-1	MB	LW	680	49.353290	-99.159122	-1.33 ± 0.05		1.01	741	99	-5.82	0.63
16-33-004-13W1-2	MB	LW	680	49.353290	-99.159122	-1.36 ± 0.05	0.708282 ± 0.000006	1.08	662	92	-6.25	0.70
4-160-93-2	ND	LW	3326	48.716809	-102.711205	-2.23 ± 0.05		46.21			-6.71	0.84
4-160-93-3	ND	LW	3326	48.716809	-102.711205	-2.72 ± 0.04		85.70			-6.32	1.11
4-160-93-4	ND	LW	3326	48.716809	-102.711205	-2.66 ± 0.07		85.97			-6.72	1.17
6-141-94-1	ND	LW	3408	47.062611	-102.633313	-2.20 ± 0.02		33.40			-6.79	0.33
6-141-94-2	ND	LW	3408	47.062611	-102.633313	-3.24 ± 0.02		125.33			-6.22	0.50
6-141-94-3	ND	LW	3408	47.062611	-102.633313	-1.72 ± 0.02		5.96			-5.76	0.36
6-141-94-4	ND	LW	3408	47.062611	-102.633313	-1.88 ± 0.04		30.64			-6.62	0.12
26-149-80-1	ND	LW	2138	47.690531	-100.877371	-1.55 ± 0.10	0.708317 ± 0.000008	3.79	1781	118	-5.34	1.33
26-149-80-2	ND	LW	2138	47.690531	-100.877371	-1.56 ± 0.07	0.708505 ± 0.000006	3.45	1783	119	-5.14	1.44
5-161-95-2	ND	LW	3135	48.805962	-103.029115	-1.64 ± 0.07		3.03			-7.85	1.49
16-158-75-1	ND	LW	1466	48.399503	-102.068055	-1.83 ± 0.05		1.26			-2.45	2.39
16-158-75-2	ND	LW	1466	48.399503	-102.068055	-1.81 ± 0.04		1.21			-2.43	2.40
29-157-88-1	ND	LW	3070	48.503399	-100.360764	-1.54 ± 0.02		0.96			-4.94	2.31
29-157-88-2	ND	LW	3070	48.503399	-100.360764	-1.59 ± 0.07		0.91			-4.96	2.33
13-34-004-09W2-1	SK	WA	2402	49.346174	-103.147107		0.707885 ± 0.000006					
13-34-004-09W2-2	SK	WA	2402	49.346174	-103.147107		0.707886 ± 0.000007					
12-30-38-7W3-1	SK	UW	1081	52.298597	-107.000080	-1.56± 0.04	0.708030 ± 0.000007	0.90	205	50		
12-30-38-7W3-2	SK	UW	1087	52.298597	-107.000080	-1.54± 0.09	0.708034 ± 0.000006	0.96	212	47		
12-30-38-7W3-3	SK	UW	1090	52.298597	-107.000080	-1.56± 0.04	0.708044 ± 0.000008	0.89	177	35		
12-30-38-7W3-10	SK	LW	1162	52.298597	-107.000080	-0.95± 0.02	0.708488 ± 0.000008	0.90	965	95		
12-30-38-7W3-11	SK	LW	1164	52.298597	-107.000080	-0.96± 0.04	0.708947 ± 0.000010	0.98	1158	101		

Table 4.1 Cont.

Sample Name	**State/Province**	**Strata**	**Depth** (m)	**Latitude**	**Longitude**	**δ^{26}Mg** (‰)$_{DSM3}$	**^{87}Sr/^{86}Sr** (± 2se)	**Ca/Mg** (mol/mol)	**Fe** (ppm)	**Mn** (ppm)	**δ^{18}O** (‰)$_{VPDB}$	**δ^{13}C$_{Carb}$** (‰)$_{VPDB}$
12-30-38-7W3-12	SK	LW	1166	52.298597	-107.000080	-0.96± 0.04	0.708407 ± 0.000008	0.90	1834	107		

MB, Manitoba; SK, Saskatchewan; ND, North Dakota; LW, Lower Winnipegosis Member; WA, Whitkow Anhydrites; UM, Upper Winnipegosis Member; DMS3, Dead Sea Magnesium 3.

Table 4.2 Isotope data of the Lower Winnipegosis Stoichiometric dolomite end-member values.

Core Name	State/Province	Depth (m)	Latitude	Longitude	δ^{26}Mg Dolomite (‰)$_{DSM3}$	^{87}Sr/^{86}Sr
111/13-27-008-02W2; 092A046	SK	1907	49.680947	-102.206765	-1.60	0.708207†
101/02-10-001-21W2; 091B118	SK	2733	49.015495	-104.730191	-1.51	0.707880†
101/04-27-031-07W2; 058B026	SK	931	51.679600	-102.924981	-1.41	0.708237†
101/10-34-023-27W2; 069A042	SK	1568	51.002835	-105.691232	-1.43	0.708311†
101/01-04-020-32W1; 055H112	SK	1085	50.682960	-101.860891	-1.64	0.708447†
101/01-12-035-26W2; 069A061	SK	1119	51.985652	-105.577769	-1.53	0.707999†
101/04-02-014-21W2; 060G021	SK	1883	50.136327	-104.778990	-1.36	0.708084†
101/12-30-038-07W3; 067L038	SK	1165	52.298597	-107.000080	-0.96	0.708614†
100/03-29-036-25W1; 2548	MB	244	52.115389	-101.002788	-1.45	0.708152†
100/04-27-011-22W1; 1228	MB	863	49.947579	-100.413362	-1.34	0.708097†
100/13-30-022-08W1	MB	24	50.931009	-98.572228	-1.60	0.708107‡
102/01-05-033-19W1	MB	132	51.798959	-100.108691	-1.43	0.708144†
100/02-21-007-28W1; 91	MB	1447	49.578987	-101.221962	-1.50	0.708388‡
100/16-33-004-13W1; 609	MB	680	49.353290	-99.159122	-1.35	0.708282†
NESE 02-156-82; 4992	ND	2115	48.361558	-101.167782	-1.47	
SWNE 05-154-103; 4597	ND	3637	48.192435	-103.957185	-1.89	0.714083‡
NWNW 20-162-98; 12318	ND	3100	48.847664	-103.439244	-1.59	0.715989‡
SENW 22-149-91; 793	ND	3520	47.712110	-102.313085	-2.03	0.711582‡
SWNW 04-160-93; 12933	ND	3326	48.716809	-102.711205	-1.71	
SENE 06-141-94; 505	ND	3408	47.062611	-102.633313	-1.65	
SESW 26-149-80; 8993	ND	2138	47.690531	-100.877371	-1.56	0.708834‡
NENE 05-161-95; 5246	ND	3135	48.805962	-103.029115	-1.64	
SWSW 16-158-75; 5281	ND	1466	48.399503	-102.068055	-1.82	
NWNE 29-157-88; 11872	ND	3070	48.503399	-100.360764	-1.56	

MB, Manitoba; SK, Saskatchewan; ND, North Dakota; DSM3, Dead Sea Magnesium 3; †, Measured ^{87}Sr/^{86}Sr ratios; ‡, Calculated ^{87}Sr/^{86}Sr ratios.

CHAPTER 5 – Discussion

The following sections discuss the trace element and stable isotopic data from the sampled carbonates while respecting the susceptibility of each element to resetting during dolomitization (Figure 1.1). The discussion will start with interpretations of $\delta^{13}C_{Carb}$ values and Fe and Mn concentrations; here, I will argue that these signatures reflect rock buffered diagenetic conditions. In other words, dolomitization did not destroy the original signatures. By contrast, carbonate δ^{26}Mg and δ^{18}O values and ^{87}Sr/^{86}Sr ratios reflect fluid buffered diagenetic conditions and therefore can be used to develop a model of dolomitization for the Lower Member Winnipegosis dolomite.

5.1 Interpretation of the $\delta^{13}C_{Carb}$ map for the Lower Member Winnipegosis dolomite

Lower Member Winnipegosis dolomite exhibits a ~ 4.00‰ variation in δ^{13}C values across the Elk Point Basin (Table 4.1). The highest δ^{13}C values are found in the deeper waters of the central basin / mud mound facies (2.50 to 3.00‰). The surrounding shallow-water shelf environments exhibit lower δ^{13}C values (1.00 to –0.50 ‰). As there is no evidence that dolomitization altered the δ^{13}C value of the original carbonate sediment (e.g., Fu et al., 2006), it may be concluded that the geographic pattern of δ^{13}C values observed in the Lower Member Winnipegosis dolomite was inherited from the originally deposited carbonate sediment.

Facies dependent patterns in sedimentary δ^{13}C values have been reported before in C-cycling studies of ancient epicontinental seas. Holmden et al. (1998) reported a ~4‰ variation in limestones deposited across the Late Ordovician Mohawkian Sea in the submerged Midcontinent region of North America. They interpreted their findings in terms of local C-cycling effects (Patterson and Walter, 1995; Holmden et al., 1998; Panchuk et al. (2005, 2006; Melchin and Holmden, 2006; Fanton and Holmden, 2007; Immenhauser et al., 2008; Swart 2008; Holmden et al., 2012). There are a number of ways that local C-cycling effects can become manifested in carbonate sediment. Panchuk et al. (2006) used a quantitative box model to determine under what conditions a gradient in sedimentary $\delta^{13}C$ values could reflect a seawater gradient in the $\delta^{13}C$ values of dissolved inorganic carbon (DIC). They concluded that large fluxes of isotopically light carbon from continental runoff could create a gradient where there is a circulation restriction between epeiric seas and oceans.

Swart (2008) reported that platform sediments from the Bahamas are 3–4‰ enriched in ^{13}C compared to pelagic carbonate sediments deposited in deeper waters of the adjacent open ocean. He also found gradients in $\delta^{13}C$ values in peri-platform sediments draping the margins of the Bahamas platform. He attributed these findings to a predominance of aragonite deposition on the platform, which typically yields $\delta^{13}C$ values that are 2–3‰ more positive than calcite precipitated under similar conditions (Emrich et al., 1970; Romanek et al., 1992; Rubinson and Clayton, 1969), and the gradients in peri-platform sediments to mixing between aragonite and calcite. He also noted, however, that the mineralogical effect could not explain the highest $\delta^{13}C$ values of aragonite on the platform, indicating that ^{13}C-enriched pools of DIC must exist locally and transiently in platform waters that are not in equilibrium with atmospheric CO_2. Elevated ^{13}C could result from episodically intense periods of photosynthesis during which isotopically light DIC is fixed into organic matter, leaving the residual pool of DIC higher in $\delta^{13}C$ and higher in pH, thus facilitating carbonate precipitation. A similar local-scale C-cycling effect was proposed to explain higher $\delta^{13}C$ values in the nearshore regions of shallow epicontinental seas during the Hirnantian glaciation (Holmden et al., 2012). Kimmig and Holmden (2017) later presented Mg and Ca isotope evidence supporting an increase in aragonite precipitation during the glacio-eustatically controlled Hirnantian sea-level low stand, indicating that a change in carbonate polymorph mineralogy may have also contributed to the high sedimentary $\delta^{13}C$ values in nearshore settings at this time.

The gradient in $\delta^{13}C$ values found in in this study differs from the examples above in that the carbonates with the highest $\delta^{13}C$ values belong to the deeper waters of the central basin /mud mound facies, rather than the shallow waters of the surrounding platform. These deep waters were likely hypersaline, prompting consideration of the role that elevated salinity may have played in creating a pool of ^{13}C-enriched waters in the deep part of the basin. For example, evaporation of seawater is known to cause degassing of isotopically light CO_2, which generates an enrichment of ^{13}C in the residual pool of DIC (e.g., Stiller et al., 1985; Horton et al., 2016) (Figure 4.4a). It is therefore possible that the high sedimentary $\delta^{13}C$ values of the Lower Member Winnipegosis carbonates deposited in the central basin / mud mound facies indicates that deep waters were salinity stratified at this time. Alternatively, aragonite may have been deposited in the central basin/mud mound facies and calcite on the shelves, with the aragonite subsequently inverting to calcite in a closed diagenetic system.

5.2 Interpretation of the Fe and Mn concentration maps for the Lower Member Winnipegosis dolomite

Fu et al. (2006) noted that Fe and Mn concentrations in Type 2 dolomite from the Lower Member Winnipegosis were much higher than in Type 1 dolomite from the Upper Member Winnipegosis. They interpreted this finding as evidence that Type 2 dolomite formed during deep burial. Indeed, it has been widely reported that high Fe and Mn concentrations typify late-diagenetic burial dolomites (cf. Land 1985; Warren, 2000) due to the fact that Fe and Mn have very low concentrations in seawater (~2 ppb and ~0.3 ppb respectively for modern-day seawater) and much higher concentrations in anoxic sedimentary pore-fluids. Although the reasoning is sound, the maps of Mn and Fe concentrations show elevated concentrations in the platform facies of the Saskatchewan sub-basin (Figures 4.3b, 4.3c) strongly suggesting a depositional origin for the Fe and Mn distribution in the Lower Member Winnipegosis. I, therefore, propose that the Fe and Mn concentrations in the Lower Member Winnipegosis dolomite were inherited from the precursor carbonate and that the higher Fe and Mn concentrations in the platform facies is due to local runoff from the surrounding land surfaces.

An additional process which may have added Fe and Mn to the Elk Point sea is atmospheric deposition, which is a major source of these sparingly soluble metals to the open oceans (Duce and Tindale, 1991; Fung et al., 2000; Spokes et al., 2001). In the modern-day, prevailing winds blow Saharan mineral dust westward over the tropical North Atlantic (Williams et al., 2016), reaching as far as the Great Bahama Banks where dust deposition is responsible for elevated levels of Fe in the carbonate sediments (Swart et al., 2014). In the Middle Devonian, it has been suggested that easterly trade winds paralleled the palaeoequator (Witzke and Heckel, 1988; Wendte, 1992), highlighting the possible role of atmospheric deposition as a source of Fe and Mn to the region, where it could then be washed into the Elk Point Sea in runoff following precipitation events (Figure 4.4b and 4.3c).

5.3 Origin and significance of the basin-scale gradient in δ^{26}Mg values

5.3.1 Rayleigh fractionation effects

The similarity between the contour map of dolomite δ^{26}Mg values and the isopach map of Winnipegosis depth from the surface (Figure 4.1a) implies that Type 2 dolomite formed after subsidence tilted the Winnipegosis towards the center of the basin in northeastern North Dakota (Figure 2.1). The increase in dolomite δ^{26}Mg values (Figure 4.1a) with increasing distance from the center of the basin is consistent with Rayleigh fractionation of Mg-bearing fluids during their migration up the stratigraphic dip of the Lower Member Winnipegosis beds (cf., Kimmig, 2017). But the relatively small range of fractionation observed (~1.0‰) over the considerable distance of implied fluid flow (~400 km), the per mil level fractionation factor (Equation 1.2), and the likelihood that dolomite will continue to exchange Mg with the migrating fluid removing any transport related Rayleigh fractionation effects, suggest that a simple distillation model cannot explain these findings.

Building on a water-rock interaction model by Ahm et al. (2018), and similar contributions by others (Banner and Hanson, 1990; Blättler et al., 2015; Fantle and Higgins, 2014), I use a numerical model to simulate deep burial dolomitization. The model is constructed as a 1-D system of boxes that represents the porous flow path of the Lower Member Winnipegosis carbonates. Although the conceptual framework of this model is a simplification of the complex geometry of fluid flow, it can be used to study how gradients in δ^{26}Mg values may form in dolomite bodies under different conditions.

Model runs simulating replacement dolomitization (Equation 1.1) depict reaction fronts that move through the rock in the direction of fluid flow, as shown by the blue curve in Figure 5.1. Behind the reaction front, the original limestone is fully dolomitized. Ahead of the reaction front, the limestone remains undolomitized (Figure 5.1a). In the region of the reaction front, dolomite records Rayleigh fractionation of Mg isotopes (e.g., Figure 5.1b), with δ^{26}Mg values increasing in the direction of fluid flow as the concentration of dolomite decreases. In this model run, dolomite does not continuously react with the fluid Mg. In time the reaction front migrates away from the source of the Mg and the fluid (Figure 5.1a-b). If the flow were to stop at any time, a gradient of increasing δ^{26}Mg values would be preserved in the reaction front region where the concentration of dolomite decreases in the direction of fluid flow. However, behind the reaction front the dolomite body becomes increasingly uniform in δ^{26}Mg with time, eventually approaching the value of the initial dolomitizing fluid (–0.8‰), except for a region closest to the source of Mg and fluid where a fossilized reaction front will be recorded in carbonate that is 100% dolomitized. This result is analogous to a closed system Rayleigh fractionation experiment where the Mg in the fluid has been exhausted, and the accumulated Mg in the dolomite obtains the δ^{26}Mg value of the dolomitizing fluid at its source as a reflection of mass conservation. The net result is a dolomite body that records the δ^{26}Mg value of the dolomitizing fluid directly without fractionation (Figure 5.1d), except for at the margins of the dolomite body near the source of the Mg bearing fluids and in the extreme margins of the dolomite body perpendicular to the flow. The length scale of the gradients or reaction fronts at margins in this model can be made larger by simulating faster fluid flow rates and slower reaction rates, simulating conditions that allowing the reactive Mg to flow further along the flow path before complete exhaustion. Reactive transport modeling of dolomitization using realistic estimates of fluid flow and variable dolomite reaction rates, however, have only produced reaction front length scales ranging between ~25 m and ~30,000 m (Whitaker and Xiao, 2010; Wilson et al., 1990; Yapporova et al. 2017). This is substantially narrower than the observed ~400 km gradient in dolomite δ^{26}Mg values found in this study in the Lower Member Winnipegosis in the Williston Basin.

Keeping the model framework that same, a more realistic scenario would be to allow the dolomite already formed along the flow path to back-react with the fluid Mg. Numerous studies have shown that it is not dolomite that initially forms by Equation 1.1, but rather, very high magnesian calcite (VHMC) (Kaczmarek and Thornton, 2017), or proto-dolomite, that is more soluble than dolomite due to excess Ca and non-ideal cation ordering (Navrotsky and Capobianco, 1987; Chai et al., 1995; Drits et al., 2005; Jones, 2013). Over time, proto-dolomite is transformed to stoichiometric dolomite (Ca/Mg = 1.0) by acquiring additional Mg from pore fluids or shedding excess Ca (Nordeng and Sibley, 1994; Kaczmarek and Thornton, 2017). This phenomenon, known as Ostwald ripening (Nordeng and Sibley, 1994) describes how amorphous or poorly crystalline minerals will slowly increase in crystallinity over time. Li et al. (2015) showed that a "proto-dolomite" prepared with a ^{25}Mg-enriched isotopic composition nearly completely exchanged Mg isotopes with an isotopically "normal" tracer solution in 12–22 days at temperatures between 130ºC and 230ºC, with faster exchange rates occurring at higher temperatures, equivalent to deeper burial.

A new model simulating replacement dolomitization (Equation 1.1) was run, shown by the black curve in Figure 5.1. This time the dolomite formed behind the reaction front was allowed to continuously react with the fluid at a prescribed reaction rate that was lower than the initial reaction rate used to form proto-dolomite by replacement of limestone in the reaction front region (Figure 5.1). At progressively higher cumulative water-rock ratios (Figure 5.1 a-d), the final δ^{26}Mg value of the dolomite again approaches the fluid δ^{26}Mg value, but this time offset by the –1.2‰ fractionation factor, yielding –2.0‰. The required cumulative water-rock volumes required to reach equilibrium between the dolomite and original fluid Mg depends on the susceptibility of proto-dolomite to Mg exchange at the temperature of the fluid. If the fluid flow system were stalled at some point before full equilibration, a much broader spatially defined gradient would be preserved in the dolomite body than in the first scenario, with increasing δ^{26}Mg in the direction of fluid flow (Figure 5.1d). This appears to offer a more promising mechanism for producing large fossilized reaction fronts in vast dolomite bodies.

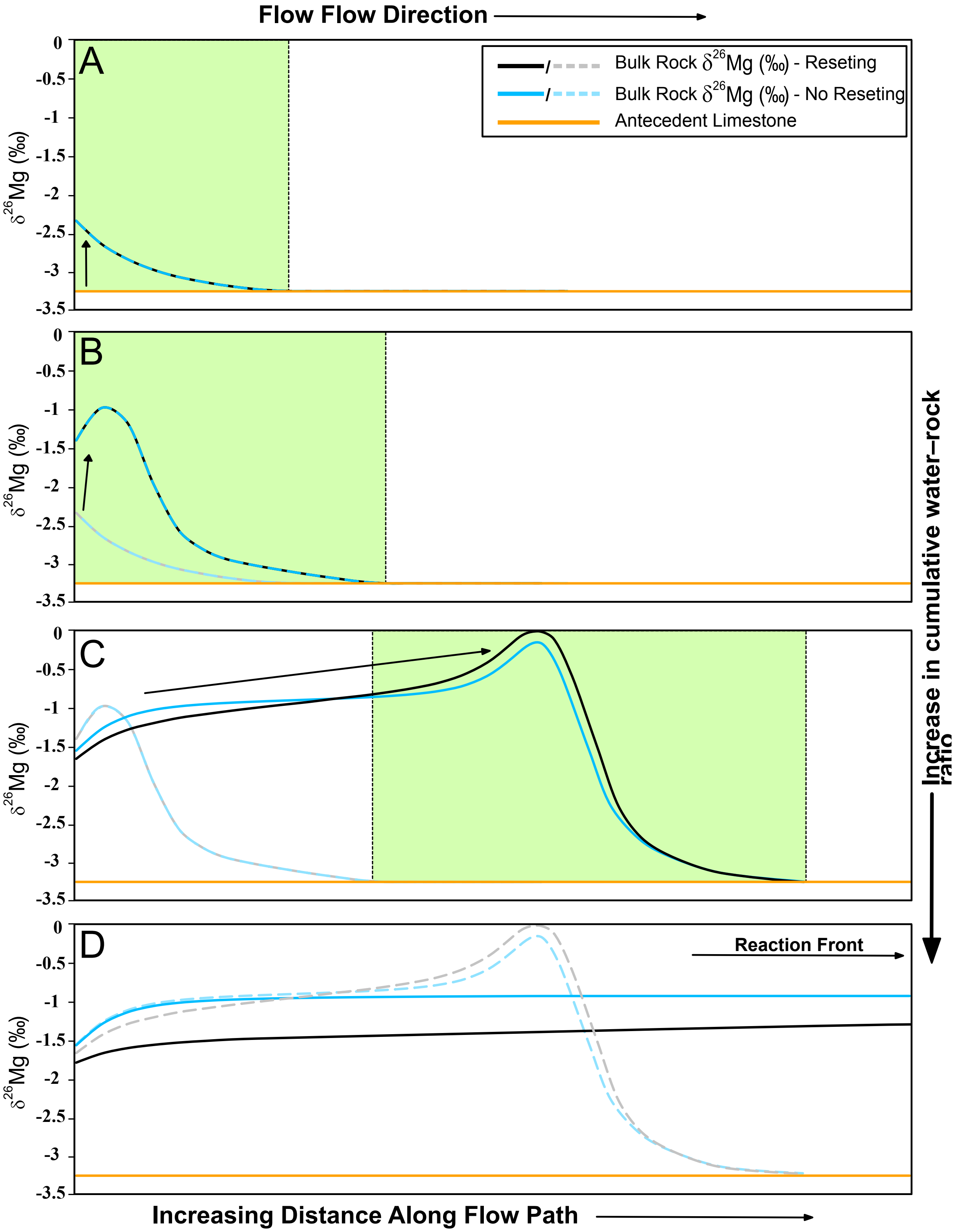
Flow Flow Direction
A
B
C
D
0
-0.5
-1
-1.5
-2
-2.5
-3
-3.5
δ26Mg (‰)
Bulk Rock δ26Mg (‰) - Reseting
Bulk Rock δ26Mg (‰) - No Reseting
Antecedent Limestone
Reaction Front
Increase in cumulative water–rock ratio
Increasing Distance Along Flow Path

Figure 5.1 Water-rock interaction model (modified after Ahm et al., 2018) depicting the transformation of limestone to dolomite by the passage of Mg bearing pore fluids during fluid flow. The initial δ^{26}Mg value of the limestone is –3.20‰ (orange line). The δ^{26}Mg value of the dolomitizing fluid is –0.80‰. Two model runs are shown: (1) dolomite does not exchange Mg with pore fluids after it forms (blue line), and (2) dolomite continuously exchanges Mg with pore fluids after it forms (black line). Panels A through D depict reaction progress through increased cumulative water-rock ratios. By panel D, the reaction front has migrated out of the frame. In model run (1), once the reaction front passes, the dolomite formed in its wake records a uniform δ^{26}Mg value, with the exception of a small rise in δ^{26}Mg values limited to the region nearest to the source of fluid flow (and another one out of the frame where the reaction front is characterized by decreasing dolomite concentration). In modeled run (2), once the reaction front passes, dolomite continues to exchange Mg with the fluid producing a gradient of increasing δ^{26}Mg values in the direction of fluid flow. This gradient is slowly removed at higher cumulative water-rock volumes (A-D) to eventually produce a dolomite body with a uniform δ^{26}Mg value of –2.0‰, which is in equilibrium with the fluid δ^{26}Mg value of –0.8‰, reflecting the applied fractionation factor of –1.20‰ at 90ºC (Li et al., 2015).

5.3.2 Temperature effects

Gradients in dolomite δ^{26}Mg values could also be produced by temperature changes occurring along the flow path of the dolomitizing fluids. The temperature dependence of the dolomite fractionation factor is given in Equation 1.2 (Li et al., 2015). If the temperature of the fluid changes along the flow path, then a gradient in dolomite δ^{26}Mg values will form as a result of the change in the fractionation factor. Consider, for example, an initially hot fluid that is flowing slowly enough to thermally equilibrate with cooler rocks during its ascent. If the δ^{26}Mg value of the fluid is constant at the source, then dolomite formed at progressively lower temperatures will record lower δ^{26}Mg values from the center to the edge of the basin, which is not what I observe (Figure. 4.1a). If descending fluids warmed in response to geothermal heating, this too would create a gradient of increasing dolomite δ^{26}Mg values with increasing depth, which again does not match the observations.

5.3.3 Mixing effects

Mixing can generate gradients in dolomite δ^{26}Mg values. As a case in point, Type 1 (–1.55‰) and Type 2 (–0.96‰) dolomite in this study have different δ^{26}Mg values (Table 4.1) (see core 12-30-38-7W3-1, Table 1). Mixtures of the two dolomite types could in principle generate gradients in bulk dolomite δ^{26}Mg values if the mixing fractions are spatially controlled. This kind of mixing could be verified through petrographic examination, and as such it cannot explain the basin-scale gradient in δ^{26}Mg values in the Lower Member Winnipegosis because this dolomite body is composed entirely of Type 2 dolomite, based on higher than seawater ^{87}Sr/^{86}Sr ratios. On the other hand, mixing effects may be cryptic in dolomites that have undergone partial exchange of Mg with younger fluids of different isotopic composition and temperature than the fluid from which the original dolomite formed. Mixing has the potential to develop large gradients in δ^{26}Mg values in large dolomite bodies.

5.3.4 A mixing interpretation for basin-scale gradients in dolomite δ^{26}Mg values in the Lower Member Winnipegosis Formation

The proposed mixing model has two variants: (1) Type 2 dolomite formed by replacement of original limestone, where dolomite that forms behind the reaction front continuously exchanges Mg, as described above (Figure 5.1), and (2) Type 2 dolomite formed by re-equilibration of Type 1 proto-dolomite. As the first model has been covered above, I will focus on the second model (2) in this section, which has the greater potential of the two to form large gradients in dolomite δ^{26}Mg values. Moreover, this model presents a scenario that would seem to be universally relevant to sedimentary basins worldwide, as it allows proto-dolomite to form early from Mg-bearing seawater fluids at low temperatures, and later recrystallize during burial in the presence of Mg-bearing formation waters at higher temperatures.

Indeed, in the present study, it is difficult to imagine a scenario whereby the Upper Member Winnipegosis could be dolomitized by brines filtering down through the mud mounds, and not dolomitize the Lower Winnipegosis as well, given that it conformably underlies the mud mound, is just 7-16 m thick, and is in turn underlain by the Ashern aquitard — a relatively impermeable unit which would have caused the sinking brines to spread laterally along the length of the Lower Member beds.

For simplicity, I assume that Type 1 proto-dolomite was initially uniform in its δ^{26}Mg value (–1.55‰) and that the Lower Member Winnipegosis was initially similarly composed of Type 1 dolomite as the Upper Member, with Middle Devonian ^{87}Sr/^{86}Sr ratios implying dolomitization by seawater or evaporatively concentrated seawater at high water-rock ratios. Subsidence then tilted the Winnipegosis beds towards the center of the basin in North Dakota, accounting for the fact that the Mg isotopic map resembles the isopach map of depths to the top of the Winnipegosis. Next, I estimate the δ^{26}Mg values for Type 1 and Type 2 dolomitizing fluids using the Mg isotope paleotemperature equation (Equation 1.2) (Li et al., 2015). Based on an assumed temperature of 30ºC and the –1.55‰ value for Type 1 dolomite, the δ^{26}Mg value of Middle Devonian seawater in the Elk Point Basin is estimated to be 0.15‰. Due to the long residence time of Mg in the oceans (~13 Ma) (Berner and Berner, 1996), seawater is expected to have a uniform δ^{26}Mg value over the depositional time frame of the studied carbonates (Tipper et al., 2006; Young and Galy, 2004). In fact, 0.15‰ is typical of early Paleozoic seawater more generally (Li et al., 2015) (Figure 5.2). Using the δ^{26}Mg value for Type 2 dolomite from the deep center of the basin (~ –2.0‰), and an assumed temperature of 90ºC, yields –0.8‰ for the dolomitizing Type 2 fluid. I chose the deepest dolomite for this calculation because they are closest to the inferred source of Type 2 dolomitizing fluid, and the most likely to have fully equilibrated with Type 2 fluid during its ascent through the formation. Temperatures of 90ºC are based on analyses of apatite fission track data, representing the maximum temperatures experienced in the deep center of the Williston Basin in the Paleozoic (Osadetz et al., 2002). For reference, a higher temperature of 150ºC gives a lower fluid δ^{26}Mg value of –1.1‰. Type 2 fluids (–0.8‰) are inferred to be much lower in δ^{26}Mg value than Middle Devonian seawater (+0.15‰), demonstrating that there is plenty of scope for creating the observed gradient in δ^{26}Mg values in Lower Member Winnipegosis dolomite.

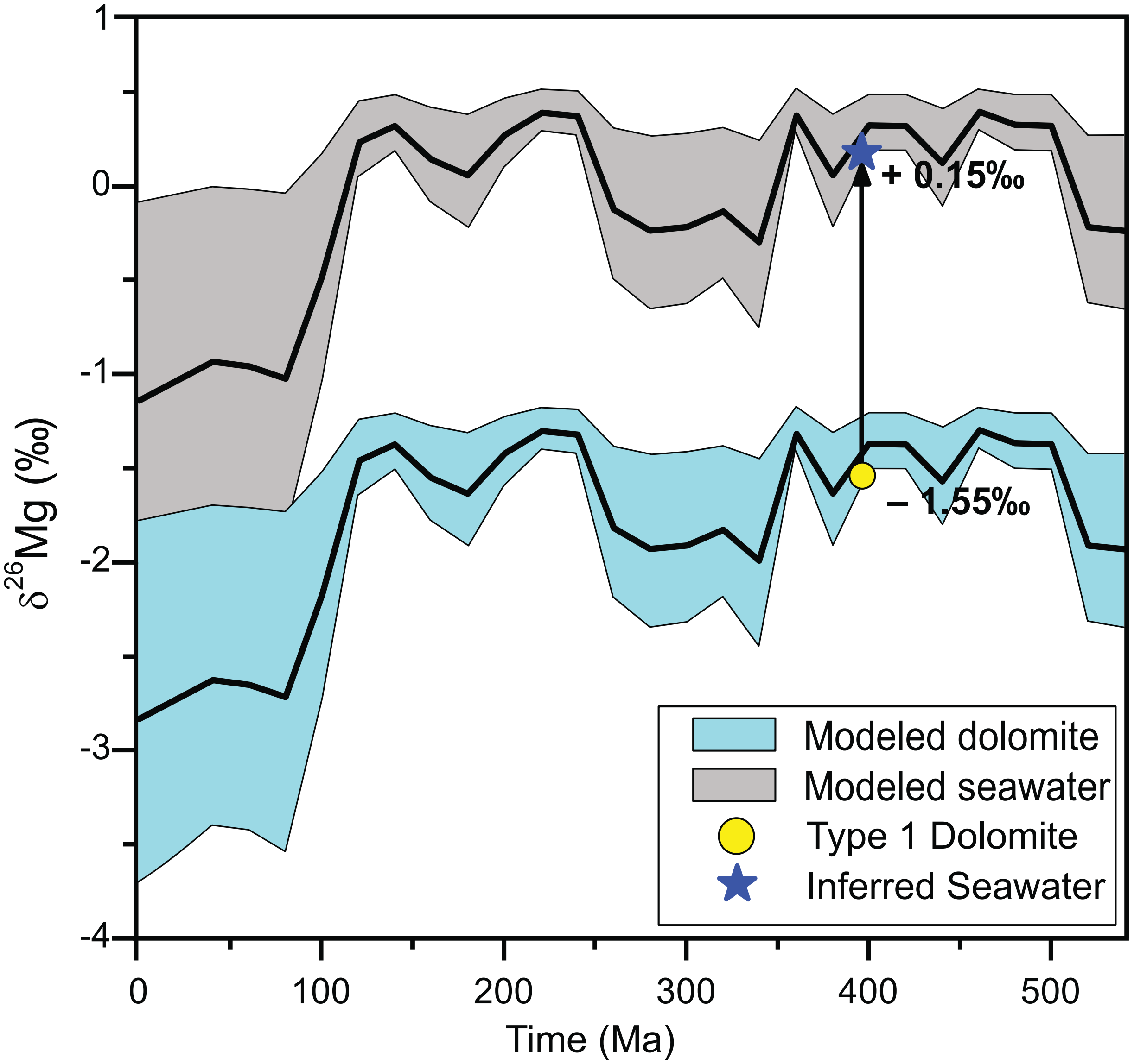

Figure 5.2 Secular change in the δ^{26}Mg of seawater based modified after Li et al. (2015). The curve is based on a box model of the ocean Mg cycle and estimates of seawater Mg/Ca ratio from Wilkinson and Algeo (1989) and Hardie (1996). The model assumes a constant Mg isotope fractionation factor between dolomite and aqueous solution; Δ^{26}Mg ≈ –1.7‰. The δ^{26}Mg value for Type 1 dolomite plot within the modeled sedimentary dolomites range.

Model runs simulating re-equilibration of Type 1 proto-dolomite (containing 35% mol% Mg) with a hot Type 2 Mg-bearing fluid are shown in Figure 5.3. In this model, the reaction front region (defined as the migrating peak in δ^{26}Mg values) results from a combination of Rayleigh fractionation effects and mixing between two isotopically distant Mg sources, Type 1 dolomite (–1.55‰) and Type 2 dolomitizing fluids (–0.80‰). Behind the reaction front, Type 1 proto-dolomite is transformed to stoichiometric Type 2 dolomite. Ahead of the reaction front, Type 1 proto-dolomite remains unaffected. As the reaction front migrates in the direction of fluid flow, a broad gradient in δ^{26}Mg develops behind the reaction front (Figure 5.3c). The gradient reflects progress made towards equilibration of the original Type 1 proto-dolomite with the isotopically lighter Type 2 fluid, with reaction progress decreasing with increasing distance from the source of Mg and fluid in the center of the Williston basin. The result is a gradient in dolomite δ^{26}Mg values where Rayleigh fractionation effects are subordinate to the mixing effects (Figure 5.3d), generating an up-flow gradient of increasing δ^{26}Mg values that is larger than what can be produced from Rayleigh fractionation effects alone (Figure 5.1d). Moreover, the gradient in δ^{26}Mg values is independent of dolomite concentration, which also fits the observations.

Banner et al. (1988) proposed a similar model for the origin of the Burlington-Keokuk dolomite, based on reaction path modeling of trace element concentrations (Sr) and δ^{18}O and ^{87}Sr/^{86}Sr. As dolomite is relatively low in Sr concentration, and oxygen is similarly concentrated between water and carbonate rock, the δ^{18}O value and ^{87}Sr/^{86}Sr ratio of proto-dolomite can be altered at relatively low water-rock ratios (Fig 1.1). However, this would not be the case for Mg isotopes in dolomite or proto-dolomite, which would require a large stable supply of reactive Mg and high cumulative water-rock ratios before it too could be altered. Accordingly, a better appreciation of the scale of the fluid flow system that altered δ^{18}O and ^{87}Sr/^{86}Sr could be gleaned from an investigation of dolomite δ^{26}Mg values in the same samples.

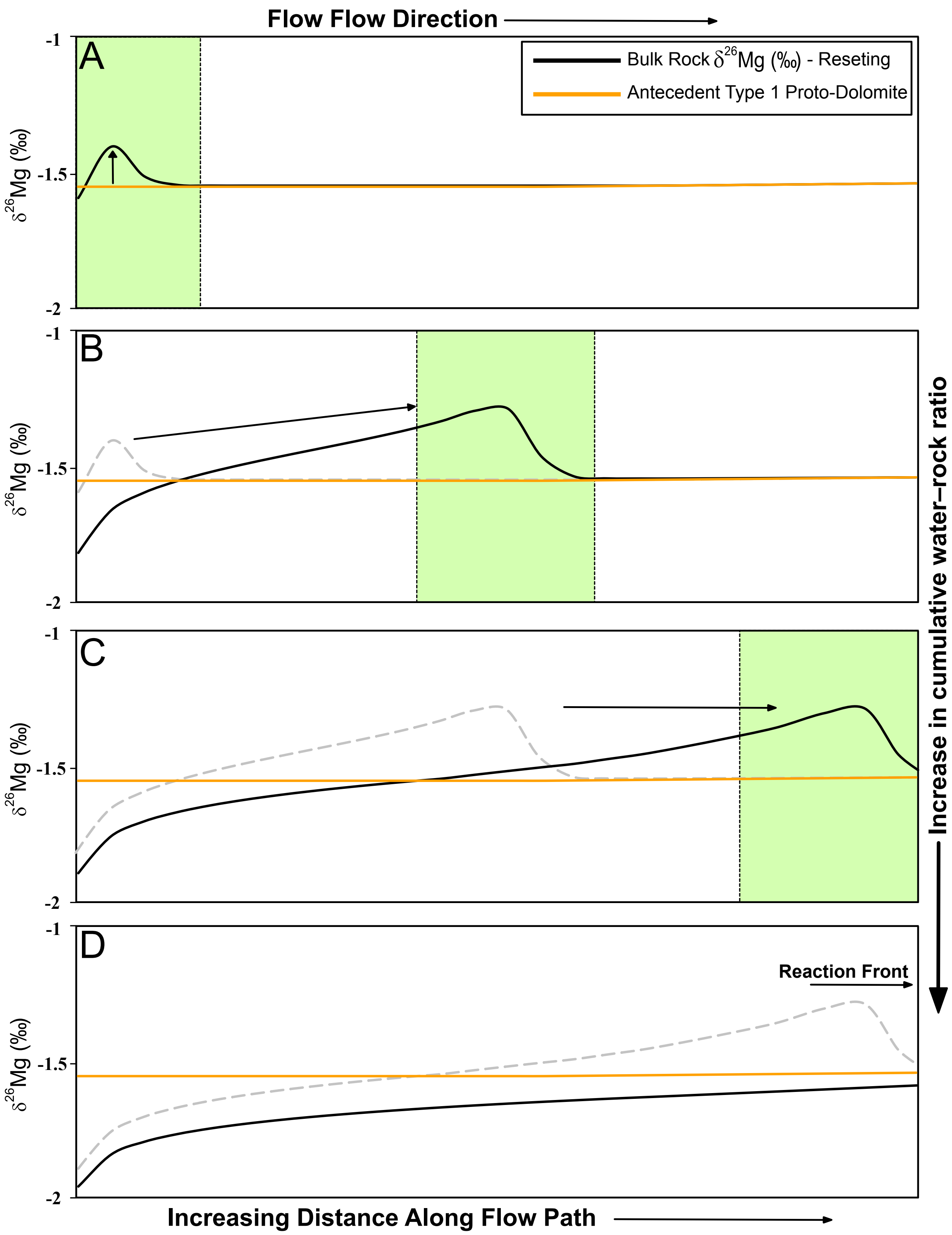Flow Flow Direction
A
B
C
D
Bulk Rock δ^{26}Mg (‰) - Reseting
Antecedent Type 1 Proto-Dolomite
δ^{26}Mg (‰)
-1
-1.5
-2
Increase in cumulative water–rock ratio
Reaction Front
Increasing Distance Along Flow Path

Figure 5.3 Water-rock interaction model (modified after Ahm et al., 2018) simulating progressive alteration of Type 1 proto-dolomite (δ^{26}Mg value of –1.55‰) by a Type 2 (–0.80‰) dolomitizing fluid. Panels A through D represents an increase in cumulative water-rock ratio. Results show the presence of a reaction front, highlighted by the green box, that moves through the rock in the direction of fluid flow. By panel D, the reaction front has migrated past the modeled flow path length shown. Behind the reaction front, Type 1 proto-dolomite is progressively transformed to Type 2 dolomite, producing a gradient of increasing δ^{26}Mg values in the direction of fluid flow, reflecting the fact that proto-dolomite located closer to the source of the dolomitizing fluid in the deep center of the Williston basin is exposed to higher cumulative water-rock volumes during ascending flow than proto-dolomite located near the edges of the basin (A-D). This gradient will eventually be removed if the fluid flow event continues long enough to equilibrate the entire dolomite body with the new higher temperature Mg-bearing fluid. Gray dotted line represents the echo of the previous bulk rock δ^{26}Mg value.

5.3.5 Source of Mg-bearing fluids

Because high water-rock ratios are needed to substantially alter the Mg isotope composition of previously formed proto-dolomite, steady supplies of reactive Mg are required to meet the demand. The inventory of Mg in pore fluids would be quickly exhausted by reactive fluid flow. As a case in point, the Lower Member Winnipegosis dolomite contains ~ $10\times^{17}$ moles of Mg. The pore fluids are estimated to contain less than 5% of this amount. This calculation is based on a primary porosity of 35%, with a Mg concentration (Mg ≈ 1500 – 2000 mmol/Kg H_2O; Fu et al., 2006) based on inclusion brines measured from the Whitkow halite, likely to reflect evaporatively concentrated seawater brines in the Elk Point Sea during the Middle Devonian. If the fluids ascended from the deep center of the basin as proposed, then a source of Mg in the underlying crystalline basement is implied.

Ultramafic rocks contain high concentrations of Mg with a uniform δ^{26}Mg value of –0.25‰ ± 0.04‰ (2σ) (Teng et al. 2010). Similar δ^{26}Mg values characterize biotite (–0.29‰ to –0.12‰) and amphibole (–0.32‰ to –0.14‰) in granites (Liu et al., 2010; Ryu et al., 2011; Teng, 2017), the high temperatures appearing to greatly limit the range of Mg isotope fractionation that occurs during magmatic processes (Liu et al., 2010). This leaves high temperature weathering by crustal fluids as a potential mechanism by which fractionated Mg isotopes might form in the crust, as inferred by the much wider range and generally more negative values of δ^{26}Mg in chlorite (–0.78 to –1.82) (e.g., Kimmig et al., 2018; Ryu et al., 2011)—a hydrothermal alteration product of igneous biotite. These lower δ^{26}Mg values fall in the range of predicted δ^{26}Mg values for the Mg bearing fluid that ascended to form Type 2 dolomite in the Lower Member Winnipegosis in the Williston Basin. Thus, hydrothermal processes involving mafic crustal minerals and ultramafic rocks appears to be a promising way to concentrate and fractionate Mg isotopes in the crust. In addition, carbonation of ultramafic rocks, which results in the production of listwanite (carbonated serpentinite), a rock assemblage consisting of talc, magnesite, quartz and dolomite, needs to be further explored as a source of Mg for dolomitization (Oskierski et al., 2019: Robertson et al., 2019). Below I consider mechanisms by which a hypothetical cache of isotopically light Mg can be delivered upwards into the bottom of the Williston Basin.

5.3.6 Drivers of ascending fluid flow in the Williston Basin

The Mg supply problem is inextricably tied to the forces that can create deep fluid motion in sedimentary basins. However, deep basin fluids are highly saline and will resist forces that can induce flow in more dilute formation waters at shallower depths (Ferguson et al., 2018). As a case in point, there is no evidence from δ^{18}O and δD studies that formation waters in the deep center of the Williston Basin have mixed with meteoric waters with very low δ^{18}O (–19‰) and δD (–150‰) values (Rostron et al., 1998; Iampen and Rostron, 2000; Rostron and Holmden, 2003). Meteoric waters with such low values formed only after uplift of the Western Cordillera in the earliest Cretaceous, which created an orographic effect on isotopes in precipitation in the foreland basin that extended eastward to the Williston Basin (cf. Holmden et al. 1997). However, waters with these isotopically depleted compositions may not have infiltrated the Williston Basin until Tertiary intrusions caused smaller uplifts along the southern edge of the basin about 50 million-years-ago, such as the Black Hills (Iampen and Rostron, 2000; Rostron et al., 1998; Rostron and Holmden, 2003). The fluid flow produced by sediment compaction yields very weak flows (e.g., Bethke, 1985; Whitaker at al., 2004). Thrust sheet loading of the Western Margin of North America during the Cretaceous Laramide Orogeny has been linked to ascending fluid flow in the nearby Alberta Basin (Qing and Mountjoy, 1994), and Pb-Zn mineralization at Pine Point in the Yukon (Rhodes et al., 1984), but these effects did not reach the more southeasterly located intracratonic Williston Basin. Accordingly, the forces that motivated ascending fluid flow in the Williston Basin must have arisen in the crust beneath the basin.

Fu et al. (2006) suggested that Type 2 dolomite formed during a Late Devonian/Early Carboniferous heating event attributed to the far-field effects of the Antler Orogeny on the west coast of North America (Osadetz et al. 2002). A second heating event affected the Williston Basin during the Cretaceous/Tertiary Laramide Orogeny (Osadetz et al. 2002). Both heating events are associated with thermal remnant magnetizations in trace iron oxides in the overlaying Prairie Evaporite, and more deeply buried Red River carbonates of Late Ordovician age (Figure 2.5b) (Chipley and Kyser, 1992; Cioppa et al., 2003; Koehler at al., 1997; Wendte et al. 1998; Al-Aasm et al. 2002; Szabo and Cioppa, 2006). Geothermal heating in the crystalline basement causes fluids to expand, fracturing rocks, and driving fluids upwards through the fractures by seismic pumping (Sibson, 1994). The center of the Williston Basin hosts numerous down-to-the-basement vertical faults (Anderson, 2011; Gerhard et al., 1982, 1988) that may have functioned as conduits for delivering crustal fluids to the basin, and for bypassing low permeability aquitards that would otherwise restrict cross-formational fluid-flow (cf. Kimmig, 2017) (Figure 5.4). Capillary seals might have also played a role in creating over-pressurized fluid compartments in the deep center of the basin. Formed by the adhesive and cohesive forces generated by mixing of water and gas in graded sediments, capillary sealed pressure compartments can reach supra-hydrostatic pressures by the *in situ* formation of natural gas. When the seals rupture, fluids are driven upwards through porous and permeable sedimentary successions (e.g., Bradley and Powley, 1994; Cathles, 2001; Hunt, 1990; Powley, 1990; Shosa and Cathles, 2001). The compartments may conceivably pressurize and rupture many times sending as many fluid pulses upwards in the basin. Three confined carbonate-bearing aquifers would have channelized the bulk of the fluid flow: (1) the

Middle Devonian Winnipegosis aquifer of this study, (2) the Silurian Interlake aquifer, and (3) the Late Ordovician Red River aquifer (Figure 5.4) (Kimmig, 2017).

One of the models for the origin of subsidence in the Williston Basin proposes that a sizeable mafic body transformed to eclogite in the crust below the basin. The increase crustal density caused the lithosphere to sag (Fowler and Nesbit, 1984). Hydrothermal alteration or carbonation of ultramafic rocks associated with this hypothetical mafic body could have also supplied the isotopically light Mg required to create Type 2 dolomite in the Lower Member Winnipegosis.

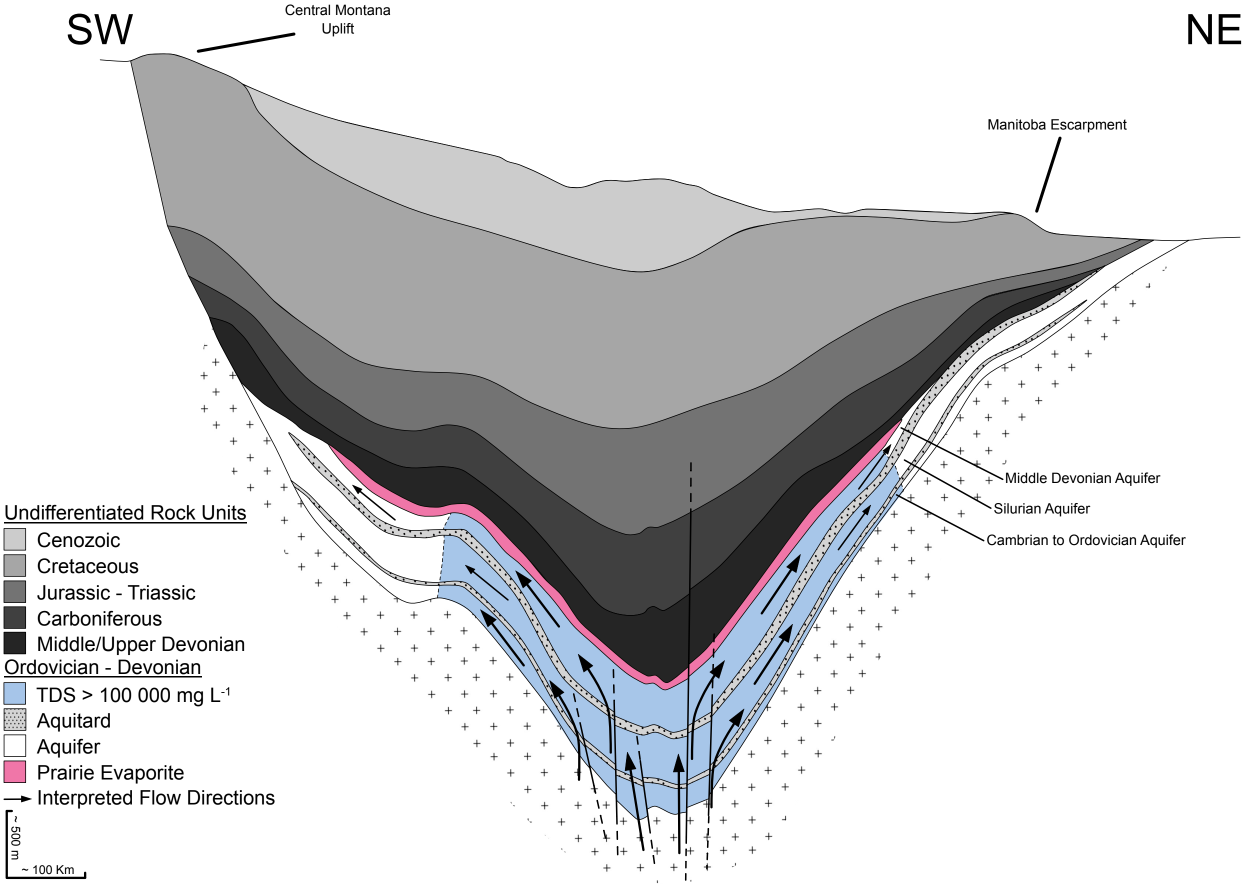

Figure 5.4 Conceptual model of ascending Mg-bearing fluid flow originating from the center of the Williston Basin and below, with up dip directed fluid flow through permeable carbonate aquifers. Three confined carbonate-bearing aquifers would have channelized the bulk of the fluid

flow: (1) the Middle Devonian Winnipegosis aquifer of this study, (2) the Silurian Interlake aquifer, and (3) the Late Ordovician Red River aquifer (Kimmig, 2017). Only the Interlake dolomites remain to be studied using Mg isotopes. Note that the thickness of the Prairie Evaporite Formation decreases towards the basin margins. Vertical black lines illustrate the down-to-the-basement faults abundantly located near the structural center of the Williston Basin (Anna, 2013). Black arrows denote hypothetical subsurface fluid migration trajectories. TDS = Total Dissolved Solids. The blue color estimates the portion of the deep Williston Basin with TDS concentrations in formation waters of the order of ten times the salinity of seawater (Bachu and Hitchon, 1996; Grasby et al., 2000).

5.3.7 Broader implications of the ascending fluid flow model for dolomite formation in the Williston Basin

Dolomite formation in the Williston Basin is mostly confined to early Paleozoic units below the Prairie Evaporite. This led previous workers to favor a brine reflux model of dolomitization for the Lower Member Winnipegosis. Although Type 1 dolomite preserved in the Upper Member Winnipegosis appears to have formed by seawater or refluxing brines (Kendall, 1985; Fu et al., 2006), the volumetrically larger body of Type 2 dolomite in the Lower Member Winnipegosis formed by ascending fluids that may have been blocked from further ascent by the Prairie Evaporite aquiclude. Dolomite is abundant in the underlying Silurian Interlake Formation, and Kimmig (2017) found a similar pattern of increasing δ^{26}Mg values in the dolomitized burrows of the “C Member” carbonate of the Ordovician Red River Formation. It seems that dolomite formed or altered by ascending fluid flow is common in the strata below the Prairie Evaporite in the Williston Basin, which increases the demand for Mg from a source located in the crust below the deep center of the Williston Basin.

Lately, there has been a surge of interest in the origin of structurally controlled hydrothermal dolomite (Davies and Smith, 2006), and there are aspects of the hydrothermal dolomite model that appear to be applicable to the Williston Basin, even though classic indicators of hydrothermal dolomite are lacking, such as abundant saddle dolomite, coarsely crystalline dolomite, faultassociated dolomite cement, and Mississippi Valley Type ore deposits. On the other hand, wrench faulting and fault-bounded basement highs occur in the crust beneath the Williston Basin, which are features that are associated with structurally controlled hydrothermal dolomite elsewhere. Moreover, Mississippi Valley Type ore deposits are commonly emplaced in shallowly buried strata near the edges of sedimentary basins where they may be later removed by erosion. However, it remains to be determined whether Type 2 dolomite in Lower Winnipegosis (and analogous dolomite in other formations formed during the ascending fluid flow event) formed at a higher temperature than the predicted burial temperature. To some extent, this has already been demonstrated by the identification of two thermal anomalies in the Williston Basin (Osadetz et al., 1998) using fission track dating and basin subsidence models. However, quantitative estimates of temperature could be obtained from clumped isotope paleothermometry and/or fluid inclusion temperature analysis (Bonifacie et al., 2017).

5.3.8 Dolomitization and petroleum migration in the Williston Basin

The contour map of dolomite δ^{26}Mg values is interpreted as a paleofluid flow map and, as such, there is one conspicuous flow path towards the northeast that merits attention from a petroleum migration perspective. This is an area of southwestern Saskatchewan with strong petroleum production in the underlying Red River, and closely overlaps petroleum migration pathways predicted by Khan et al., (2006) using a hydrostatic model of fluid flow in the Red River during source rock maturation (Figure. 4.1b) (Osadetz et al., 1998). The contour map of Red River dolomite δ^{26}Mg shows a similar feature (Kimmig, 2017), indicating that dolomitization by ascending fluid flow in the Late Devonian/Early Carboniferous may have created this pathway of enhanced permeability in the Red River aquifer that was later used by migrating petroleum systems. Peak maturation of early Paleozoic source rocks occurred 65-70 Ma ago (Osadetz et al., 1998). Petroleum may have followed a similar path in the Lower Member Winnipegosis. Traps along this pathway may contain undiscovered petroleum reservoirs.

5.4 Interpretation of the $^{87}Sr/^{86}Sr$ map for the Lower Member Winnipegosis dolomite

Fu et al. (2006) also considered Type 2 dolomite to have formed by ascending fluid flow. Their interpretation was primarily based on the high $^{87}\mathrm{Sr}/^{86}\mathrm{Sr}$ ratios found in Type 2 dolomite compared to Type 1 dolomite in a few Winnipegosis cores from the Saskatoon region. They also noted that present-day formation waters in deeper units of the Williston Basin, such as the Ordovician Red River Formation (avg. 0.70959, n=5), Winnipeg Formation (avg. 0.71502, n=2), and Cambrian Deadwood Formation (avg. 0.71730, n=5) (Kimmig 2017; Rostron and Holmden, 2000) have high $^{87}\mathrm{Sr}/^{86}\mathrm{Sr}$ ratios. However, if the deep center of the basin was the source of radiogenic $^{87}\mathrm{Sr}$, then the Lower Member Winnipegosis dolomites should record decreasing $^{87}\mathrm{Sr}/^{86}\mathrm{Sr}$ ratios in the direction of fluid flow. However, the $^{87}\mathrm{Sr}/^{86}\mathrm{Sr}$ map does not meet this expectation (Figure 4.3a), most likely because the cores sampled near the center of the basin are only partially dolomitized and need to be corrected Sr contributions from the limestone, which is assumed to have a Middle Devonian seawater signature of 0.70789. Two-component mixing between dolomite and calcite in these cores can be observed on a $^{87}\mathrm{Sr}/^{86}\mathrm{Sr}$ *vs.* Ca/Sr diagram where mixtures plot as straight lines according to Eq. 5.1.

$$\left(\frac{^{87}\mathrm{Sr}}{^{86}\mathrm{Sr}}\right)_{\mathrm{mixure}} = \left(\frac{^{87}\mathrm{Sr}}{^{86}\mathrm{Sr}}\right)_{\mathrm{dolomite}} \times \left(\frac{\left(\frac{\mathrm{Ca}}{\mathrm{Sr}}\right)_{\mathrm{mixure}} - \left(\frac{\mathrm{Ca}}{\mathrm{Sr}}\right)_{\mathrm{calcite}}}{\left(\frac{\mathrm{Ca}}{\mathrm{Sr}}\right)_{\mathrm{dolomite}} - \left(\frac{\mathrm{Ca}}{\mathrm{Sr}}\right)_{\mathrm{calcite}}}\right) + \left(\frac{^{87}\mathrm{Sr}}{^{86}\mathrm{Sr}}\right)_{\mathrm{calcite}} \times \left(1 - \frac{\left(\frac{\mathrm{Ca}}{\mathrm{Sr}}\right)_{\mathrm{mixure}} - \left(\frac{\mathrm{Ca}}{\mathrm{Sr}}\right)_{\mathrm{calcite}}}{\left(\frac{\mathrm{Ca}}{\mathrm{Sr}}\right)_{\mathrm{dolomite}} - \left(\frac{\mathrm{Ca}}{\mathrm{Sr}}\right)_{\mathrm{calcite}}}\right) \tag{5.1}$$

All input parameters are known except for the Ca/Sr ratios in dolomite and calcite, which may be found using a cross-plot of Sr/Ca *vs.* Mg/Ca. Dolomite Sr/Ca can be calculated from the best-fit equation of the line for a Mg/Ca ratio of 1.0, while the calcite end-member may be approximated from the y-intercept (Mg/Ca = 0). Dolomite end-member $^{87}\mathrm{Sr}/^{86}\mathrm{S}$ ratios determined in this way are listed in Table 4.2. With these data, a new contour map of dolomite $^{87}\mathrm{Sr}/^{86}\mathrm{Sr}$ ratios for the Lower Member Winnipegosis was constructed in Figure 4.3b. The new map shows high dolomite $^{87}\mathrm{Sr}/^{86}\mathrm{Sr}$ ratios in the center of the Williston Basin, becoming progressively lower towards the basin margins. The new map supports the ascending fluid flow model of dolomitization, but the higher than ideal slope uncertainty affecting the determination of the Ca/Sr end-member dolomite and calcite determinations warrants caution. This can be remedied in future work by analysis of additional samples with aim of improving the determinations of the slopes and intercepts of the mixing lines.

5.5 Interpretation of the δ^{18}O *map for the Lower Member Winnipegosis dolomite*

The average δ^{18}O value from the Lower Member Winnipegosis dolomite is –6.23‰ (Table 4.1), which is lower than the estimated range of dolomites believed to have formed during early diagenesis at shallow burial depths (–1 to –4‰; Fritz, 1971; Veizer et al., 1999). The contour map (Appendix A – Supplementary Figure 1) of dolomite δ^{18}O values for the Lower Member Winnipegosis does not follow the depositional outline of the Elk Point Basin or the isopach map of depth of the Williston Basin. The pattern appears to be random. This perhaps not too surprising. Ideally, δ^{18}O values of dolomite should reflect the δ^{18}O value of the dolomitizing fluids offset by a temperature-dependent fractionation factor. However, δ^{18}O values in dolomite are easily altered by water-rock interaction at low water-rock ratios (~$10e^0$ - $10e^1$) (Figure 1.1) (Ahm et al., 2018; Banner and Hanson, 1990; Husson et al., 2015).

CHAPTER 6 – Conclusion

Results from this study show significant geographic variation in isotope signatures ($\delta^{13}C_{Carb}$, $\delta^{18}O$, $^{87}Sr/^{86}Sr$ and $\delta^{26}Mg$) and trace metal concentrations (Fe and Mn) in the Lower Member Winnipegosis in the Williston Basin. The sensitivity of each of these elements in carbonate sediments to diagenetic alteration varies depending on numerous factors (Figure 1.1), and the relative differences in the response of different element systems to water-rock interactions translate into characteristic trends that can be used to distinguish the source(s), paleo-fluid flow directions, and hydrogeological model of dolomitization. The geographic variation in $\delta^{13}C_{Carb}$ values (Figure 4.4a) is interpreted as being inherited from the precursor carbonate (Ahm et al., 2018; Banner and Hanson, 1990; Fu et al., 2006). The high carbonate $\delta^{13}C$ values in the central basin / mud mound facies is interpreted to reflect CO_2 degassing of hypersaline waters (Figure 4.4a). Although the high Fe and Mn concentrations of the studied dolomites is typical of burial dolomite (Tucker and Wright, 1990; Warren, 2000), maps of Fe and Mn concentrations (Figures 4.3b and 4.3c) resemblance the $\delta^{13}C_{carb}$ map (Figures 4.3a and 4.3d). This is evidence that the Fe and Mn concentrations were inherited from the original carbonate.

Dolomite in the Lower Member Winnipegosis records a basin-wide gradient in $\delta^{26}Mg$ values ranging from −2.03‰ in the deep center of the basin in North Dakota to −1.33‰ along the outcrop edge of the basin in Manitoba (Figure 4.1a) (Table 4.2). The dolomites are enriched in radiogenic ^{87}Sr consistent with their formation in a burial environment. I hypothesize that fluid overpressures created in the crust beneath the center of the Williston Basin during the Late Devonian/Early Carboniferous heat flow anomaly, caused Mg-bearing fluids to flow into the bottom of the Williston Basin using down-to-the-basement faults as conduits, pressurizing carbonate units like the Winnipegosis, and inducing upwardly directed flow along the confined sedimentary beds. A $\delta^{26}Mg$ gradient of similar magnitude characterizes dolomitic burrows of the Late Ordovician Red River Formation (Kimmig, 2017), indicating that dolomitization by ascending fluid flow is not restricted to the Middle Devonian Winnipegosis. The younger Mg bearing fluids that created the gradient were isotopically lighter (~ –0.8‰) than Middle Devonian seawater (0.15‰). My preferred interpretation for the origin of the gradient is the equilibration of the original Type 1 proto-dolomite (–1.55‰) with an isotopically lighter Mg-bearing Type 2 fluid as it ascended through the formation from a source of fluid overpressure in the deep center of the basin (Figure 5.4). Water-rock interaction modeling (Figure 5.3) demonstrates how gradients in dolomite δ^{26}Mg values might form. In the preferred model, Rayleigh fractionation effects are subordinate to the cryptic mixing effects. Type 2 dolomite formed the center of the basin experienced higher water-rock ratios and, thus, shifted to lower δ^{26}Mg values, than Type 2 dolomite near the edges of the basin which experienced lower water-rock ratios.

The ascending fluid flow model predicts that the gradients in dolomite δ^{26}Mg values will be restricted to carbonate units deposited below the Prairie Evaporite aquiclude. Deep crustal fluids carry heavy loads of dissolved salt that would have protected the evaporite aquiclude from dissolution during ascending fluid flow, but it may be wondered where these fluids ended up. Today there are saline springs along the Manitoba Escarpment (Grasby et al., 2006) that prompt me to consider the possibility that ascending fluids were flushed from the basin along its edges. However, the depositional edge of the basin has been eroded by time and repeated assault by ice sheet advances during the Pleistocene.

The evidence presented here for ascending fluid flow, and potential involvement of crustal fluids, would appear to make the Willison Basin a strong candidate for Mississippi Valley Type ore deposition, though none have been found except for a small 15 cm showing of sulfide-bearing dolomite in a core near the basin edge in Manitoba with 4.59 wt% Zn and 0.41 wt% Pb (Bamburak and Kline, 2004), strengthening the possibility that Pb-Zn ores have been eroded from the edge of the basin, and consistent with Jackson and Beales (1967), who wrote that one of the most striking features of Mississippi Valley Type orebodies is that the mineralization usually occurs near the margins of sedimentary basins, or arches between basins (Anderson and Macqueen, 1982).

Fluid flow is a major condition of replacive dolomitization, and all models of dolomitization have a hydrogeological component (Machel, 2004). This study demonstrates the potential for Mg isotopic mapping of paleofluid flow using dolomite bodies in sedimentary basins, with implications for tracing petroleum migration fairways and pinpointing petroleum reservoirs. Moreover, this model presents a scenario that would seem to be universally relevant to sedimentary basins worldwide, as it allows proto-dolomite to form early from Mg-bearing seawater fluids at low temperatures, and later recrystallize during burial in the presence of Mg-bearing formation waters at higher temperatures. This study cautions that secular histories of seawater δ^{26}Mg initially preserved in dolomite may be overprinted by their burial histories.

6.1 Future directions

The ascending fluid that dolomitized the Lower Member Winnipegosis in the Williston Basin must have dolomitized other carbonate units as well. Indeed, similar patterns in basin-scale gradients in δ^{26}Mg values and ^{87}Sr/^{86}Sr ratios were found in a study of Late Ordovician Red River dolomite in the Williston Basin (Kimmig, 2017). Only the pervasively dolomitized Silurian Interlake Formation remains to be studied, and it seems likely that it too will record the same Mg isotopic patterns as the underlying Red River (Kimmig, 2017) and overlying Winnipegosis (this study). This prediction needs to be verified. A simple budget calculation reveals that the amount of Mg that could be reasonably imagined to be contained in pore spaces in sedimentary units located below the Prairie Evaporite is not enough to explain the volume of dolomite found even in the Lower Member Winnipegosis. It seems inevitable that a significant fraction of the Mg in dolomite in the Williston Basin must come from the underlying crust or mantle. Future work needs to examine potential Mg isotope effects associated with hydrothermal alteration of ultramafic rocks, particularly the hydrothermal dolomite associated with listwanite, which forms during hydrothermal alteration of peridotite (Robertson et al., 2019).

The lithosphere is weak below the Williston Basin, which accounts for the long history of subsidence in this region over Phanerozoic time. Oil field brines collected from the basal Cambrian Deadwood aquifer have high ^{87}Sr/^{86}Sr ratios (0.71730, n=5; Kimmig 2017; Rostron and Holmden 2000). At present, this is the only empirical evidence that crustal fluids may have entered, or currently reside, in the Williston Basin, but it is not unique evidence, as the high ^{87}Sr/^{86}Sr ratios could have resulted from local-scale water-rock interactions with siliciclastic units in the deep basin, such as those in the Ordovician Winnipeg Formation. Other tracers are needed that can show a clear connection between Type 2 dolomite in the Lower Winnipegosis and a mantle source of Mg. Of course, the Mg isotopes, themselves, lend crucial information regarding Mg demand through mass balance considerations, but it ought to be possible to find additional tracers that can identify the crust or mantle, ultramafic bodies in the crust, as source the source of ascending fluids and accompanying Mg. Perhaps rare earth elements could be useful, as ultramafic rocks have higher Sm/Nd ratios than the continental crust or its weathered products.

Clumped isotope analysis should be explored to determine temperatures of dolomite formed by ascending fluid flow in the Williston Basin. This information is needed to determine whether the micritic dolomite formed or altered in the Williston Basin is belongs to, or is a variant of, the structurally controlled hydrothermal dolomite facies.

Radiometric dating of dolomite should be explored. The most promising dating method is U-Pb isochron dating. Dating could be used to test whether Type 1 and Type 2 dolomite are genuinely different in age, and a product of different hydrogeological mechanisms of dolomitization. Dating could also test the hypothesis that Type 2 dolomite formed during the Late Devonian/Early Carboniferous heat flow anomaly, as proposed in this thesis, and in an earlier study by Fu et al. (2006).

Lastly, I have demonstrated the potential for dolomite bodies to preserve Mg isotopic information on paleofluid flow in sedimentary basins. As the Williston Basin has been extensively cored, and these cores are housed in facilities in Saskatchewan, Manitoba, North Dakota, and Montana, it may be possible to create 3-D maps of paleofluid flow in the Williston Basin with additional sampling and isotopic analyses. These maps could reveal highly detailed information on migration pathways taken by ore fluids and petroleum fluids in the geological past, which could help locate missing MVT deposits and new petroleum reservoirs in the Williston Basin.

LIST OF REFERENCES

Ahm, A. S. C., Bjerrum, C. J., Blättler, C. L., Swart, P. K., & Higgins, J. A. (2018). Quantifying early marine diagenesis in shallow-water carbonate sediments. *Geochimica et Cosmochimica Acta*, *236*, 140-159.

Al-Aasm, I. S., Lonnee, J., & Clarke, J. (2002). Multiple fluid flow events and the formation of saddle dolomite: case studies from the Middle Devonian of the Western Canada Sedimentary Basin. *Marine and Petroleum Geology*, *19*(3), 209-217.

Anderson, F. J. (2011) Structural relationships between surface lineaments and basement faulting in the northeastern Williston Basin. In *The Bakken–Three Forks Petroleum System in the Williston Basin* (Eds. Robinson, J.W., LeFever, J. A., & Gaswirth S. B.), *Rocky Mountain Association of Geologists,* 376–392.

Anderson, G. M., & Macqueen, R. W. (1982). Ore deposit models-6. Mississippi Valley-type lead-zinc deposits. *Geoscience Canada*, *9*(2).

Anna, L. O. (2013) Geologic assessment of undiscovered oil and gas in the Williston Basin Province, Montana, North Dakota, and South Dakota. In *Assessment of Undiscovered Oil and Gas Resources of the Williston Basin Province of North Dakota, Montana, and South Dakota* (Eds. U.S. Geological Survey Williston Basin Province Assessment Team), *U.S. Geological Survey Digital Data Series* 69-71.

Bachu, S., & Hitchon, B. (1996). Regional-scale flow of formation waters in the Williston Basin. *AAPG bulletin*, *80*(2), 248-264.

Baillie, A. D. (1951). Devonian Geology of Lake Manitoba-Lake Winnipegosis Area. Province of Manitoba, *Department of Mines and Natural Resources, Mines Branch*. Publication No. 49-2.

Baillie, A.D. (1953). Devonian System of the Williston Basin area, Winnipeg, Manitoba. Province of Manitoba, *Department of Mines and Natural Resources, Mines Branch*. Publication No. 52-5.

Baker, P. A., Gieskes, J. M., & Elderfield, H. (1982). Diagenesis of carbonates in deep-sea sediments; evidence from Sr/Ca ratios and interstitial dissolved Sr^{2+} data. *Journal of Sedimentary Research*, *52*(1), 71-82.

Bamburak, J. D., & Klyne, K. (2004). A possible new Mississippi Valley-type mineral occurrence near Pemmican Island in the north basin of Lake Winnipegosis, Manitoba (NTS 63B12 and 13, 63C9 and 16). *Report of Activities*, 266-278.

Banner, J. L., Hanson, G. N., & Meyers, W. J. (1988). Rare earth element and Nd isotopic variations in regionally extensive dolomites from the Burlington-Keokuk Formation (Mississippian); implications for REE mobility during carbonate diagenesis. *Journal of Sedimentary Research*, *58*(3), 415-432.

Banner, J. L., & Hanson, G. N. (1990). Calculation of simultaneous isotopic and trace element variations during water-rock interaction with applications to carbonate diagenesis. *Geochimica et Cosmochimica Acta*, *54*(11), 3123-3137.

Bathurst, R. G. (1972). *Carbonate sediments and their diagenesis* (Vol. 12). Elsevier.

Berner, E. K., & Berner, R. A. (1996). Global environment water, air, and geochemical cycles Prentice-Hall. *Englewood Cliffs, NewJersey*.

Bethke, C. M. (1985). A numerical model of compaction-driven groundwater flow and heat transfer and its application to the paleohydrology of intracratonic sedimentary basins. *Journal of Geophysical Research: Solid Earth*, *90*(B8), 6817-6828.

Bialik, O. M., Wang, X., Zhao, S., Waldmann, N. D., Frank, R., & Li, W. (2018). Mg isotope response to dolomitization in hinterland-attached carbonate platforms: Outlook of δ^{26}Mg as a tracer of basin restriction and seawater Mg/Ca ratio. *Geochimica et Cosmochimica Acta*, *235*, 189-207.

Blättler, C. L., Miller, N. R., & Higgins, J. A. (2015). Mg and Ca isotope signatures of authigenic dolomite in siliceous deep-sea sediments. *Earth and Planetary Science Letters*, *419*, 32-42.

Bonifacie, M., Calmels, D., Eiler, J. M., Horita, J., Chaduteau, C., Vasconcelos, C., Agrinier, P., Katz, A., Passey, B., Ferry, B. H., & Bourrand, J. J. (2017). Calibration of the dolomite clumped isotope thermometer from 25 to 350°C, and implications for a universal calibration for all (Ca, Mg, Fe) CO_3 carbonates. *Geochimica et Cosmochimica Acta*, *200*, 255-279.

Bradley J. S and Powley D. E. (1994). Pressure compartments in sedimentary basins: a review. In *Basin Compartments and Seals*. (Ed. P. J. Ortoleva*) AAPG Memoirs,* 61, 3-26.

Catanzaro, E. J., Murphy, T. J., Garner, E. L., & Shields, W. R. (1966). Absolute isotopic abundance ratios and atomic weight of magnesium. *Journal of Research of the National Bureau of Standards*, 70, 453-458.

Cathles, L. M. (2001). Capillary seals as a cause of pressure compartmentation in sedimentary basins. In *Petroleum Systems of Deep-Water Basins: Global and Gulf of Mexico Experience.* Proceedings of the Gulf Coast Section Society of Economic Paleontologists and Mineralogists Foundation, 21st Annual Bob F. Perkins Research Conference, 561-572.

Carlson, C. G., & Thompson, S. C. (1987). Stratigraphy of the deadwood formation and winnipeg group in the Williston Basin.

Chai, L., Navrotsky, A., & Reeder, R. J. (1995). Energetics of calcium-rich dolomite. *Geochimica et Cosmochimica Acta*, *59*(5), 939-944.

Chang, V. T. C., Makishima, A., Belshaw, N. S., & O'Nions, R. K. (2003). Purification of Mg from low-Mg biogenic carbonates for isotope ratio determination using multiple collector ICP-MS. *Journal of Analytical Atomic Spectrometry*, *18*(4), 296-301.

Chipley, D., & Kyser, T. K. (1992). Preservation of ancient basinal fluids in halite fluid inclusions. In *Proceedings of the 7th International Symposium on Water/Rock Interaction* (Eds. J. Kharaka & Maest, A. S.) International Association of Geochemistry and Cosmochemistry and Alberta Research Council, Sub-Group on Water-Rock Interaction, Edmonton, AB, Canada, 1105-1108.

Cioppa, M. T. (2003). Magnetic evidence for the nature and timing of fluid migration in the Watrous Formation, Williston Basin, Canada: A preliminary study. *Journal of Geochemical Exploration*, *78*, 349-354.

Clark, I. D., & Fontes, J. C. (1990). Paleoclimatic reconstruction in northern Oman based on carbonates from hyperalkaline groundwaters. *Quaternary Research*, *33*(3), 320-336.

Davies, G. R., & Smith Jr, L. B. (2006). Structurally controlled hydrothermal dolomite reservoir facies: An overview. *AAPG bulletin*, *90*(11), 1641-1690.

de Dolomieu (1791) D. Sur un genre de Pierres calcaires trés-peu effervescentes avec les acides, & phosphorescentes par la collision. J. de Physique 39, 3–10. See also English translation of Dolomieu's paper with notes reporting his discovery of dolomite by Carozzi, A. V., & Zenger, D. H. (1981) *Journal of Geoscience Education*. 29, 4-10.

De Vleeschouwer, D., Leather, D., & Claeys, P. (2015). Ripple marks indicate Mid-Devonian paleo-wind directions in the Orcadian Basin (Orkney Isles, Scotland). *Palaeogeography, palaeoclimatology, palaeoecology*, *426*, 68-74.

Degens, E. T., & Epstein, S. (1964). Oxygen and carbon isotope ratios in coexisting calcites and dolomites from recent and ancient sediments. *Geochimica et Cosmochimica Acta*, *28*(1), 23-44.

Dessert, C., Galy, A., & Elderfield, H. (2005). Mechanisms of Mg isotopes fractionation during CaCO3 biomineralization. *Geochimica et Cosmochimica Acta Supplement*, *69*, A214.

Drits, V. A., McCarty, D. K., Sakharov, B., & Milliken, K. L. (2005). New insight into structural and compositional variability in some ancient excess-Ca dolomite. *The Canadian Mineralogist*, *43*(4), 1255-1290.

Duce, R. A., & Tindale, N. W. (1991). Atmospheric transport of iron and its deposition in the ocean. *Limnology and Oceanography*, *36*(8), 1715-1726.

Dunnington, H. V. (1967). Aspects of diagenesis and shape change in stylolitic limestone reservoirs. In *7th World Petroleum Congress*. World Petroleum Congress.

Ehrets, J. R., & Kissling, D. L. (1987). Winnipegosis platform margin and pinnacle reef reservoirs, northwestern North Dakota. *Williston Basin Symposium.*

Elderfield, H. (1986). Strontium isotope stratigraphy. *Palaeogeography, palaeoclimatology, palaeoecology*, *57*(1), 71-90.

Elrod, V. A., Berelson, W. M., Coale, K. H., & Johnson, K. S. (2004). The flux of iron from continental shelf sediments: A missing source for global budgets. *Geophysical Research Letters*, *31*(12).

Emrich, K., Ehhalt, D. H., & Vogel, J. C. (1970). Carbon isotope fractionation during the precipitation of calcium carbonate. *Earth and Planetary Science Letters*, *8*(5), 363-371.

Fabricius, I. L. (2000). Interpretation of burial history and rebound from loading experiments and occurrence of microstylolites in mixed sediments of Caribbean Sites 999 and 1001. In *Proceedings of the Ocean Drilling Program, scientific results*, 165, 177-190.

Fantle, M. S., & Higgins, J. (2014). The effects of diagenesis and dolomitization on Ca and Mg isotopes in marine platform carbonates: implications for the geochemical cycles of Ca and Mg. *Geochimica et Cosmochimica Acta*, *142*, 458-481.

Feinstein S., Kohn B., Osadetz K., Everitt R., and O'Sullivan P. (2009) Variable Phanerozoic thermal history in the Southern Canadian Shield: evidence from an apatite fission track profile at the Underground Research Laboratory (URL), Manitoba. *Tectonophysics* 475, 190-199.

Faure, G., & Powell, J. L. (1972). *Strontium isotope geology* (Vol. 1). Springer Science & Business Media.

Ferguson, G., McIntosh, J. C., Grasby, S. E., Hendry, M. J., Jasechko, S., Lindsay, M. B., & Luijendijk, E. (2018). The persistence of brines in sedimentary basins. *Geophysical Research Letters*, *45*(10), 4851-4858.

Fowler, C. M. R., & Nisbet, E. G. (1984). The subsidence of the Williston Basin. *Canadian Journal of Earth Sciences*, *22*(3), 408-415.

Fu, Q., Qing, H., & Bergman, K. M. (2002). Petrography of diagenetic anhydrite in the Middle Devonian Winnipegosis and Ratner formations, south-central Saskatchewan. *Summary of Investigations*, 2002-4.

Fu, Q., Qing, H., & Bergman, K. M. (2004). Dolomitized calcrete in the Middle Devonian Winnipegosis carbonate mounds, subsurface of south–central Saskatchewan, Canada. *Sedimentary Geology*, *168*(1-2), 49-69.

Fu, Q., Qing, H., & Bergman, K. M. (2006). Dolomitization of the Middle Devonian Winnipegosis carbonates in south-central Saskatchewan, Canada. *Sedimentology*, *53*(4), 825-848.

Fu, Q., & Qing, H. (2011). Medium and coarsely crystalline dolomites in the Middle Devonian Ratner Formation, southern Saskatchewan, Canada: origin and pore evolution. *Carbonates and Evaporites*, *26*(2), 111-125.

Fung, I. Y., Meyn, S. K., Tegen, I., Doney, S. C., John, J. G., & Bishop, J. K. (2000). Iron supply and demand in the upper ocean. *Global Biogeochemical Cycles*, *14*(1), 281-295.

Fritz, P. (1971). Geochemical characteristics of dolomites and the18O content of Middle Devonian oceans. *Earth and Planetary Science Letters*, *11*(1-5), 277-282.

Galy, A., Belshaw, N. S., Halicz, L., & O'Nions, R. K. (2001). High-precision measurement of magnesium isotopes by multiple-collector inductively coupled plasma mass spectrometry. *International Journal of Mass Spectrometry*, *208*(1-3), 89-98.

Galy, A., Yoffe, O., Janney, P. E., Williams, R. W., Cloquet, C., Alard, O., Halicz, L., Wadhwa, M., Hutcheon, I., Ramon, E., & Carignan, J. (2003). Magnesium isotope heterogeneity of the isotopic standard SRM980 and new reference materials for magnesium-isotope-ratio measurements. *Journal of Analytical Atomic Spectrometry*, *18*(11), 1352-1356.

Gendzwill, D. J. (1978). Winnipegosis mounds and Prairie Evaporite Formation of Saskatchewan--seismic study. *AAPG Bulletin*, *62*(1), 73-86.

Gendzwill, D. J., & Wilson, N. L. (1987). Form and distribution of Winnipegosis mounds in Saskatchewan. In *Williston Basin: Anatomy of a cratonic oil province* (Eds. Peterson, J. A., Kent, D., Anderson, S. B., Pilatzke, R. H., & Longman, M. W.) *Rocky Mountain Association of Geologists*, 109-117.

Gerhard, L. C., Anderson, S. B., LeFever, J. A., & Carlson, C. G. (1982). Geological development, origin, and energy mineral resources of Williston Basin, North Dakota. *AAPG Bulletin*, *66*(8), 989-1020.

Gerhard, L. C., & Anderson, S. B. (1988) Geology of the Williston Basin (United States portion). In *Geology of North America: Geological Society of America (*Ed. Sloss, L. L.) *Decade of North American Geology*, 221-241.

Gerhard, L.C., Anderson, S.B., and Fischer, D.W. (1990) Petroleum geology of the Williston Basin, In *Interior cratonic basins* (Eds., Leighton, M.W., Kolata, D.R., Oltz, D.F., and Eidel, J.J.) *American Association of Petroleum Geologists Memoir,* 51, 507.

Geske, A., Lokier, S., Dietzel, M., Richter, D.K., Buhl, D., Immenhauser, A. (2015a) Magnesium isotope composition of sabkha porewater and related (sub-) recent stochiometric dolomites, Abu Dhabi (UAE). *Chemical Geology*, 393-394, 112-124.

Geske A, Goldstein, R.H., Macromatis, V., Richter, D.K., Buhl, D.,Kluge, T., John, C.M., Immenhauser, A. (2015b) The Mg isotope (δ^{26}Mg) signature of dolomites. *Geochimica et Cosmochimica Acta* 149, 131-151.

Gingras, M.K., Pemberton, S. G, Muehlenbachs, K., Machel, H. (2004) Conceptual models for burrow-related dolomitization with textural and isotopic evidence from the Tyndall Stone, Canada. *Geobiology*, 2, 21-30.

Goldstein, S. J., & Jacobsen, S. B. (1987). The Nd and Sr isotopic systematics of river-water dissolved material: Implications for the sources of Nd and Sr in seawater. *Chemical Geology: Isotope Geoscience section*, *66*(3-4), 245-272.

Gothmann, A. M., Stolarski, J., Adkins, J. F., & Higgins, J. A. (2017). A Cenozoic record of seawater Mg isotopes in well-preserved fossil corals. *Geology*, *45*(11), 1039-1042.

Grasby, S. E., Bezys, R., & Londry, K. L. (2006). Silica 'chimneys' related to paleo-brine discharge from the Williston Basin. *Journal of Geochemical Exploration*, *89*(1-3), 149-152.

Grasby, S., Osadetz, K., Betcher, R., & Render, F. (2000). Reversal of the regional-scale flow system of the Williston basin in response to Pleistocene glaciation. *Geology*, *28*(7), 635-638.

Hayes, J. M., & Waldbauer, J. R. (2006). The carbon cycle and associated redox processes through time. *Philosophical Transactions of the Royal Society B: Biological Sciences*, *361*(1470), 931-950.

Heckel, P. H., & Witzke, B. J. (1979). Devonian world palaeogeography determined from distribution of carbonates and related lithic palaeoclimatic indicators. *Special Papers in Palaeontology*, *23*, 99-123.

Higgins, J. A., & Schrag, D. P. (2010). Constraining magnesium cycling in marine sediments using magnesium isotopes. *Geochimica et Cosmochimica Acta*, *74*(17), 5039-5053.

Higgins, J. A., & Schrag, D. P. (2015). The Mg isotopic composition of Cenozoic seawater–evidence for a link between Mg-clays, seawater Mg/Ca, and climate. *Earth and Planetary Science Letters*, *416*, 73-81.

Higgins, J. A., Blättler, C. L., Lundstrom, E. A., Santiago-Ramos, D. P., Akhtar, A. A., Ahm, A. C., Bialik, O., Holmden, C., Bradbury, H., Murray, S.t., & Swart, P. K. (2018). Mineralogy, early marine diagenesis, and the chemistry of shallow-water carbonate sediments. *Geochimica et Cosmochimica Acta*, *220*, 512-534.

Hippler, D., Buhl, D., Witbaard, R., Richter, D.K., Immenhauser, A. (2009) Towards a better understanding of magnesium-isotope ratios from marine skeletal carbonates. *Geochimica et Cosmochimica Acta*, 73, 6134-6146.

Holmden C., Creaser R.A. and Muehlenbachs K. (1997) Paleosalinity and paleoenvironment of the Early Cretaceous Ostracode Sea. CSPG Memoir 18, Petroleum Geology of the Cretaceous Manville Group, Western Canada. Edited by, George Pemberton and David Jame p. 77-92.

Holmden, C., Creaser, R. A., Muehlenbachs, K. L. S. A., Leslie, S. A., & Bergstrom, S. M. (1998). Isotopic evidence for geochemical decoupling between ancient epeiric seas and bordering oceans: implications for secular curves. *Geology*, *26*(6), 567-570.

Holmden, C., Panchuk, K., & Finney, S. C. (2012). Tightly coupled records of Ca and C isotope changes during the Hirnantian glaciation event in an epeiric sea setting. *Geochimica et Cosmochimica Acta*, *98*, 94-106.

Hunt, J. M. (1990). Generation and migration of petroleum from abnormally pressured fluid compartments. *AAPG bulletin*, *74*(1), 1-12.

Husson, J. M., Higgins, J. A., Maloof, A. C., & Schoene, B. (2015). Ca and Mg isotope constraints on the origin of Earth's deepest δ13C excursion. *Geochimica et Cosmochimica Acta*, *160*, 243-266.

Immenhauser, A., Holmden, C., & Patterson, W. P. (2008). Interpreting the carbon-isotope record of ancient shallow epeiric seas: lessons from the recent. *Dynamics of epeiric seas*, *48*, 137-174.

Iampen, H. T., & Rostron, B. J. (2000). Hydrogeochemistry of pre-Mississippian brines, Williston Basin, Canada–USA. *Journal of Geochemical Exploration*, *69*, 29-35.

Jackson, S. A., & Beales, F. W. (1967). An aspect of sedimentary basin evolution: the concentration of Mississippi Valley-type ores during late stages of diagenesis. *Bulletin of Canadian Petroleum Geology*, *15*(4), 383-433

Jin, J., & Bergman, K. M. (1999). Sequence stratigraphy of the Middle Devonian Winnipegosis carbonate-prairie evaporite transition, southern Elk Point Basin. *Carbonates and Evaporites*, *14*(1), 64.

Jin, J., & Bergman, K. M. (2001). Revised stratigraphy of the Middle Devonian (Givetian) Winnipegosis carbonate–Prairie Evaporite transition, Elk Point Group, southern Saskatchewan. *Bulletin of Canadian Petroleum Geology*, *49*(4), 441-457.

Jones, L. (1964). The stratigraphy of the Middle Devonian Winnipegosis Formation in Saskatchewan. Williston Basin Symposium.

Jones, B. (2013). Microarchitecture of dolomite crystals as revealed by subtle variations in solubility: implications for dolomitization. *Sedimentary Geology*, *288*, 66-80.

Kaczmarek, S. E., & Thornton, B. P. (2017). The effect of temperature on stoichiometry, cation ordering, and reaction rate in high-temperature dolomitization experiments. *Chemical Geology*, *468*, 32-41.

Hardie, L. A. (1987). Dolomitization; a critical view of some current views. *Journal of Sedimentary Research*, *57*(1), 166-183.

Hardie, L. A. (1996). Secular variation in seawater chemistry: An explanation for the coupled secular variation in the mineralogies of marine limestones and potash evaporites over the past 600 my. *Geology*, *24*(3), 279-283.

Katz, A., Sass, E., Starinsky, A., & Holland, H. D. (1972). Strontium behavior in the aragonite-calcite transformation: An experimental study at 40–98 C. *Geochimica et Cosmochimica Acta*, *36*(4), 481-496.

Karlstrom, K. E., & Timmons, J. M. (2012). Many unconformities make one 'Great Unconformity'. *Grand Canyon Geology; Two Billion Years of Earth's History*, 73-79.

Kendall, A. C. (1975). The Middle Devonian Winnipegosis and lower Prairie Evaporite formations of the commercial potash areas. *Summary Report of Investigations of the Saskatchewan Geological Survey*, 61-65.

Kendall, A. C. (1976). The Ordovician carbonate succession (Bighorn Group) of southeastern Saskatchewan: Mineral Resources, Saskatchewan Geol. Surv. *Sedimentary Geol. Div. Report*, *180*, 1-185.

Kendall, A.C. (1977). Origin of dolomite mottling in Ordovician limestones from Saskatchewan and Manitoba. *Bulletin of Canadian Petroleum Geology*, *25*(3), 480-504.

Kendall, A.C. (1984). Origin and geometry of Red River dolomite reservoirs, western Williston Basin: Discussion. *AAPG Bulletin*, *68*(6), 776-779.

Kendall, A. C. (1989). Brine mixing in the Middle Devonian of western Canada and its possible significance to regional dolomitization. *Sedimentary Geology*, *64*(4), 271-285.

Khan, D. K., Rostron, B. J., Margitai, Z., & Carruthers, D. (2006). Hydrodynamics and petroleum migration in the Upper Ordovician Red River Formation of the Williston Basin. *Journal of Geochemical Exploration*, *89*(1-3), 179-182.

Kimmig, S. R. (2017). *A Study of Novel Magnesium Isotope Tracers in Geological, Paleoceanographic and Biogeochemical Systems* (Doctoral dissertation, University of Saskatchewan).

Kimmig, S. R., & Holmden, C. (2017). Multi-proxy geochemical evidence for primary aragonite precipitation in a tropical-shelf 'calcite sea' during the Hirnantian glaciation. *Geochimica et Cosmochimica Acta*, *206*, 254-272.

Kimmig, S. R., Holmden, C., & Bélanger, N. (2018). Biogeochemical cycling of Mg and its isotopes in a sugar maple forest in Québec. *Geochimica et Cosmochimica Acta*, *230*, 60-82.

Knoll, A. H., Hayes, J. M., Kaufman, A. J., Swett, K., & Lambert, I. B. (1986). Secular variation in carbon isotope ratios from Upper Proterozoic successions of Svalbard and East Greenland. *Nature*, *321*(6073), 832.

Hoefs, J. (2015). Isotope Fractionation Processes of Selected Elements. In *Stable isotope geochemistry* (pp. 35-93). Springer, Cham.

Koehler, G., Kyser, T. K., Enkin, R., & Irving, E. (1997). Paleomagnetic and isotopic evidence for the diagenesis and alteration of evaporites in the Paleozoic Elk Point Basin, Saskatchewan, Canada. *Canadian Journal of Earth Sciences*, *34*(12), 1619-1629.

Horton, T. W., Defliese, W. F., Tripati, A. K., & Oze, C. (2016). Evaporation induced ^{18}O and ^{13}C enrichment in lake systems: A global perspective on hydrologic balance effects. *Quaternary Science Reviews*, *131*, 365-379.

Land L. S. (1980). The isotopic and trace element geochemistry of dolomite: the state of the art. In *Concepts and Models of Dolomitization* (Eds. D. H. Zenger et al.) SEPM Special Publication 28, 87-110.

Land, L. S. (1985). The origin of massive dolomite. *Journal of Geological Education*, *33*(2), 112-125.

Land, L. S. (1998). Failure to Precipitate Dolomite at 25 C from Dilute Solution Despite 1000-Fold Oversaturation after32 Years. *Aquatic Geochemistry*, *4*(3), 361-368.

Lee, T., & Papanastassiou, D. A. (1974). Mg isotopic anomalies in the Allende meteorite and correlation with O and Sr effects. *Geophysical Research Letters*, *1*(6), 225-228.

Li, W., Beard, B. L., Li, C., Xu, H., & Johnson, C. M. (2015). Experimental calibration of Mg isotope fractionation between dolomite and aqueous solution and its geological implications. *Geochimica et Cosmochimica Acta*, *157*, 164-181.

Li, W., Bialik, O. M., Wang, X., Yang, T., Hu, Z., Huang, Q., Zhoa, S., & Waldmann, N. D. (2019). Effects of early diagenesis on Mg isotopes in dolomite: The roles of Mn (IV)-reduction and recrystallization. *Geochimica et Cosmochimica Acta*, *250*, 1-17.

Liu, S. A., Teng, F. Z., He, Y., Ke, S., & Li, S. (2010). Investigation of magnesium isotope fractionation during granite differentiation: implication for Mg isotopic composition of the continental crust. *Earth and Planetary Science Letters*, *297*(3-4), 646-654.

Lippman, F. (1973). Sedimentary carbonate minerals: New York, Springer-Verlag, 228 p.

Lobdell, F. K. (1984). Age and depositional history of the Middle Devonian Ashern Formation in the Williston Basin, Saskatchewan and North Dakota. *Saskatchewan Geological Society Special Publication Number 7: Oil and gas in Saskatchewan, Proceedings of a Symposium,* 5-12.

Lorens, R. B. (1981). Sr, Cd, Mn and Co distribution coefficients in calcite as a function of calcite precipitation rate. *Geochimica et Cosmochimica Acta*, *45*(4), 553-561.

Machel, H. G. (2004). Concepts and models of dolomitization: a critical reappraisal. *Geological Society, London, Special Publications*, *235*(1), 7-63.

Maiklem, W. R. (1971). Evaporative drawdown--a mechanism for water-level lowering and diagenesis in the Elk Point Basin. *Bulletin of Canadian Petroleum Geology*, *19*(2), 485-501.

Martindale, W., Erkmen, U., Metcalfe, D., & Potts, E. (1991). Winnipegosis buildups of the Hitchcock area, southeastern Saskatchewan-a case study. *Sixth International Williston Basin Symposium*, 47-63.

Mavromatis, V., Meister, P., & Oelkers, E. H. (2014). Using stable Mg isotopes to distinguish dolomite formation mechanisms: A case study from the Peru Margin. *Chemical geology*, *385*, 84-91.

Mavromatis, V., Purgstaller, B., Dietzel, M., Buhl,, D., Immenhauser, A., Schott, J. (2017) Impact of amorphous precursor phases on magnesium isotope signatures of Mg-calcite. *Earth and Planetary Science Letters*, 464, 227-236.

Millero, F. J. (1974). The physical chemistry of seawater. *Annual Review of Earth and Planetary Sciences*, *2*(1), 101-150.

Morrow, D. W. (1982). Diagenesis 2. Dolomite-part 2 dolomitization models and Ancient dolostones. *Geoscience Canada*, *9*(2), 95-107.

Morrow, D. W., & Ricketts, B. D. (1988). Experimental investigation of sulfate inhibition of dolomite and its mineral analogues. *The Society of Economic Paleontologists and Mineralogists*, 43.

Mountjoy, E. W., Machel, H. G., Green, D., Duggan, J., & Williams-Jones, A. E. (1999). Devonian matrix dolomites and deep burial carbonate cements: a comparison between the Rimbey-Meadowbrook reef trend and the deep basin of west-central Alberta. *Bulletin of Canadian Petroleum Geology*, *47*(4), 487-509.

Murphy, E. C., Nordeng, S. H., Juenker, B. J., & Hoganson, J. W. (2009). North Dakota stratigraphic column. *ND Geological Survey, Miscellaneous Series*, *91*.

Navrotsky, A., & Capobianco, C. (1987). Enthalpies of formation of dolomite and of magnesian calcites. *American Mineralogist*, *72*(7-8), 782-787.

Nordeng, S. H., & Sibley, D. F. (1994). Dolomite stoichiometry and Ostwald's step rule. *Geochimica et Cosmochimica Acta*, *58*(1), 191-196.

Osadetz, K. G., & Snowdon, L. R. (1995). Significant Paleozoic Petroleum Source Rocks in the Canadian Williston Basin: Their Distribution, Richness and Thermal Maturity (Southeastern Saskatchewan and Southwestern Manitoba) *Geological Survey of Canada.* 60.

Osadetz, K. G., Goodarzi, F., Snowdon, L. R., Brooks, P. W., & Fayerman, S. (1990). Winnipegosis pinnacle reef play in Williston Basin, Saskatchewan and North Dakota: oil compositions and effects of oil-based drilling muds on exploration geochemistry. *Current Research, part D, Geological Survey of Canada, Paper*, 153-163.

Osadetz, K. G., Hannigan, P. K., Stasiuk, L. D., Kohn, B. P., O'Sullivan, P., Feinstein, S., Evetitt, R. A., Gilboy, C. F., & Bezys, R. K. (1998). Williston Basin thermotectonics: variations in heat flow and hydrocarbon generation. *Eighth International Williston Basin Symposium*, 147-165.

Osadetz, K. G., Kohn, B. P., Feinstein, S., & O'Sullivan, P. B. (2002). Thermal history of Canadian Williston basin from apatite fission-track thermochronology — implications for petroleum systems and geodynamic history. *Tectonophysics*, *349*(1-4), 221-249.

Oskierski, H. C., Beinlich, A., Mavromatis, V., Altarawneh, M., & Dlugogorski, B. Z. (2019). Mg isotope fractionation during continental weathering and low temperature carbonation of ultramafic rocks. *Geochimica et Cosmochimica Acta*.

Palmer, M. R., & Edmond, J. M. (1989). The strontium isotope budget of the modern ocean. *Earth and Planetary Science Letters*, *92*(1), 11-26.

Panchuk, K. M., Holmden, C. E., & Leslie, S. A. (2006). Local controls on carbon cycling in the Ordovician midcontinent region of North America, with implications for carbon isotope secular curves. *Journal of Sedimentary Research*, *76*(2), 200-211.

Patterson, W. P., & Walter, L. M. (1994). Depletion of ^{13}C in seawater ΣCO_2 on modern carbonate platforms: Significance for the carbon isotopic record of carbonates. *Geology*, *22*(10), 885-888.

Peng, Y., Shen, B., Lang, X. G., Huang, K. J., Chen, J. T., Yan, Z., Tang, W., Ke, S., Ma, H., & Li, F. B. (2016). Constraining dolomitization by Mg isotopes: A case study from partially dolomitized limestones of the Middle Cambrian Xuzhuang Formation, North China. *Geochemistry, Geophysics, Geosystems*, *17*(3), 1109-1129.

Perrin, N. A. (1982). Environment of Deposition of Winnipegosis Formation (Middle Devonian), Williston Basin, North Dakota. *AAPG Bulletin*, *66*(5), 616-617.

Powley, D. E. (1990). Pressures and hydrogeology in petroleum basins. *Earth-Science Reviews*, *29*(1-4), 215-226.

Pratt, B. R., Haidl, F. M., & Holmden, C. (2008). Microbial patch reefs in Upper Ordovician Red River strata, Williston Basin, Saskatchewan: Signal of heating in a deteriorating epeiric sea. *Dynamics of Epeiric Seas. Geological Association of Canada, Special Publication*, *48*, 303-340.

Qing, H., & Mountjoy, E. W. (1994). Formation of coarsely crystalline, hydrothermal dolomite reservoirs in the Presqu'ile barrier, Western Canada sedimentary basin. *AAPG bulletin*, *78*(1), 55-77.

Qing, H. (1998). Petrography and geochemistry of early-stage, fine-and medium-crystalline dolomites in the Middle Devonian Presqu'ile Barrier at Pine Point, Canada. *Sedimentology*, *45*(2), 433-446.

Rédly, P. (1998). *Tectonostratigraphic evolution of the Williston Basin*. (Doctoral dissertation, University of Saskatchewan).

Reinson, G. E., & Wardlaw, N. C. (1972). Nomenclature and Stratigraphic Relationships, Winnipegosis and Prairie Evaporite Formations. Central Saskatchewan. *Bulletin of Canadian Petroleum Geology*, *20*(2), 301-320.

Rhodes, D., Lantos, E. A., Lantos, J. A., Webb, R. J., & Owens, D. C. (1984). Pine Point orebodies and their relationship to the stratigraphy, structure, dolomitization, and karstification of the Middle Devonian barrier complex. *Economic Geology*, *79*(5), 991-1055.

Ries, J. B. (2010). Geological and experimental evidence for secular variation in seawater Mg/Ca (calcite-aragonite seas) and its effects on marine biological calcification. *Biogeosciences*, *7*(9), 2795-2849.

Robertson, H., Corlett, H., Hollis, C., Kibblewhite, T, Whitaker, F. (2019) Listwanitization as a source of Mg for dolomitization: Field evaluation of Atlin, British Columbia. Goldschmidt Annual Meeting Abstracts, Barcelona

Romanek, C. S., Grossman, E. L., & Morse, J. W. (1992). Carbon isotopic fractionation in synthetic aragonite and calcite: effects of temperature and precipitation rate. *Geochimica et cosmochimica acta*, *56*(1), 419-430.

Rosman, K. J. R., & Taylor, P. D. P. (1998). Isotopic compositions of the elements 1997 (Technical Report). *Pure and Applied Chemistry*, *70*(1), 217-235.

Rosenbaum, J., & Sheppard, S. M. F. (1986). An isotopic study of siderites, dolomites and ankerites at high temperatures. *Geochimica et cosmochimica acta*, *50*(6), 1147-1150.

Rosenthal, L. R. (1987). The Winnipegosis Formation of the northeastern margin of the Williston Basin. *Williston Basin Symposium.*

Rostron, B. J., Holmden, C., & Kreis, L. K. (1998). Hydrogen and oxygen isotope compositions of Cambrian to Devonian formation waters, Midale area, Saskatchewan. *Eighth International Williston Basin Symposium*, 267-273.

Rostron, B. J., & Holmden, C. (2000). Fingerprinting formation-waters using stable isotopes, Midale area, Williston Basin, Canada. *Journal of Geochemical Exploration*, *69*, 219-223.

Rostron, B. J., & Holmden, C. (2003). Regional variations in oxygen isotopic compositions in the Yeomanand Duperow aquifers, Williston basin (Canada-USA). *Journal of Geochemical Exploration*, *78*, 337-341.

Rubinson, M., & Clayton, R. N. (1969). Carbon-13 fractionation between aragonite and calcite. *Geochimica et Cosmochimica Acta*, *33*(8), 997-1002.

Russell, W. A., & Papanastassiou, D. A. (1978). Calcium isotope fractionation in ion-exchange chromatography. *Analytical Chemistry*, *50*(8), 1151-1154.

Ryb, U., & Eiler, J. M. (2018). Oxygen isotope composition of the Phanerozoic ocean and a possible solution to the dolomite problem. *Proceedings of the National Academy of Sciences*, *115*(26), 6602-6607.

Ryu, J. S., Jacobson, A. D., Holmden, C., Lundstrom, C., & Zhang, Z. (2011). The major ion, δ44/40Ca, δ44/42Ca, and δ26/24Mg geochemistry of granite weathering at pH= 1 and T= 25° C: power-law processes and the relative reactivity of minerals. *Geochimica et Cosmochimica Acta*, *75*(20), 6004-6026.

Schmitt, A. D., Gangloff, S., Cobert, F., Lemarchand, D., Stille, P., & Chabaux, F. (2009). High performance automated ion chromatography separation for Ca isotope measurements in geological and biological samples. *Journal of Analytical Atomic Spectrometry*, *24*(8), 1089-1097.

Sharma, T., & Clayton, R. N. (1965). Measurement of $^{18}O/^{16}O$ ratios of total oxygen of carbonates. *Geochimica et Cosmochimica Acta*, *29*(12), 1347-1353.

Shosa, J. D., & Cathles, L. M. (2001). Experimental investigation of capillary blockage of two-phase flow in layered porous media. In *Petroleum Systems of Deep-Water Basins: Global and Gulf of Mexico Experience: Proceedings of the GCSSEPM Foundation, 21st Annual Bob F. Perkins Research Conference*, 725-739.

Sibson, R. H. (1994). Crustal stress, faulting and fluid flow. In *Geofluids: origin, migration and evolution of fluids in sedimentary basins* (Ed. J. Parnell) Geol. Soc. Special Publication 78, 69-84.

Spokes, L., Jickells, T., & Jarvis, K. (2001). Atmospheric inputs of trace metals to the northeast Atlantic Ocean: the importance of southeasterly flow. *Marine Chemistry*, *76*(4), 319-330.

Stanford, R. L. (1989). Sedimentology and diagenesis of the Winnipegosis Formation, southeastern Saskatchewan. (Doctoral dissertation, University of Alberta).

Stiller, M., Rounick, J. S., & Shasha, S. (1985). Extreme carbon-isotope enrichments in evaporating brines. *Nature*, *316*(6027), 434.

Stoakes, F. C., & Campbell, G., & Hassler, R., & Dixon, & D. Forbes. (1987) Sedimentology and hydrocarbon source potential of the Middle Devonian Winnipegosis Formation of southeastern Saskatchewan. *Stoakes Campbell Geoconsulting Report (unpublished),* 1-98.

Stuiver, M. (1970). Oxygen and carbon isotope ratios of fresh-water carbonates as climatic indicators. *Journal of Geophysical Research*, *75*(27), 5247-5257.

Swart, P. K. (2008). Global synchronous changes in the carbon isotopic composition of carbonate sediments unrelated to changes in the global carbon cycle. *Proceedings of the National Academy of Sciences*, *105*(37), 13741-13745.

Swart, P. K., Burns, S. J., & Leder, J. J. (1991). Fractionation of the stable isotopes of oxygen and carbon in carbon dioxide during the reaction of calcite with phosphoric acid as a function of temperature and technique. *Chemical Geology: Isotope Geoscience section*, *86*(2), 89-96.

Swart, P. K., & Eberli, G. (2005). The nature of the $\delta^{13}C$ of periplatform sediments: Implications for stratigraphy and the global carbon cycle. *Sedimentary Geology*, *175*(1-4), 115-129.

Swart, P. K., Oehlert, A. M., Mackenzie, G. J., Eberli, G. P., & Reijmer, J. J. G. (2014). The fertilization of the Bahamas by Saharan dust: A trigger for carbonate precipitation?. *Geology*, *42*(8), 671-674.

Szabo, E., & Cioppa, M. T. (2006). Multiple magnetization events in the Red River carbonates, Williston Basin, Canada: Evidence for fluid-flow?. *Journal of Geochemical Exploration*, *89*(1-3), 384-388.

Taylor, S. R., & McLennan, S. M. (1985). The continental crust: its composition and evolution.

Teng, F. Z., Li, W. Y., Ke, S., Marty, B., Dauphas, N., Huang, S., Wu, F., & Pourmand, A. (2010). Magnesium isotopic composition of the Earth and chondrites. *Geochimica et Cosmochimica Acta*, *74*(14), 4150-4166.

Teng, F. Z., Wadhwa, M., & Helz, R. T. (2007). Investigation of magnesium isotope fractionation during basalt differentiation: implications for a chondritic composition of the terrestrial mantle. *Earth and Planetary Science Letters*, *261*(1-2), 84-92.

Teng, F. Z. (2017). Magnesium isotope geochemistry. *Reviews in Mineralogy and Geochemistry*, *82*(1), 219-287.

Tipper, E. T., Galy, A., Gaillardet, J., Bickle, M. J., Elderfield, H., & Carder, E. A. (2006). The magnesium isotope budget of the modern ocean: constraints from riverine magnesium isotope ratios. *Earth and Planetary Science Letters*, *250*(1-2), 241-253.

Tipper, E. T., Louvat, P., Capmas, F., Galy, A., & Gaillardet, J. (2008). Accuracy of stable Mg and Ca isotope data obtained by MC-ICP-MS using the standard addition method. *Chemical Geology*, *257*(1-2), 65-75.

Tóth, J. (1963). A theoretical analysis of groundwater flow in small drainage basins. *Journal of geophysical research*, *68*(16), 4795-4812.

Tóth, J. (1980). Cross-formational gravity-flow of groundwater: a mechanism of the transport and accumulation of petroleum (the generalized hydraulic theory of petroleum migration). Am. Assoc. Pet. Geol. Stud. Geol., 10, 121-167.

Tucker, M., Wright, V.P., 1990. Carbonate Sedimentology. Blackwell Scientific Publications, Oxford, 482.

Vahrenkamp, V. C., & Swart, P. K. (1990). New distribution coefficient for the incorporation of strontium into dolomite and its implications for the formation of ancient dolomites. *Geology*, *18*(5), 387-391.

Van der Voo, R. (1988). Paleozoic paleogeography of North America, Gondwana and intervening. displaced terranes: Comparisons of palaeomagnetism with paleoclimatology and biogeographical patterns. *Geol. Soc. Amer. Bull.*, *100*, 411-423.

Veizer, J., Ala, D., Azmy, K., Bruckschen, P., Buhl, D., Bruhn, F., Carden, G.A.F., Diener, A., Ebneth, S., Godderis, Y., Jasper, T., Korte, C., Pawellek, F., Podlaha, O.G. and Strauss, H. (1999). $^{87}Sr/^{86}Sr$, $\delta^{13}C$ and $\delta^{18}O$ evolution of Phanerozoic seawater. *Chemical geology*, *161*(1-3), 59-88.

Warren, J. (2000). Dolomite: occurrence, evolution and economically important associations. *Earth-Science Reviews*, *52*(1-3), 1-81.

Wasserburg, G. J., Lee, T., & Papanastassiou, D. A. (1977). Correlated O and Mg isotopic anomalies in Allende inclusions: II. Magnesium. *Geophysical Research Letters*, *4*(7), 299-302.

Wendte, J., Dravis, J. J., Stasiuk, L. D., Qing, H., Moore, S. L., & Ward, G. (1998). High-temperature saline (thermoflux) dolomitization of Devonian Swan Hills platform and bank carbonates, Wild River area, west-central Alberta. *Bulletin of Canadian Petroleum Geology*, *46*(2), 210-265.

Whitaker, F., Smart P. L. and Jones G. D. (2004) Dolomitization: from conceptual to numerical models. In *The Geometry and Petrogenesis of Dolomite Hydrocarbon Reservoirs* (Eds. C. J. R. Braithwaite, G. Rizzi and G. Darke) Geol. Soc., London, Special Publications 235, 99-139.

Whitaker, F. F., & Xiao, Y. (2010). Reactive transport modeling of early burial dolomitization of carbonate platforms by geothermal convection. *AAPG bulletin*, *94*(6), 889-917.

Wilkinson, B. H., & Algeo, T. J. (1989). Sedimentary carbonate record of calcium-magnesium cycling. *American Journal of Science*, *289*(10), 1158-1194.

Williams, R. H., McGee, D., Kinsley, C. W., Ridley, D. A., Hu, S., Fedorov, A., Tal, I., Murray, R., & deMenocal, P. B. (2016). Glacial to Holocene changes in trans-Atlantic Saharan dust transport and dust-climate feedbacks. *Science advances*, *2*(11), e1600445.

Wilson, E. N., Hardie, L. A., & Phillips, O. M. (1990). Dolomitization front geometry, fluid flow patterns, and the origin of massive dolomite: the Triassic Latemar buildup, northern Italy. *American Journal of Science*, *290*(7), 741-796.

Witzke, B. J. (1990). Palaeoclimatic constraints for Palaeozoic palaeolatitudes of Laurentia and Euramerica. *Geological Society, London, Memoirs*, *12*(1), 57-73.

Yapparova, A., Gabellone, T., Whitaker, F., Kulik, D. A., & Matthäi, S. K. (2017). Reactive transport modelling of hydrothermal dolomitisation using the CSMP++ GEM coupled code: Effects of temperature and geological heterogeneity. *Chemical Geology*, *466*, 562-574.

Young, E. D., & Galy, A. (2004). The isotope geochemistry and cosmochemistry of magnesium. *Reviews in Mineralogy and Geochemistry*, *55*(1), 197-230.

APPENDIX A. – Supplementary Material

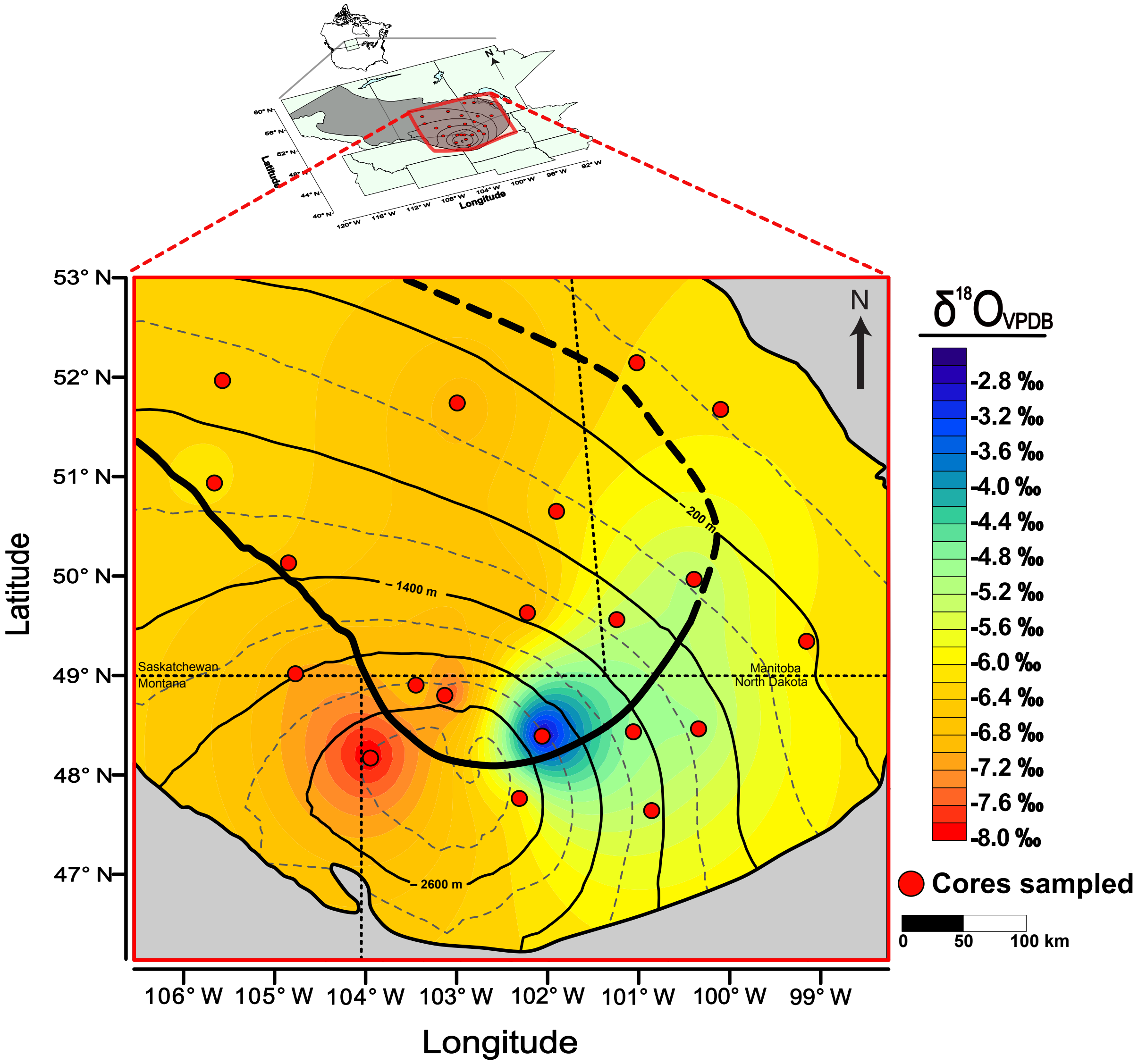

Supplementary Figure 1 Shaded contour map of carbonate $\delta^{18}O$ values of the Lower Member Winnipegosis Formation. The erosional extent of the Middle Devonian Elk Point Basin demarcates the countering limits. Thick black line represents the divide between the central basin / mud mound facies and the surrounding platform facies (Modified after Fischer and Burke, 1987 and Jin and Bergman, 1999). See locations of sampled sites indicated by red circles. Depth to the top of the Winnipegosis is represented as an isopach overlay shown in solid and dashed lines (300 m spacing, max depth dashed contour line at 2900 m below sea level).

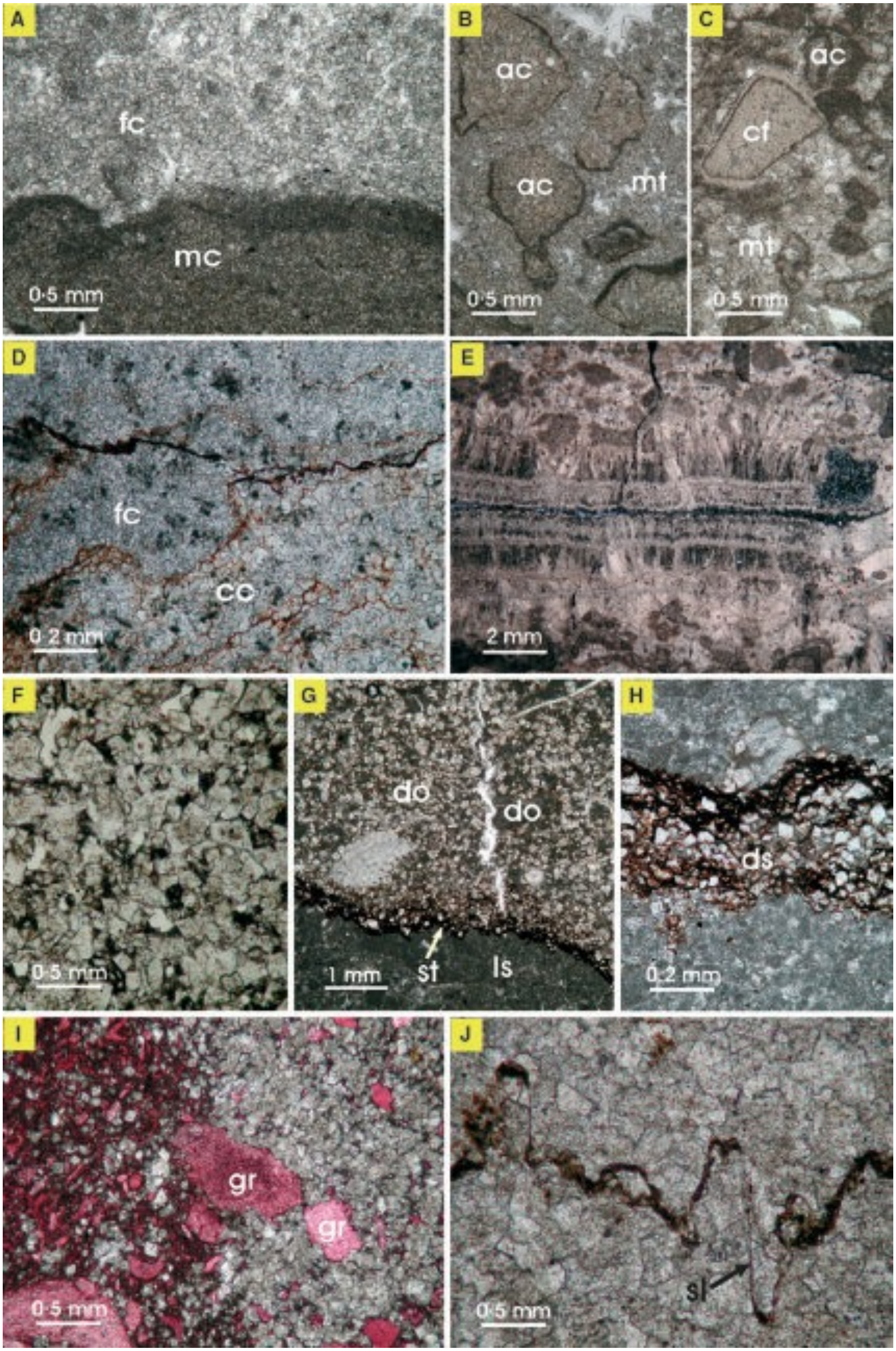
A
fc
mc
0·5 mm
B
ac
ac
mt
0·5 mm
C
ac
cf
mt
0·5 mm
D
fc
cc
0·2 mm
E
2 mm
F
0·5 mm
G
do
do
st
ls
1 mm
H
ds
0·2 mm
I
gr
gr
0·5 mm
J
sl
0·5 mm

Supplementary Figure 2 Photomicrographs showing textures of type 1 dolomite (A–E) and type 2 (F–J) dolomite. **(A)** Dolomite in the upper view field of picture (fc) is finely crystalline and nonplanar-a, which is interpreted as resulting from recrystallization. Intercrystalline porosities are filled with acicular anhydrite. Dolomite in the lower view field of picture (mc) is microcrystalline. 6-36-38-28W2, 1041 m, the Upper Winnipegosis Member (UW), plane polarized light (PPL). **(B)** Crystals of type 1 dolomite in precursor grains (ac) are coarser than those in matrix (mt). 16-20-37-8W3, 1104.6m, UW, PPL. **(C)** Crystals of type 1 dolomite in precursor grains (ac) are finer than those in matrix (mt). A single, inclusion-enriched dolomite crystal mimics the morphology of a crinoidal fragment (cf). 13-1-38-8W3, 1152.8m, UW, PPL. **(D)** Very fine to finely crystalline, planar-s type 1 dolomite. Note crystal size varies from very finely crystalline (fc) in one side of the stylolite to finely crystalline (cc) in the other side. 10-29-36-9W3, 1179.4 m, UW, PPL. **(E)** Type 1 dolomite mimetically replaces the radiaxial fibrous cements inferred to have precipitated as calcite from sea water in submarine environments. 6-36-38-28W2, 1047.0 m, UW, cross polarized light. **(F)** Type 2 dolomite is medium crystalline and mainly planar-e. Note intercrystalline porosity. 7-2-38-1W3, 1186.0 m, the Lower Winnipegosis Member (LW), PPL. **(G)** Dolomitization (do) front in limestone (ls) is constrained by a stylolite (st). 6-16-38-1W3, 1175.9 m, LW, PPL. **(H)** Replacement of limestone by type 2 dolomite occurs along dissolution seams (ds). 6-16-38-1W3, 1175.9 m, LW, PPL. **(I)** Wackestone (red stained with Alizarin Red-S) is partially replaced by type 2 dolomite (in grey color). In the left half view field of picture, rhomboid type 2 dolomite crystals ‘floating’ in limestone; in the right half view field of picture, limestone relicts (mainly grain relicts, denoted by gr) ‘floating’ in dolomite. 13-3-42-26W2, 1002.1 m, LW, PPL. **(J)** Type 2 dolomite showing medium crystalline, planar-s fabric. Note dolomite crystals are truncated by stylolites (sl). 16-11-33-1W3, 1278.2 m, LW, PPL. Modified after Fu et al., 2006.